



DOCTORAL DISSERTATION

SUBMITTED IN PARTIAL FULFILLMENT OF THE REQUIREMENTS
FOR THE DEGREE OF **DOCTOR OF ENGINEERING**

TITLE: Numerical Modeling of Transport in Metal Foam Using an Idealized Geometrical Cell

PRESENTED BY: Ahmed Salem Sulaiman

Table of Contents

Abstract.....	v
List of Figures.....	ix
List of Tables.....	xiv
Chapter 1: Introduction.....	1
1.1 Background.....	1
1.2 Objectives and Scope of Work.....	2
Chapter 2: Literature Survey.....	4
Chapter 3: Geometrical Cell Development.....	13
3.1 Modeling the Structure of the Foam.....	14
3.2 Geometrical Characterization Verification.....	24
3.2.1 Porosity.....	24
3.2.2 Specific Surface Area.....	24
3.2.3 Cell and Pore.....	25
3.2.4 Ligament.....	26
Chapter 4: Numerical Simulation of Flow Field for One Cell.....	28
4.1 Overview COMSOL.....	29
4.1.1 Pre Processing.....	29
4.1.2 Processing (Study).....	29
4.2.3 Post Processing (Results).....	30

4.2 Model Descriptions	30
4.2.1 Physical Domain	30
4.2.2 Laminar flow.....	31
4.2.3 Meshing and Solving	32
4.2.4 Results.....	33
Chapter 5: Simulation of Fluid Flow	36
5.1 Introduction	36
5.2 Physical Fluid Flow Problem	36
5.3 Computational Domain Creation	37
5.4 Numerical Simulation	41
5.4.1 Flow Phenomenon	41
5.4.2 Boundary Conditions	42
5.4.3 Meshing and Mesh Dependence	43
5.5 Results	47
5.6 Experimental Validation	51
5.6.1 Experiment Set Up.....	51
5.6.2 Comparison	53
5.7 Model Limitations	56
5.8 Study of Hydrodynamic Entry Length	59
5.8.1 Geometrical Model	59

5.8.2 Simulation Results	60
5.8.3 Entry-Length Experiment Verification	71
Chapter 6: Numerical Convection Heat Transfer in Metal Foam.....	74
6.1 Introduction	74
6.2 Problem Description.....	76
6.3 Numerical Simulations.....	79
6.3.1 Geometrical & Fluid domains.....	79
6.3.2 Model Description	83
6.3.3 Solving with The Marching Technique	85
6.4 Mesh Independence.....	91
6.5 Results	95
6.5.1 Temperature Field of Entry Region	95
6.5.2 Temperature Field of Fully Developed Region	97
6.5.3 The Wall Temperature	97
6.5.4 Mean Temperature	98
6.5.5 Nusselt Number	99
Chapter 7 : Heat Transfer Validation.....	101
7.1 Volume-Averaged Analytical Solution.....	101
7.2 Experiment	105
7.2.1 Sample.....	105

7.2.2 Wind Tunnel and Set-up	113
7.2.3 Procedure	115
7.3 Comparison	116
Chapter 8 : Conclusion.....	122
References.....	124

Abstract

Open-cell metal foam is a class of modern porous media that possesses high thermal conductivity, large accessible surface area per unit volume and high porosities (often greater than 90%). The high porosity means very low weight. The microstructure of the foam is web-like. Internal flow inside the foam is complex and includes flow reversal, destruction of boundary layers and vigorous mixing. All of these attributes make metal foam a very attractive heat transfer core for many applications, e.g. heat exchange and reactors. The rather complex and intrinsically random architecture of the foam is virtually impossible to capture exactly. In this dissertation, a unit cell geometrical model was developed that can be used to understand fluid flow behavior and heat transfer through open-cell metal foam. In particular, two numerical models were constructed to simulate, *first*, the fluid flow and pressure drop inside aluminum foam; *second*, forced convection heat transfer between the aluminum foam and air. The Navier-Stokes and the governing energy equation were directly solved and the velocity and temperature fields were obtained using COMSOL. The details of the modeling process are given in this dissertation. The pressure drop results were compared to experimental data, from which the permeability, form drag coefficient and hydrodynamic entry length could be calculated. The commercial foam that was used in the experiment had 10 pores per inch, with a porosity of 91.2%. Air was forced to flow inside the foam using an open loop wind tunnel. Good agreement between the modeling and experimental results were obtained, within the velocity range of the study. To validate the heat transfer model, numerical air temperatures were compared to the volume-averaged analytical

predictions, and to physical experimental data. The volume-averaged analytical formulation employed the Darcy-extended Brinkman model for momentum, and the non-thermal-equilibrium two-energy-equation model for the temperatures of the solid and the fluid phases inside a channel filled with foam, and heated at its top and bottom bounding surfaces by a uniform heat flux. The physical experiment was conducted on 20-pores-per-inch commercial aluminum foam, with a porosity of 90 %. Local air temperatures were measured inside a commercial aluminum foam cylinder heated at its outer wall by a constant heat flux, and cooled by forced air flow. A comparison showed good agreement between the numerical, experimental and the analytical air temperatures, within the thermally fully-developed region. The results are encouraging and lend confidence to the modeling approach, which paves the way for investigating other phenomena inside the foam.

Acknowledgment

I would like to express sincere appreciation to all people who help to make this dissertation done. First, many thanks to my advisor, Prof. Nihad Dukhan, who inspired me to work on the research, and helped me at various stages of the writing. His knowledge and enthusiasm about our research field greatly encouraged me and built role model for me to follow.

I also would like to thank Dr. Schumack, for providing me with valuable guidance on my research and class work, and Mr. Stuart Tucker for helping me with my English. Great and special thanks go to Mr. Sassak Chris for the great assistance that he has offered to prepare the experimental model. Also, thanks go to all my friends and colleagues working in Dr. Dukhan's research Lab, especially Mr. Muntadher Al-Rammahi.

Dedication

I dedicate this dissertation to my parents, my dear wife, my daughters, and my brothers and sister. This cannot be finished without the support and encouragement that I received from my parents who always pray for me and sacrificed themselves for my future goodness.

List of Figures

Figure 3. 1 The Internal Structure of Open Metal Foam[38].....	14
Figure 3. 2 A Sphere Surrounding by Fourteen Spheres. (a) Six Polar Spheres. .	15
Figure 3. 3 Overlapping Two Spheres; (a) A Polar Sphere with The Central Sphere, (b) A Quadrant Sphere with The Central Sphere.....	16
Figure 3. 4 The 10 PPI Sphere Number; (a) One Inch Consisting Five Spheres, (b) 3D View of the Central Sphere.....	17
Figure 3. 5 The Creation of Unit Cell; (a) Locations and Subtracting Spheres at Cube Faces, (b) Locations and Subtracting the Spheres at Vertices, (c) Locations and Subtracting the Central Sphere and the Ideal Periodic Unit Cell.....	18
Figure 3. 6 Overlapping Volume o Two Spheres	20
Figure 3. 7 Geometrical Relationship Between d_1 and d_2	22
Figure 3. 8 Specific Surface Area is Calculated by CAD Tools of Current Geometrical Model.	25
Figure 3. 9 Pore and Cell Shape. (a) ERG [38],(b) Current Geometrical Model .	26
Figure 3. 10 The Ligament Cross Section for Current Geometrical Model and ERG. (a) ERG [38]at Different Relative Densities, (b) The Current Geometrical Model at 2.2% Relative Density.	27
Figure 3. 11 Ligament diameter (in). (a) Current geometrical model; (b) ERG[38].....	27
.....	
Figure 4. 1 Schematic of Physical Model	30

Figure 4. 2 Mesh Grids in Unit Cell Model for Fluid Flow.....	32
Figure. 4. 3 Fluid Flow Streamlines in the Porous Channel Colored by Velocity Magnitude for a Free Stream Velocity of 1.28 m/s.	34
Figure 4. 4 Pressure Drop per Unit Length as a Function of Free Stream Velocity for a Unit Cell	35
Figure 5. 1 Schematic of Fluid Flow Problem.....	36
Figure 5. 2 Pore Level Domain.....	38
Figure 5. 3 10 PPI Duocel® Aluminum 6101 Alloy Metal Foam, 90.2 % Porous	38
Figure 5. 4 Creation of Computational Domain	39
Figure 5. 5 The Computational Domain and Boundary Conditions in 3D	41
Figure 5. 6 Element Kinds. a) Tetrahedral Element. b) Hexahedral Element. c) Prismatic Element.....	43
Figure 5. 7 Meshing	44
Figure 5. 8 Details of Volume Mesh of Cells at the Coarse and Fine Meshes	45
Figure 5. 9 Pressure Drop at Different Meshes and $V=0.31$ m/sec	45
Figure 5. 10 Cross-Sectional Slices Colored by Velocity Magnitudes for an Inlet Velocity of 1.18 m/s.....	48
Figure 5. 11 Streamlines Colored by Velocity for an Inlet Velocity of 1.18 m/s.	49
Figure 5. 12 Velocity Vector at an x-z Plane Passing through Middle of the Domain for an Inlet Velocity of 1.18 m/s.	50
Figure 5. 13 Experimental Testing Equipment Setup.....	51

Figure 5. 14 Pressure Drop from Numerical and Experimental Studies of 10 PPI and 97% Porosity Foam	54
Figure 5. 15 Pressure Drop from Numerical and Experimental Studies of 10 PPI and 97% Porosity Foam	56
Figure 5. 16 The Computational Domain of Hydrodynamic Entry Length.....	59
Figure 5. 17 Cross-Sectional Slices Colored by Velocity Magnitudes for Inlet Velocities of 2.35 and 4.48 m/s.	61
Figure 5. 18 Streamlines Colored by Velocity Magnitudes for Inlet Velocities of 2.35 and 4.48 m/s.	62
Figure 5. 19 Velocity Vector at an x-z Plane Passing through the Middle of the Domain for Inlet Velocities of 2.35 and 4.48 m/s.....	64
Figure 5. 20 Two-Dimensional Plot Showing Velocity Vectors in an X-Z Plane Passing Through the Center of the Cells for All Five Values of Inlet Velocities.	66
Figure 5. 21 Cell Center z-Velocity Component at 2.54 mm from the Entrance of Each Cell as a Function of Cell Number	67
Figure 5. 22 Pressure Drop over the Length of Each Cell	68
Figure 5. 23 Schematic of the Test Section.	71
Figure 5. 24 Schematic of Entrance Effects Measurement.	72
Figure 5. 25 Pressure Drop per Unit Length across the Porous Channel	73
Figure 6.1 Problem Schematic	76
Figure 6.2 Taking Thin Slice From the Actual Physical Domain.....	79
Figure 6.3 Splitting the Thin-Slice Domain into Even Blocks	80

Figure 6.4 3D Metal Foam Geometrical Approximation at Pore Level	81
Figure 6.5 Creation of One Block Model	82
Figure 6.6 The Block Model Set-Up Including Channel and Metal Foam.....	84
Figure 6.7 Setting Up a Unit block Before Marching Technique.....	86
Figure 6.8 The First Marching Block Set-Up	87
Figure 6.9 Second Marching Block Set-Up.....	88
Figure 6.10 The Third Marching Block Set-Up.....	89
Figure 6.11 The Last Marching Block Set-Up.....	90
Figure 6.12 The Computational Model with Fine Mesh.....	91
Figure 6.13 Details of Volume Mesh of Heated Wall and Cells for the Coarse and Fine Meshes	92
Figure 6.14 Fluid Temperatures at $x=0.635$ cm for All Meshing.....	93
Figure 6.15 Pressure Drop at Different Meshes.....	94
Figure 6. 16 Temperature Field of Developing Entry Rgion.....	95
Figure 6. 17 Air Temperature for Fully Developing Region at 2.55 inch from Heated Wall	96
Figure 6. 18 Temperature Field of Fully Developed Region.....	97
Figure 6.19 Wall Local Temperature as Function of Distance in Flow Direction	98
Figure 6. 20 The Mean Temperture as Function of line distance in The Flow direction	99
Figure 6. 21 Nusselt Number as a Function of Axial Distance.	100

Figure 7. 1 Photograph of the Cylindrical Foam Sample	105
Figure 7. 2 Photograph of the Thermocouples’ Holes	106
Figure 7. 3 Photograph of Slots to Measure the Temperature of the Wall	107
Figure 7. 4 The Angles between the Holes in the Set.....	108
Figure 7. 5 Photograph of the Small Tubes	109
Figure 7. 6 Photograph of the Thermocouple Inside the Small	110
Figure 7. 7 Photograoh of the Groove in the Wall’s Sample.....	110
Figure 7. 8 Photograph of the Foam Sample Instrumented with Thermocouples	111
Figure 7. 9 Photograph of the Heaters	112
Figure 7. 10 Photograph of the Foam Sample with Thermofoil Heaters.....	112
Figure 7. 11 Photograph of the Open-Loop Tunnel.....	113
Figure 7. 12 Photograph of Sample Wrapped with the Insulation.....	114
Figure 7. 13 Photograph of the Complete Set-up	114
Figure 7. 14 Experimental and Numerical Air Temperatures.....	117
Figure 7. 15 Analytical and Numerical Air Temperatures.....	118
Figure 7. 16 Anaytical Air Temperature.....	119
Figure 7. 17 Physical Air Temperatures	120

List of Tables

Table 3. 1 Current Model & ERG [38] Foam Parameters	26
Table 4. 1 Permeability and Form Drag.....	35
Table 5. 1 Foam Parameters.....	40
Table 5. 2 Meshing levels with their number of elements	46
Table 5. 3 Experimental Normalized Pressure Drop with Numerical for Low Velocity Regime for 10 PPI and 97% Porosity Foam	55
Table 5. 4 Experimental Normalized Pressure Drop with Numerical for Low and High Velocity Regimes for 10 PPI and 97% Porosity Foam.....	57
Table 5. 5 Simulation and Experimental Values of Permeability and Form Drag Coefficient in the Low- and High-Velocity Regimes.	58
Table 5. 6 Entrance Length for Various Inlet Velocities	68
Table 6. 1 Meshing Levels with Their Number of Elements and Pressure Drop (Pa/m).....	93
Table 7. 1 Location of Each Themocouple and Numbering System	106
Table 7. 2 Proprties of the Heater	112
Table 7. 3 Air temperature Differences for Parallel plates and cylinder	121

Nomenclature

CPI	cell per inch
R	sphere radius, Chapter (3)
r0	cylinder radius
b ₁	constant, Eq. (7.10)
Bi	channel porous media Biot number = $h\sigma H^2/k_s$ (dimensionless)
C	specific heat of fluid ($\text{J.kg}^{-1}.\text{K}^{-1}$)
d ₁	constant, Eq. (7.10)
d ₂	constant, Eq. (7.10)
d ₃	constant, Eq. (7.10)
Da	Darcy number = K/H^2 (dimensionless)
D _h	Hydraulic diameter (m)
h	convection heat transfer coefficient ($\text{W.m}^{-2}.\text{K}^{-1}$)
k	effective thermal conductivity ($\text{W.m}^{-1}.\text{K}^{-1}$)
K	permeability (m^2)
q"	heat flux (W.m^{-2})
T	temperature (K)
u	volume-averaged pore velocity (m.s^{-1})
U	non-dimensional velocity
r	computational length
L	channel length
H	half of porous medium height (m)
x	axial coordinate along flow direction (m)
X	non-dimensional axial coordinate along flow direction
z	perpendicular coordinate to flow direction (m)

Z non-dimensional perpendicular coordinate to flow direction

Greek

ε porosity (dimensionless)

γ ratio of effective viscosity to actual fluid viscosity = μ/μ_e

λ ratio of effective thermal conductivities = k_f/k_s

θ dimensionless temperature

ρ density of fluid ($\text{kg}\cdot\text{m}^{-3}$)

σ surface area per unit volume of porous medium (m^{-1})

ω dimensionless parameter = $\sqrt{\gamma/Da}$

ψ dimensionless parameter = $\sqrt{Bi(\lambda+1)/\lambda}$

Subscripts

f fluid

m mean value

s solid

w wall

∞ free stream

Chapter 1: Introduction

1.1 Background

High porosity metal foams with a cellular structure have been increasingly applied in various applications, due to their interesting combinations of physical and mechanical properties. For example, they have been used in automotive and aerospace applications due to their high impact resistance and good strength -to-weight ratio [1]. Some uses of metal foam are found in thermal management applications, such as compact heat sinks of power electronics, compact heat exchangers and refrigerators, due to foam's huge accessible surface area and high conductivity of cell walls, which give unique heat transfer capability [2]. Metal foam is also used in geothermal reservoirs and petroleum drilling [3]. Open cell foams with specified sizes of pore have the potential to be applied in fluid filtration [4].

Aluminum, nickel, copper and titanium are the materials most used to make metal foam. The understanding of fluid flow behavior and heat transfer through open-cell metal foam is determined by investigation of its microstructure. Today, urgent requirements for such understanding, and thus for wide industrial applications, can only be met by implementation of Navier-Stokes and energy equations, with the use a predictive geometrical model of open cell metal foams. This model must be based on characterizing the foams' morphological parameters, namely; their shape and diameter of cell; shape and thickness of ligaments; specific surface area and porosity.

1.2 Objectives and Scope of Work

The success of any computational model using numerical methods is strongly dependent on accurate geometrical parameters of the foam, including the shape and size of pores, cells and ligaments; the porosity, the number of pores per inch (PPI); and the specific surface area (surface area to volume ratio).

The **first objective** of the current study is to develop a unit cell geometry in order to understand the microstructure of the foam and to provide a mathematical description of such geometry and its modeling parameters, which includes porosity, ligament's thickness and length, and size and shape of pore and cell.

The **second objective** is to develop a suitable physical model in COMSOL© for solving Navier-Stokes equations in different domains. This includes solving for velocity profile and pressure drop over the domains along airflow direction and the consideration of influence of different boundary conditions on these results.

The **third objective** is to experimentally verify pressure drop results for the model.

The **fourth objective** is to construct and solve a numerical model for forced convective heat transfer, and compare the results to experimental values.

This study is organized as follows. Chapter 2 is a literature survey. Chapter 3 will provide an overview of the recent progress in microstructure examination and geometrical modeling that can be used to properly characterize the internal structure of open cell metal foam. A numerical solution for one unit cell will be analyzed in Chapter 4. Chapter 5 describes simulation of fluid flow for the models and calculation

of pressure drop, permeability and form drag coefficient, along with experimental comparisons and limitations of this model. In additions, entrance effects will be investigated. Chapter 6 presents a basic numerical heat transfer model. Chapter 7 provides experimental and analytical validations of numerical air temperatures. Chapter 8 will provide the conclusion of this work and a call for future work.

Chapter 2: Literature Survey

Much of today's metal foam research consists of macroscopic studies instead of microscopic (pore-level scale). The prime reason for such an approach is the difficulties of describing predictive geometrical models, particularly the modeling of the shape and size of cells and ligaments which constitute the very core solution of transport equations inside the pores[5].

There is a large volume of experimental studies describing the flow behavior and heat transfer in porous media. The first experimental study of pressure difference over beds of sand was reported by Darcy in 1856 [6], which found that the pressure gradient through a porous medium has a linear relationship with the flow velocity and permeability. On the other hand, Forchheimer (1910) argued that the pressure drop in porous media for very high velocity was dominated by inertia force, which was accounted for by adding a quadratic term to Darcy's equation [7].

During the past 30 years much more published studies have become available on the characteristic of metal foam. In their experimental study, Antohe et al. [8] identified two hydraulic characteristics: the permeability and the inertia coefficient of air flow through 40-PPI compressed brazed foams. They used the pore-based Reynolds number method rather than the permeability-based method, which is widely applicable for granular media.

In 1998, an experimental study, Seguin [9], who studied flow regimes for different porous samples, concluded that the transition to the turbulent regime occurred in the particle diameter-based Reynolds number range of 300-600.

Peak et al. [10] have experimentally predicted pressure drop through aluminum foams of several porosities in the range of 89-96%, and they used an empirical model which correlated the friction factor with the permeability-based Reynolds number.

Noh et al. [11] investigated experimentally the pressure drop and forced convection heat transfer in an annulus filled with aluminum foam (10 PPI, Porosity, $\epsilon=0.90$) on the non-Darcy flow regime. Their test results have showed that the heat transfer coefficient depends on the Reynolds number being raised to power 0.4. In order to assess metal foam's flow and heat transfer characteristics and use for design of thermal applications, correlations for the friction factor and the Nusselt number were proposed.

Haji-sheikh and Vafai [12] studied thermally developing forced convection heat transfer in ducts of various cross sections. Their momentum and energy equations were solved by weighted residuals methods without inclusion of the viscous dissipation effects (the Brinkmen's extension).

Also, several analytical and numerical studies investigating the use of porous materials in convective heat transfer have been published. Hwang et al. [5] studied the convective heat exchange and friction drag for airflow in compressed aluminum foam having 10 PPI and porosities in the range of 70-95%. Their results showed that both friction drag and the volumetric heat transfer coefficient increase when foam porosity decreases at a fixed Reynolds number.

Vafai and Kim [13] used the analytical solution to obtain a closed –form for fully developed flow in a porous media channel bordered by parallel walls and subjected to

constant heat flux boundary conditions. Their model took account of boundary and inertia effects using a momentum equation, known Brinkman- Forcheimer extended Darcy model [14], and assumed local thermal equilibrium (LTE).

Neild, Kuznetsov, and Xiong [15,16] obtained an analytical solution of forced convection heat transfer and momentum equations for the flow through a parallel plate or circular tube with different boundaries, such as constant heat flux, constant temperature, and isothermal wall, when the axial conduction is negligible due to use of large Peclet number. Their analyses have been made on the assumption of LTE.

Extensive discussions on the validity of the LTE assumption were made by a number of researchers [17,18], who showed that the LTE is always valid when the solid conduction is the dominant heat transfer mode.

In 2002, Boomsma and Poulikakos [19] measured the hydraulic and thermal performance for water flow velocities (>0.1 m/sec) through open cell 40 PPI compressed unbrazed aluminum foam with porosities lower than 90%. This study was carried out on the metal foam's temperature profile; in addition, they used Fluent[®] commercial software to numerically analyze the pressure drop.

Mahajan R.L. and Calmidi V.V [20] conducted experimental and numerical investigations of forced convection using Local Thermal Non- Equilibrium (LTNE) in metal foam of various porosities and pore densities with air as the working fluid. Their numerical model was based on a packed bed of spheres. Their results indicate that the thermal dispersion effect is quite low when air is passing through the metal

foam, due to the relatively high conductivity of the solid matrix. However, dispersion would be considerably larger in the case of water.

The complex characteristics of velocity profile and pressure drop include flow recirculation at the back of solid fibers, turbulence, and unsteady flows; moreover, the heat transfer between the surface of the solid matrix and the fluid is not yet well understood by oversimplified approaches or empirical correlations, and there is a need for numerical analysis that is indisputable.

During the last ten years, extensive developments and tremendous advances have occurred in Computational Fluid Dynamics (CFD), and the results are rather amazing. Solving transport equations for micro fluid applications using numerical methods such as finite difference FD, finite element FE, or finite volume FV are good examples. Results of this analysis have transformed the understanding of fluid flow behavior and heat transfer concepts from the traditional models to simulation-based models. As a result, great savings have been achieved.

However, numerical methods are far from being perfect in modeling metal foam numerically, even though many recent papers and enormous resources have been published and spent on numerical methods for metal foam simulation [21–23], which apparently should cover all aspects of such a simulation. Nonetheless, commercially available software packages such as, Fluent[®], and others are readily available in the marketplace to carry out 2D and 3D metal foam simulations.

As pointed out by some researchers, the primary cause for the low fidelity of numerical methods for metal foam simulation is the inadequacy of numerical's

physical and geometrical model for metal foam modeling. All commercially available software packages are based on packed beds or granular media representatives having porosities from 0.3 to 0.6, whereas in metal foam the porosity is greater than 0.9 [24]. Most noticeable are (1) misrepresentation of the geometrical model of open cell metal foam; (2) improper boundary conditions; (3) lack of a validation strategy.

To date, two main approaches have been developed and used to simulate fluid flow and heat transfer through a variety of porous media: (a) macroscopic approach, where volume- averaged models have been used to predict flow and heat transfer behavior in porous media, predominantly in granular media [24–26]; (b) microscopic approach, where pore-scale level models have been used to investigate thermal and flow characteristics in high porosity open cell foam [27–29]. Each approach has its advantages and drawbacks. In the former approach, one major drawback is that it fails to take pore details into account, which may cause unpredictable flow characteristics. Most of the studies using the former approach were conducted at low Re [27]. That approach's advantage is that it is computationally cheap, and the entire physical domain can be simulated. In contrast to the former approach, the latter approach captures the intricate details of the foam structure but is computationally expensive; however, computational time can be reduced by symmetry in the physical domain where symmetry is found.

The microscopic approach also has a number of attractive uses: its modeling ability can capture small details at the pore-scale heat transfer, which can be used to yield the effective thermal conductivity of the foam for heat transfer. Another use of the microscopic approach is to yield the pumping power, which is a function of

pressure drop and inlet velocity. In additions, this approach is used to characterize the heat transfer coefficient and thermal resistance for quantifying the thermal performance of thermal devices during flow and convective heat transfer through the foam.

Numerous studies have attempted to directly model the geometry of the highly porous open metal foam by defining a representative elementary volume (REV) that captures the relevant characteristics of these materials in fluid flow and heat transfer. Du Plessis et al. [30] developed a geometrical modeling of the fluid dynamics in reticulated foams, such as aluminum with high porosity. Metallic foams were modeled by using a REV based on a set of rectangular prisms. These models were used to accurately predict pressure drop; in addition, to predict the permeability and foam drag as functions of the foam's structural characteristics (density, pore size, tortuosity, cell size, etc.). These models show good predictive power when confronted with experimental data using the flow of water in 40, 60 and 100 PPI foam at velocities above the Darcian regime with porosity range between 92% and 96%. Du Plessis et al. [30] reported that the permeability increased as porosity increased, and that inertia coefficient decreased. This modeling was later improved by Boomsma et al. [27] to capture more intricate details of the foam structure. Their idealized unit cell was a tetrakaidehedron, shown in Table 2. 1. Their REV consisted of eight equal volume cells with six 14-sided polyhedra having 12 pentagonal and two hexagonal faces, and two pentagonal dodecahedra. The cross section of ligaments was shaped triangularly. Laminar, incompressible flow was then modeled computationally

utilizing these unit cells along with periodic boundary conditions. Their numerical pressure drop results were lower than experimental results by 25%.

In 2010, Kopanidis et al. [22] carried out a 3D numerical simulation for conjugate flow and heat transfer of open-cell metal foam, based on REV shown in Table 2. 1. Both laminar and turbulent flow models were investigated for 10 and 20 PPI at 79% porosity.

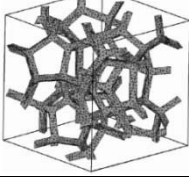
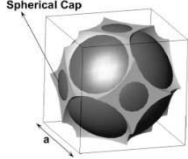



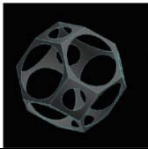
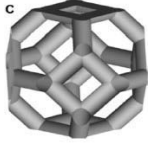
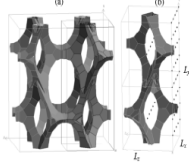
Although common computers are rapidly developing their computing power, they are still not powerful enough to model a complete piece of foam using REV. These issues can be overcome by investigating a periodic unit cell taken from open cell metal foam rather than using the REV approach. In 2006, Krishnan et al. [29] carried out a direct pore-scale level simulation of pressure drop and heat transfer in open cell metal foam using a periodic unit cell, shown in Table 2. 1. Their ideal unit cell was Body Center Cube (BCC), created by assuming the void pore is spherical, and the pores are located at the vertices and center of a unit cell. Their predicted thermal conductivity, pressure drop and heat transfer coefficient compared well with the experimental correlation for a porosity of 94%. Yu et al. [28,31] characterized the internal porous carbon foam structure based on a sphere-centered cubic periodic unit cell model, which produced a regularly - packed bed of spheres to quantify the forced convective heat transfer and pressure drop.

The other kind of periodic unit cell shape used a sphere-centered tetrakaidecahedron, generated first by cutting off the corners of a regular octahedron, and then subtracting a sphere at the center of the tetrakaidecahedron. The final

geometry is a sphere-center Kelvin structure [32,33]. Table 2. 1 shows these unit cells.

To improve the utilization of FEM in metal foam, a novel approach for characterization of these materials, in terms of permeability, pressure drop, and heat transfer will be used in this study. The approach is a BCC which was proposed by [29,34], due to the simplicity of the geometry and ease of meshing compared to the REV approach [22,27,35].

Table 2. 1 Previews Cell Models for Metal Foam.

Author	Year	Geomtery		Flow
Name		Type	shape	
Boomsma et al. [27]	2003	<ul style="list-style-type: none"> • REV 4.6x4.6x4.6 mm • 40 PPI • 8 Ttrakaidecahedron • $\epsilon = 0.96$ 		Periodic fully developed incompressible, S.S, laminar.
Krishnan et al. [29]	2006	<ul style="list-style-type: none"> • one cell • BCC • $\epsilon = 0.965$ • 10, 40 PPI 		<ul style="list-style-type: none"> • Periodic fully developed incompressible, S.S, laminar, Darcy • $Re \leq 10$
Karimian et al.[31]	2007	<ul style="list-style-type: none"> • Unit cell • $\epsilon = 0.80$ 		<ul style="list-style-type: none"> • fully developed • $Re_D \leq 0.1$ to 120
Angheliescu [34]	2009	<ul style="list-style-type: none"> • REV with 20x5 BBC • $\epsilon = 0.9031$ 		<ul style="list-style-type: none"> • Re_k • RANS with K-ϵ • Laminar
Kopanidis et al. [22]	2010	<ul style="list-style-type: none"> • REV • 10 PPI (2.82x2.82x5.82mm) • 40 PPI (9.61x9.61x19.85 mm) • Ttrakaidecahedron • $\epsilon = 0.97$ 		<ul style="list-style-type: none"> • Incompressible, S.S, laminar. • Turbulent
Mo Bai and J.N. Chung [32]	2011	<ul style="list-style-type: none"> • one cell 2.54x2.54x2.54 mm • Trakaidecahedron • 10PPI • $\epsilon = 0.974$ 		<ul style="list-style-type: none"> • $V \leq 10$ m/sec • Incompressible, S.S, laminar. • Turbulent
T. Horneber et al. [33]	2012	<ul style="list-style-type: none"> • one cell 2.54x2.54x2.54 mm • kelvin cell • 10PPI • $\epsilon = 0.89$ 		<ul style="list-style-type: none"> • incompressible, S.S, laminar. • Turbulent
De Jaeger P et al. [35]	2012	<ul style="list-style-type: none"> • Unit cell • 10 PPI • etrakaidecahedron • $\epsilon = 0.932$ 		<ul style="list-style-type: none"> • Periodic fully developed • $Re \leq 0.019$ to 370

Chapter 3: Geometrical Cell Development

To today, some techniques have been developed and introduced to obtain a representation of the 3D microstructure (pore-scale level) of metal foam. For instance, two techniques are digital imaging and idealized geometry. In the digital imaging technique, a 3D solid model of metal foam is constructed by taking digital microtomography data using a computed tomography scanner (CT). Then, image processing and 3D skeletonization are performed with image processing software [34,36]. In the idealized geometry technique, a unit cell is created; then, it is repeated in three directions to build the 3D model [29,31–35]. In contrast to the former technique, the latter technique is used to obtain an approximate representation of the 3D microstructure of metal foam. This is complicated due to the metal foam's complexity and randomness in ligaments and pore shape. All of these qualities make it difficult to obtain an accurate representation of 3D metal foam microstructure. Krishnan et al [29] approximated the internal structure of metal foam by building an ideal unit cell, known as the Body Center Cube (BCC). The BCC is constructed by subtracting eight identical spheres from a regular cube's vertices and one sphere from the cube's center. References 31 and 32 extended this concept, proposing a tetrakaidecahedral unit cell, obtained by cutting off the corners of a regular octahedron and then subtracting a sphere at the center of the tetrakaidecahedron. In the present research, an idealized geometry technique with BCC as a repeating unit cell represents an approximate 3D metal foam microstructure.

3.1 Modeling the Structure of the Foam

In the present study, the internal structure (or microstructure) of open-metal foam is represented by cells (or spheres), pores (or windows), and ligaments (or stents) as seen in Fig.3.1. All of these entities will be used to create ideal periodic unit cell.

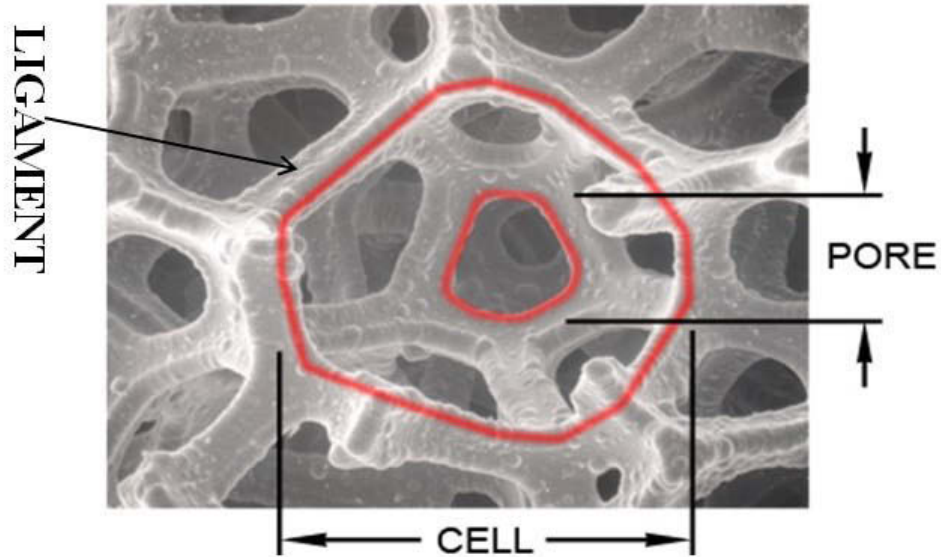


Figure 3. 1 The Internal Structure of Open Metal Foam[38]

Each cell is to be surrounded by fourteen equal volume spheres, six of which are located at a central sphere's poles as seen in Figure 3. 2(a). The other eight spheres are located at cell's quarters as shown in Figure 3. 2(b)

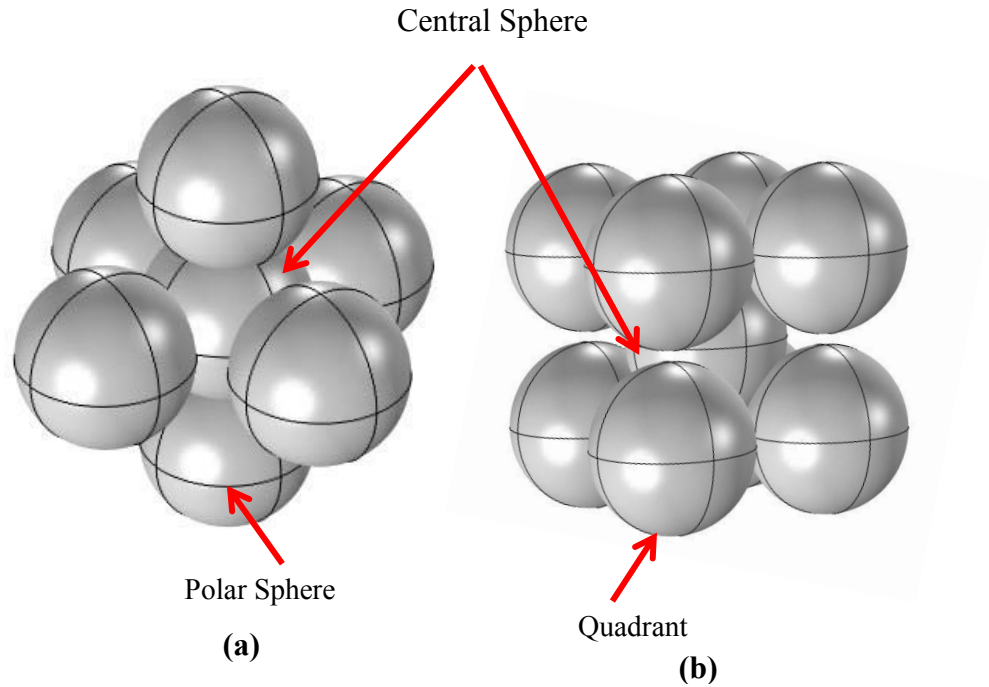


Figure 3. 2 A Sphere Surrounding by Fourteen Spheres. (a) Six Polar Spheres.

(b) Quadrant Spheres.

Each sphere of the fourteen spheres intersects with the central sphere (or cell) by a specific distance. Figure 3. 3(a) shows one of a polar sphere interfering with the central sphere by $2h_1$. Figure 3. 3(b) displays intersecting between the central sphere with quartic spheres by $2h_2$.

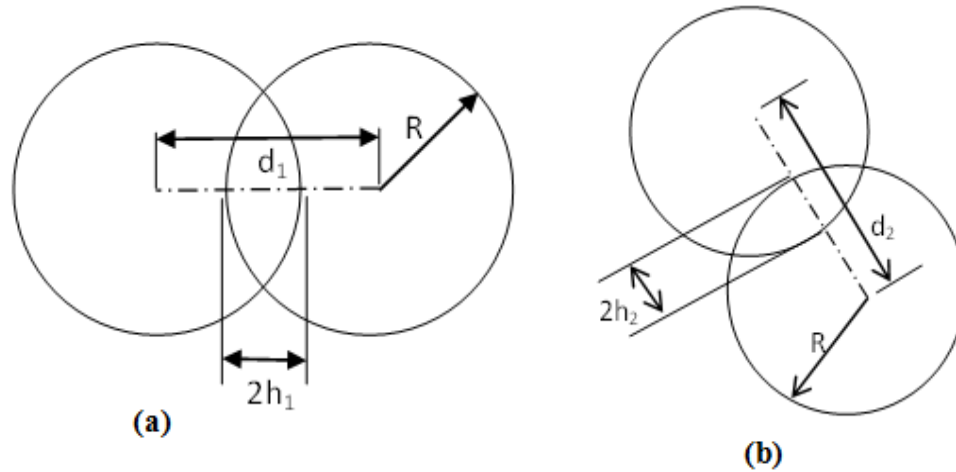


Figure 3. 3 Overlapping Two Spheres; (a) A Polar Sphere with The Central Sphere, (b) A Quadrant Sphere with The Central Sphere

where R is a sphere radius, d_1 is distance between the centers of the central sphere and polar sphere after overlapping, and d_2 is the distance between the centers of the central sphere and quadrant sphere after overlapping. The $2h_1$ is an overlapping distance of polar sphere with the central sphere, and $2h_2$ is an overlapping distance of the central sphere with quadrant sphere.

The distance d_1 can be specified by defining PPI (pore per inch). PPI is to be considered one of two independent characteristics which specify 3D dimension design of open metal foam. The second one is porosity. The average percentage of the pore diameter to the sphere or cell diameter is about 50% to 70% [38], thus the 10 PPI foam would have roughly 5 to 7 spheres in one linear inch.

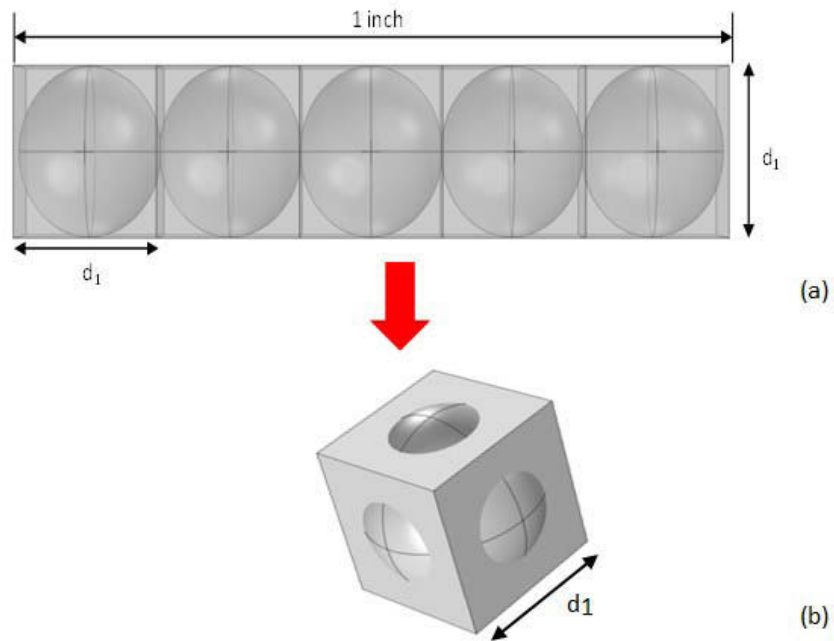
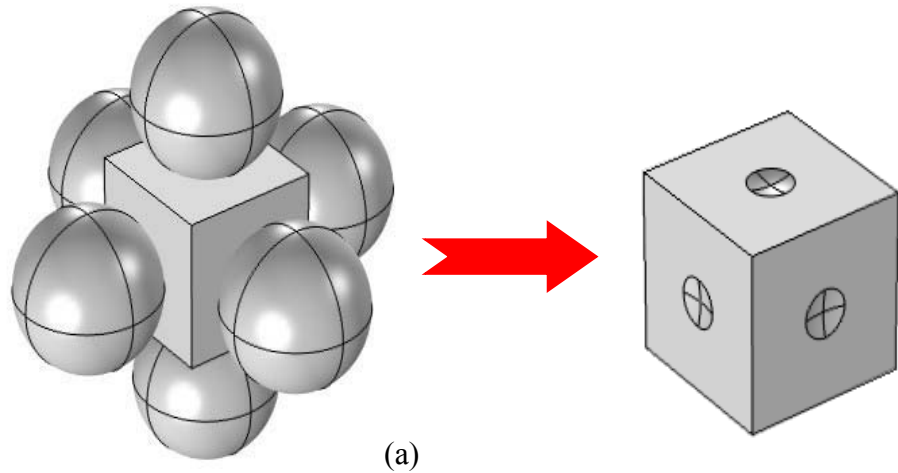
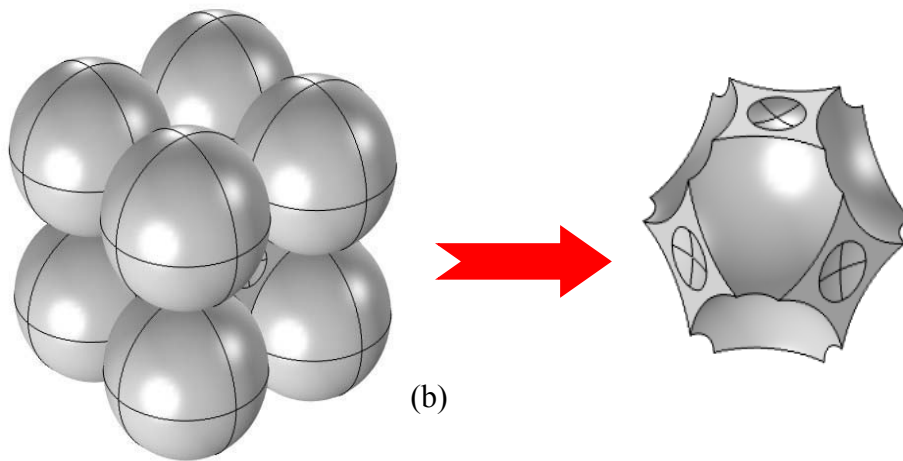


Figure 3. 4 The 10 PPI Sphere Number; (a) One Inch Consisting Five Spheres, (b) 3D View of the Central Sphere

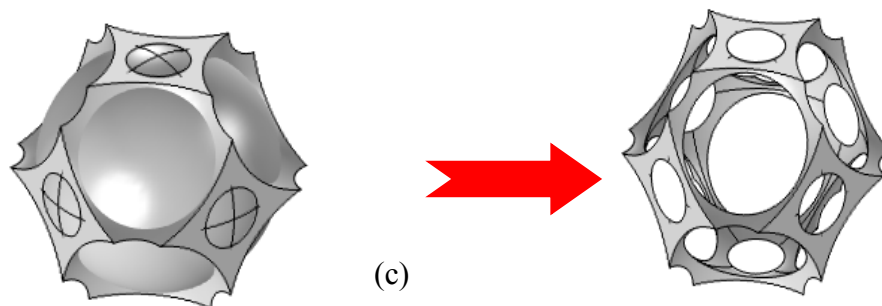
In this study, five spheres in one inch will be considered as the number of spheres per inch. For example, the 10 PPI metal foam would have 5 spheres, the 20 PPI would have 10 spheres, so on. Figure 3. 4(a) shows one linear inch having 5 spheres, which refers to the 10 PPI. Figure 3. 4(b) displays a 3D view of a central sphere with radius of R is inside a cube with length of d_1 , therefore the cube has $(d_1)^3$ volume. The ideal periodic foam geometry is obtained by subtracting fifteen spheres from the cube, as shown in Figure 3. 5.



(a)



(b)



(c)

Figure 3. 5 The Creation of Unit Cell; (a) Locations and Subtracting Spheres at Cube Faces, (b) Locations and Subtracting the Spheres at Vertices, (c) Locations and Subtracting the Central Sphere and the Ideal Periodic Unit Cell

The expression for porosity of the unit cell is given by the relation

$$\epsilon = \frac{V_{void}}{V_{cube}} = 1 - \rho_{relative} \quad (3.1)$$

Where $\rho_{relative}$ is the density of the foam divided by the density of solid origin of the ligament, V_{void} is a fraction of the cube's volume that is occupied by air or other fluid, and V_{cube} is the volume of the cube. The volume of the cube is given as

$$V_{cube} = d_1^3 \quad (3.2)$$

The length of a side of the unit cell, d_1 , is a function of the number of pores per inch (PPI) and the number of cells per inch (CPI) as:

$$d_1 = \frac{1}{CPI} \text{ (in)} \quad (3.3)$$

So,

$$V_{cube} = d_1^3 = \left(\frac{1 \text{ in}}{CPI}\right)^3 \quad (3.4)$$

For the void volume calculations, the void volume is to be a sphere located at the cube center as seen in Figure 3. 5(c). The following are subtracted from that the central sphere: (a) six overlapping caps coming from interference of the central sphere with six spheres at the cube faces as seen in Figure 3. 5(a), and (b) eight intersection volumes on the vertices of the cube as seen in Figure 3. 5(b). In addition, there are eight segments of one-eighth of sphere volume at the vertices. Each one-

eighth of sphere volume had subtracted from it an overlapping volume of the central sphere with quadrant sphere. Thus, the void volume is given by this equation:

$$V_{void} = \left(\frac{4}{3}\pi R^3 - 6V_1 - 8V_2 \right) + 8\left(\frac{1}{8}\frac{4}{3}\pi R^3 - V_2 \right) \quad (3.5)$$

where V_1 is overlapping volume of polar sphere with central sphere, V_2 is overlapping volume of quadrant sphere with the central sphere. An overlapping volume as seen in Figure 3. 6 for two overlapping spheres is given by the relation:

$$V = \frac{1}{3}\pi h^2(3R - h) \quad (3.6)$$

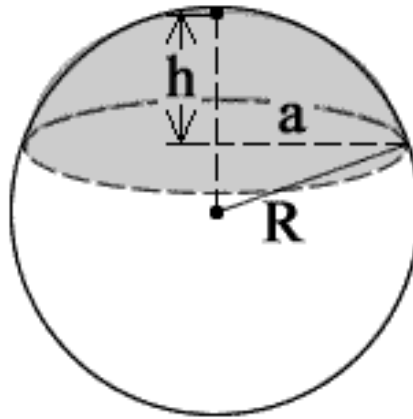


Figure 3. 6 Overlapping Volume o Two Spheres

For V_1 , the central sphere intersects with six spheres on the faces of the cube with $2h_1$ as seen in Figure 3. 3(a); thus,

$$h_1 = R - \frac{d_1}{2} \quad (3.7)$$

Then, the overlapping volume V_1 for each interfering spheres using Eq. 3.6 is:

$$V_1 = \frac{1}{3} \pi \left(R - \frac{d_1}{2} \right)^2 \left(2R + \frac{d_1}{2} \right) \quad (3.8)$$

There is another overlapping volume V_2 . The V_2 is the volume of intersecting the sphere at the center of the cube with the spheres on the vertices of the cube as seen in Figure 3. 5(a). It can be determined using Eq. 3.6:

$$V_2 = \frac{1}{3} \pi (h_2)^2 (3R - h_2) \quad (3.9)$$

where h_2 is an interference distance as seen in Figure 3. 3(b) . The h_2 can be determined in terms of d_2 as following:

$$h_2 = R - \frac{d_2}{2} \quad (3.10)$$

Figure 3. 7 shows the geometrical relationship between d_1 and d_2 .

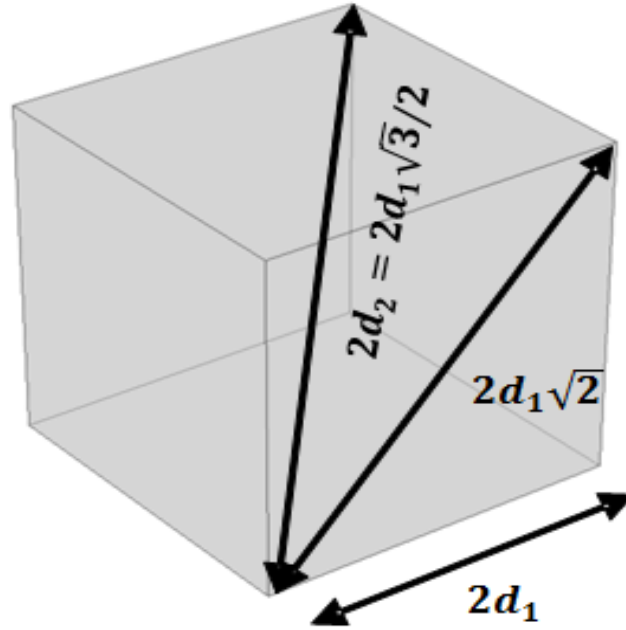


Figure 3. 7 Geometrical Relationship Between d_1 and d_2

$$d_2 = (2R - 2h_2) = d_1\sqrt{3}/2 \quad (3.11)$$

Thus,

$$h_2 = R - d_1\sqrt{3}/4 \quad (3.12)$$

Substituting Eq. 3.12 into Eq. 3.9 we get:

$$V_2 = \frac{1}{3}\pi \left(R - \frac{d_1\sqrt{3}}{4} \right)^2 \left(2R + \frac{d_1\sqrt{3}}{4} \right) \quad (3.13)$$

Substituting V_1 and V_2 into Eq. 3.5

$$\begin{aligned}
V_{void} = & \frac{8}{3}\pi R^3 - 6\frac{1}{3}\pi\left(R - \frac{d_1}{2}\right)^2\left(2R + \frac{d_1}{2}\right) \\
& - 16\frac{1}{3}\pi\left(R - d_1\sqrt{3}/4\right)^2\left(2R + d_1\sqrt{3}/4\right)
\end{aligned} \tag{3.14}$$

Also, the porosity is given by the relation

$$\begin{aligned}
\epsilon = & \frac{1}{d_1^3}\left[\frac{8}{3}\pi R^3 - 6\frac{1}{3}\pi\left(R - \frac{d_1}{2}\right)^2\left(2R + \frac{d_1}{2}\right)\right. \\
& \left. - 16\frac{1}{3}\pi\left(R - \frac{d_1\sqrt{3}}{4}\right)^2\left(2R + \frac{d_1\sqrt{3}}{4}\right)\right]
\end{aligned} \tag{3.15}$$

Equation (3.15) has two unknown variables, porosity (ϵ) and sphere radius (R), that must be solved by the trial and error method. We use a built- in Solver in *Excel*[®] named Solver to handle it. Then, a Computer-Design-Aided (CAD) package, *SolidWork2010*[®], can be used for creating the BCC geometry.

3.2 Geometrical Characterization Verification

Transfer phenomena in metal foam strongly depend on a geometrical model of a solid matrix. There are several parameters to characterize the internal structure of metal foam:

3.2.1 Porosity

Porosity is defined as the ratio of interconnected pore volume or void space that can contain fluid to the total volume.

$$\epsilon (\%) = \frac{V_f}{V} \cdot 100 = \frac{V_f}{V_f + V_s} \cdot 100 \quad (3.16)$$

where ϵ is a porosity, V_f is the volume of void or fluid, and V_s is the volume of solid. The porosity of the unit cell calculated using the CAD tools in Figure 3. 2 is 97.8 %. This is very close to the given porosity in Eq. 3.15.

3.2.2 Specific Surface Area

Specific surface area is the ratio of interfacial area to the total volume

$$\sigma = \frac{A_{sf}}{V} = \frac{A_{sf}}{V_f + V_s} \quad (3.17)$$

where A_{sf} is the surface area of a solid. The specific surface area of the unit cell calculated using the CAD tools in Figure 3. 8 is 460 m²/m³. The measured specific surface area by ERG [32] being 660 m²/m³. The relative error between model and measured specific surface area is 30.3 %.



Figure 3. 8 Specific Surface Area is Calculated by CAD Tools of Current Geometrical Model.

3.2.3 Cell and Pore

The internal structure of open celled foam is an array of cells connected to each other by ligaments. Each cell has 14 pores or windows, and it has a shape called a tetrakaidecahedron as seen in Figure 3. 9. The pore's shapes and diameters are different within a given cell. To simplify, the shape of pores are approximated as a circle with an average diameter for all 14 pores' diameter. PPI is used as an independent characteristic beside the porosity or relative density to define or specify foam. An average pore diameter is about 50% to 70% of the diameter of its parent cell; thus, 10 PPI foam would have roughly 5 to 7 bubbles per inch. In this work, 5 cells per inch for 10 PPI is used as seen in Table 3. 1

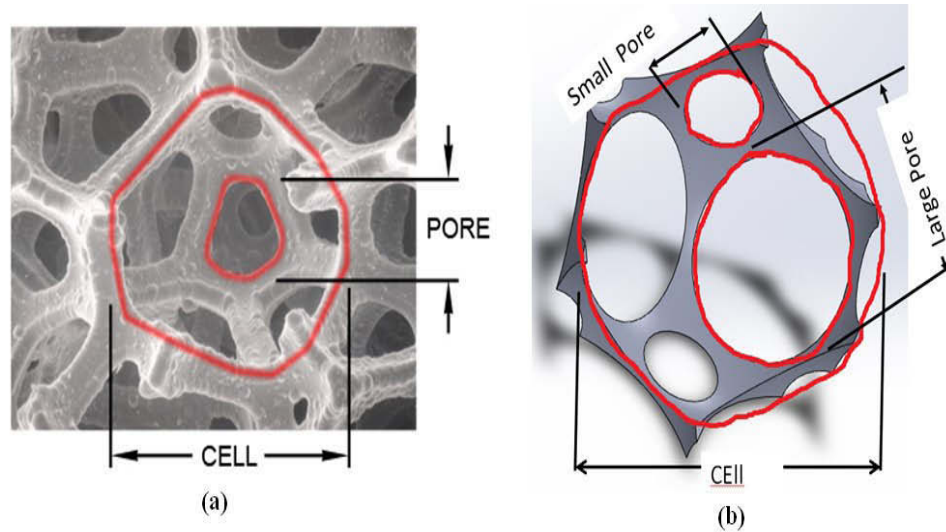


Figure 3. 9 Pore and Cell Shape. (a) ERG [38],(b) Current Geometrical Model

Table 3. 1 Current Model & ERG [38] Foam Parameters

	ERG[38]	Current Model	Error %
Average pore Diameter (in)	2.54	2.2	15
Cell Diameter (mm)	0.2	0.207	3.3

3.2.4 Ligament

The shape and size of a ligament's cross section are influenced by the porosity or the relative density. As the porosity increases, the ligament's cross section shape changes. The ligament's cross section is circular at a low porosity, 85% , while at a high porosity, 97% or more ,the cross section is triangular as seen in Fig [38].

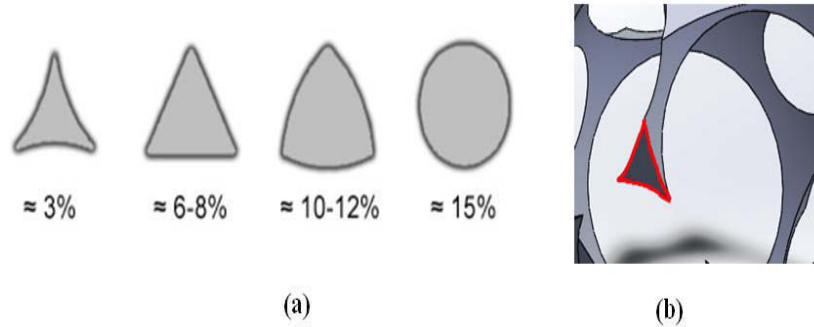


Figure 3. 10 The Ligament Cross Section for Current Geometrical Model and ERG. (a) ERG [38] at Different Relative Densities, (b) The Current Geometrical Model at 2.2% Relative Density.

The diameter of a ligament is calculated by taking an average of its diameters along the length of the ligament as seen in Figure 3. 11(a).

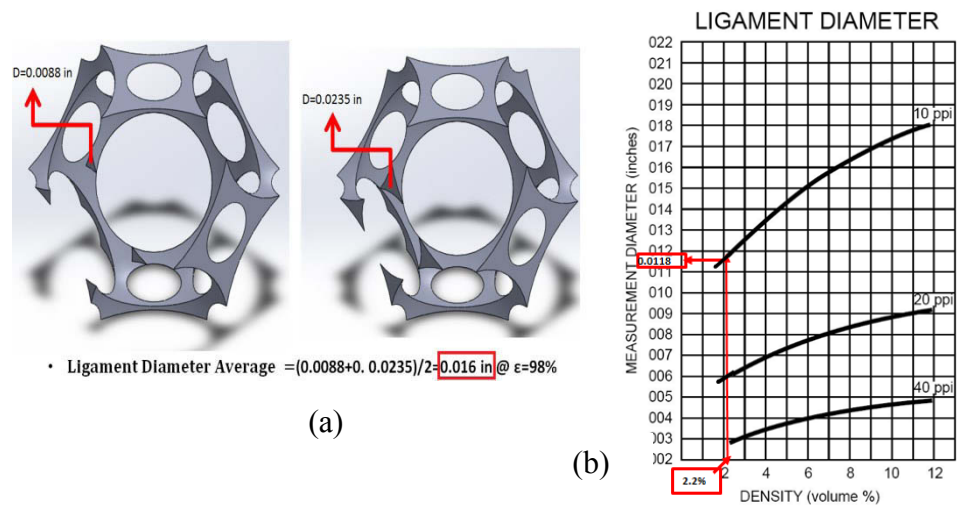


Figure 3. 11 Ligament diameter (in). (a) Current geometrical model; (b) ERG[38]

The size of ligament diameter is about 0.016 in at 97.8 % porosity or 2.2 % relative density and 10 PPI, while ERG [38]ligament’s diameter is 0.0118 in as shown in Figure 3. 11(b). The relative error between current model ligament diameters to the measured diameter of ERG[38]is about 26 %.

Chapter 4: Numerical Simulation of Flow Field for One Cell

This chapter describes the numerical experiment method that has been developed for simulating fluid flow through a unit cell model, using the commercial software COMSOL[®].

In most recent studies, hydrodynamic properties of metal foam, such as permeability, inertial coefficient, and friction factor, are measured numerically in two different approaches: macrostructure approach and microstructure approach (pore-level scale).

It was decided that the best approach to adopt for simulation fluid flow was to directly apply and solve the governing equations at the pore-level scale, which has become feasible with rapid advances in computing power. Obtaining a numerical approximation solution of fluid dynamics in metal foam by the use of a CFD program is the only choice due to the complexity of metal foam structure. This procedure has been used by many authors [22,27,29,31,33–35,37] In order to understand how pressure drop through metal foam changes with inlet velocity, a series of numerical runs for only one cell model was performed using COMSOL. COMSOL is powerful commercial CFD software and is utilized for such analysis. COMSOL models a wide range of phenomena by solving the conservation equations for mass, momentum and energy using the finite element method.

4.1 Overview COMSOL

COMSOL is a commercial multiphysics software used to simulate one phenomenon, such as conduction/convection heat transfer, fluid flow or coupled physics: for instance, fluid flow with chemical reactions or fluid flow with heat transfer or all of them together, fluid flow, heat transfer, and chemical reactions. COMSOL has a number of built-in modules. Each module can model a wide range of physical configurations. Take the CFD module as an example. The CFD module can model single or two phase flow, including 2D/3D geometries in Cartesian and cylindrical coordinates; steady state or transient; incompressible or compressible flow; laminar or turbulent flow, isothermal laminar / turbulent, and flow through porous media.

Three main processes are used in COMSOL to simulate the proposed models:

4.1.1 Pre Processing

Model wizard (Selecting space dimension, adding physics and selecting study type)

- Geometry (Importing a unit cell & creating a physical domain)
- Materials (Physical properties of fluid and solid)
- Physics (Setting phenomena and selecting boundary conditions)
- Meshing (Customizing mesh parameters)

4.1.2 Processing (Study)

- Parametric Sweep
- Choosing Solver
-

4.2.3 Post Processing (Results)

- Displaying Plots
- Creating Data Sets
- Deriving Values
- Constructing Tables

Model Descriptions

4.1.3 Physical Domain

The metal foam structure, as a unit cell with 97 % porosity and 10 PPI, is placed inside a rectangular channel, Figure 4. 1. Then, the unit cell was subtracted from the rectangular channel in order to get the fluid domain or physical domain where Navier-Stokes equations are applied and solved using a built-in function called Solver in COMSOL 4.3.

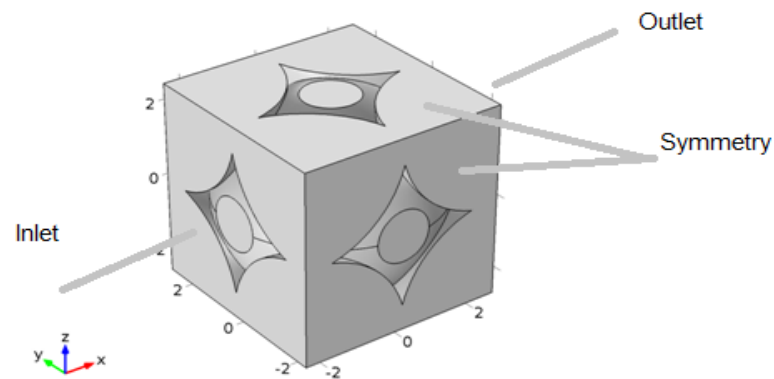


Figure 4. 1 Schematic of Physical Model

In the first step, open cell metal foams are represented by the simplified model structure, using only one BCC cell structure, as shown in Figure 4. 1, then by scaling the computational domain by arraying BCC cells in 3D directions:

- 1) 2x2x2 cells
- 2) 4x4x4 cells
- 3)

4.1.4 Laminar flow

The flow was assumed to be laminar, steady, and incompressible. Air was used as the working fluid (with density of 1.2 kg/m³ and a viscosity of 1.814x10⁻⁵ Pa.s).

The geometrical model shown in Fig.4.1 was defined as the fluid zone involving only one unit BCC type cell. The fluid inlet was set at x = -2.54 mm and the outlet was set at x = 2.54mm.

Before meshing the computational domain, the boundary conditions should be determined and set at each face. Many types of boundary conditions can be chosen, depending on the user case study.

The following boundary conditions are applied for fluid flow analysis:

- constant fluid velocity at the inlet of the porous channel.
- constant fluid pressure 0 (bar) at the outlet of the porous channel.
- zero fluid velocity (no-slip) on aluminum foam internal surface.
- symmetry on all outer surfaces of the porous channel.

The metal foam structure was modeled using COMSOL, which solves the momentum and mass equations augmented by Navier-Stokes equations :

$$\rho \nabla \cdot u = 0 \quad (4.1)$$

$$\rho(u \cdot \nabla)u = \nabla \cdot [-pI + \mu(\nabla u + (\nabla u)^T)] + F \quad (4.2)$$

where u is the fluid velocity, p is the fluid pressure, μ is the fluid viscosity, ρ is the fluid density, I is the identity matrix and F is body forces.

4.1.5 Meshing and Solving

The computational domain or physical domain is then meshed using tetrahedral elements (3D). A finer mesh is applied to areas on the porous cell surface to account for the large gradients that occur in these areas, as shown in Figure 4. 2. A mesh dependence study will be presented later.

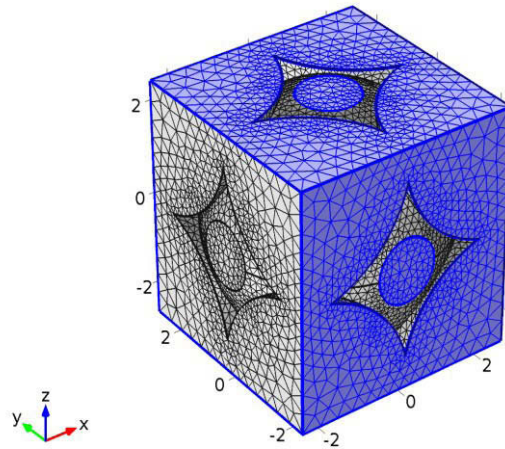


Figure 4. 2 Mesh Grids in Unit Cell Model for Fluid Flow

All the corresponding parameters are set, and the simulation is run until the data are converged.

4.1.6 Results

The Solver used in COMSOL allows for prediction of velocity distribution within the porous 3D structure. Data sets were obtained for various inlet velocities. Overall pressure drop calculations were then used to characterize the relation between the flow rates and the pressure drop.

Figure 4.3 shows the fluid flow streamlines colored by velocity magnitude for a free stream fluid with a velocity of 1.28 m/s. The fluid flows along the x- axis in the positive direction. The presence of the metal foam in the channel reduces the cross-sectional area available for fluid flow and increases fluid velocity. It can be noticed that the maximum fluid velocity in the porous channel is about 1.5 times higher than the free stream inlet velocity. This, in turn increases the pressure drop per unit length. The tortuosity of the fluid flow streamling around the foam ligaments is observed in the simulations, as shown in Fig.4.3

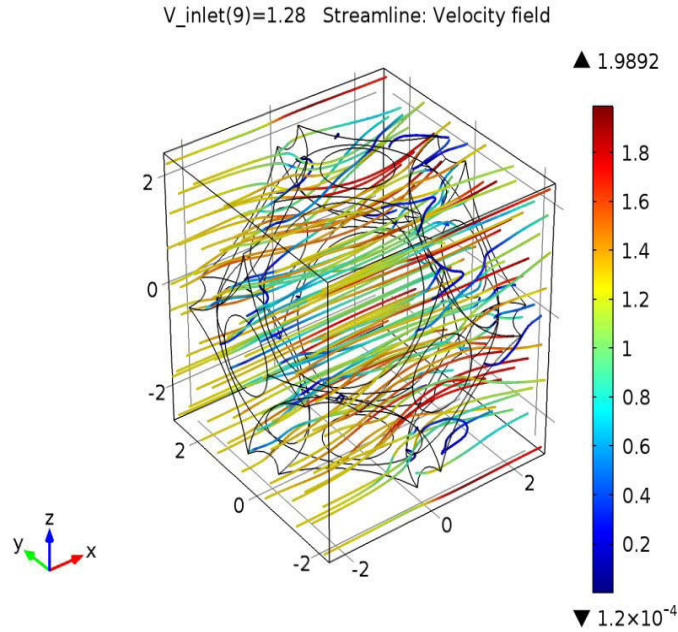


Figure. 4. 3 Fluid Flow Streamlines in the Porous Channel Colored by Velocity Magnitude for a Free Stream Velocity of 1.28 m/s.

The simulation results of pressure drop per unit length across the metal foam as a function of free stream fluid velocity are shown in Figure 4. 4 as discrete points. Quadratic curve is fitted through the data points using the least square method, and its equation is also shown in Figure 4. 4. It can be noticed that the simulation results of pressure drop per unit length can be represented by a quadratic dependence on free stream velocity, which is in agreement with the Forchheimer equation. By comparing the curve equations in Figure 4. 4 with the Forchheimer equation (Equation (4.3)), the values of permeability and inertial coefficient for the foam can be calculated. The values of these two quantities are listed in Table 4. 1 Permeability and Form Drag

$$\frac{\Delta p}{L} = \frac{\mu}{K}V + \rho CV^2 \quad (4.3)$$

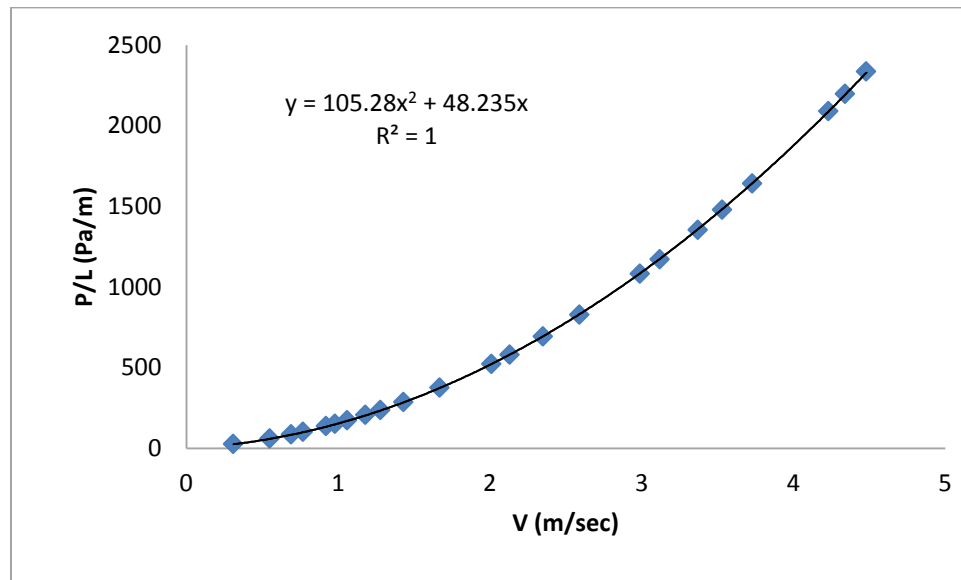


Figure 4. 4 Pressure Drop per Unit Length as a Function of Free Stream Velocity for a Unit Cell

Table 4. 1 Permeability and Form Drag

Geometrical properties	K (10^{-7} m^2)	C (1/m)
Porosity 97% , 10 PPI	3.76	88.75

Chapter 5: Simulation of Fluid Flow

5.1 Introduction

In this chapter, simulation of fluid flow for computational domain (or subdomain) using COMSOL is considered. Numerical results were obtained in terms of velocity profiles and pressure drop. The numerical pressure drop of the computational domain was compared to experimental pressure drop for actual foam obtained in the lab.

5.2 Physical Fluid Flow Problem

Consider a channel filled with open-cell porous media (or metal foam) as shown in figure 5.1. The channel has height $2H$ and length L . Inside the porous medium, there is a one-dimensional fluid flow in the positive x direction with velocity u .

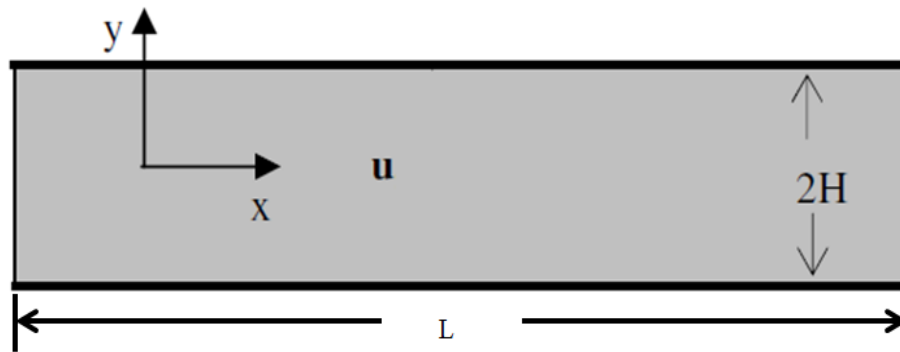


Figure 5. 1 Schematic of Fluid Flow Problem

The following boundary conditions were applied for fluid flow analysis:

- Constant fluid velocity at the inlet of the porous channel.
- Constant fluid pressure at the outlet of the porous channel (0 bar).
- Zero fluid velocity (no-slip) on the foam internal surface.
- Symmetry at the center of the porous channel.

The following mass and momentum conservation equations were used :

$$\rho \nabla \cdot u = 0 \quad (5.1)$$

$$\rho(u \cdot \nabla)u = \nabla \cdot [-pI + \mu(\nabla u + (\nabla u)^T)] + F \quad (5.2)$$

where p is the fluid pressure, μ is the fluid viscosity, ρ is the fluid density, I is an identical matrix and F represents body forces.

5.3 Computational Domain Creation

In general, solving the flow field at pore scale for the entire physical domain, as seen in Fig.5.1, is impractical due to its requirement of large computing resources, even though it would reflect accurate details of the microstructure foam. The flow field at pore scale for subdomain , as shown in Fig.5.2, should be exactly representative of the bulk material, i.e. it has to be large enough to characterize the material properties (density, porosity, PPI, etc.) as the bulk material, and small enough to maintain spatial description.

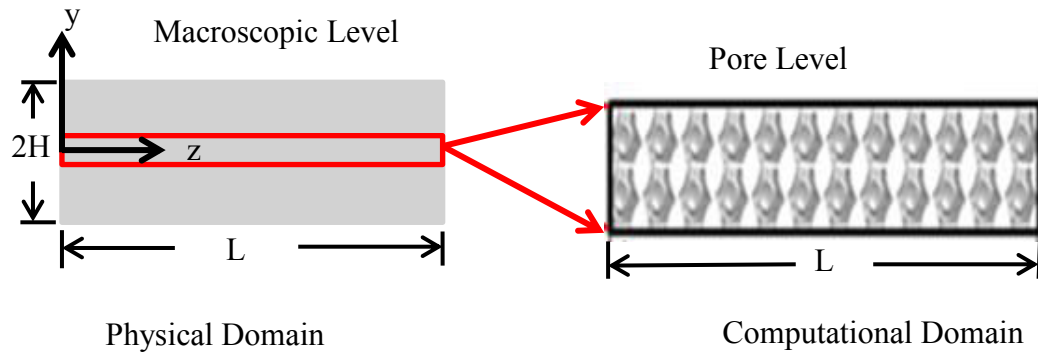


Figure 5. 2 Pore Level Domain

The computational domain of metal foam was built by using BCC unit cell as mentioned in Chapter 3. Due to limitation of available computational resources, and keeping the computational domain reasonable within that constraint, only 101.6 mm x 5.08 mm x 5.08 mm was built to represent an actual metal foam sample 101.6 mm x 101.6 mm x 101.6 mm shown in figure5.3.



Figure 5. 3 10 PPI Duocel® Aluminum 6101 Alloy Metal Foam, 90.2 % Porous

The computational domain consists of solid and fluid domain. The solid domain represents metal foam structure, and the fluid domain represents working fluid through the metal foam. For the solid domain, a matrix of 1x 20 BCC unit cells having 97.3 % porosity and 10 PPI was used. In order to construct the fluid domain, rectangular channel is used with a 101.6 mm height, 5.08 mm width and 5.08 mm depth. The matrix was placed inside the rectangular channel. Then, this matrix was subtracted from the rectangle that contained it, as shown in Fig.5.4.

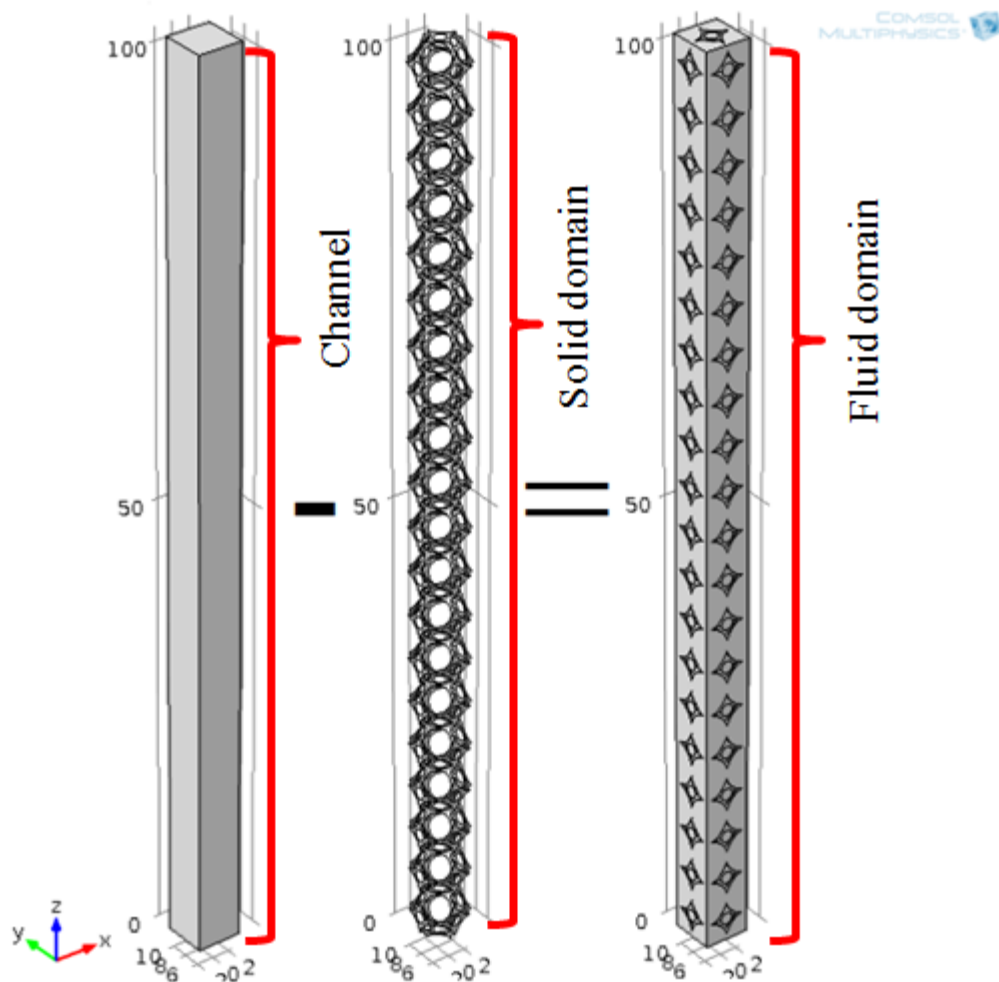


Figure 5. 4 Creation of Computational Domain

The geometrical parameters (porosity and specific surface area) can be calculated using measurement tools available in COMSOL as seen in Table 5. 1.

Table 5. 1 Foam Parameters

Size [mm]	Pore Diameter D_p[mm]	Porosity ε %	Specific surface area σ [mm²/mm³]
Simulation 5.08x5.08x101.6	2.15	97	458
Experiment 101.6x101.6x101.6	2.54	91.2	857

5.4 Numerical Simulation

5.4.1 Flow Phenomenon

For simulating fluid flow through the final geometrical domain representing computational domain as shown in Fig.5.5, the commercial software COMSOL was used. The flow was assumed to be laminar [39], steady, and incompressible. Air was used to represent computational domain and entered the computational domain as seen in fig.5.5 at room temperature (295.15 k) properties with density of 1.2 kg/m^3 and a viscosity of 1.1814×10^{-5} .

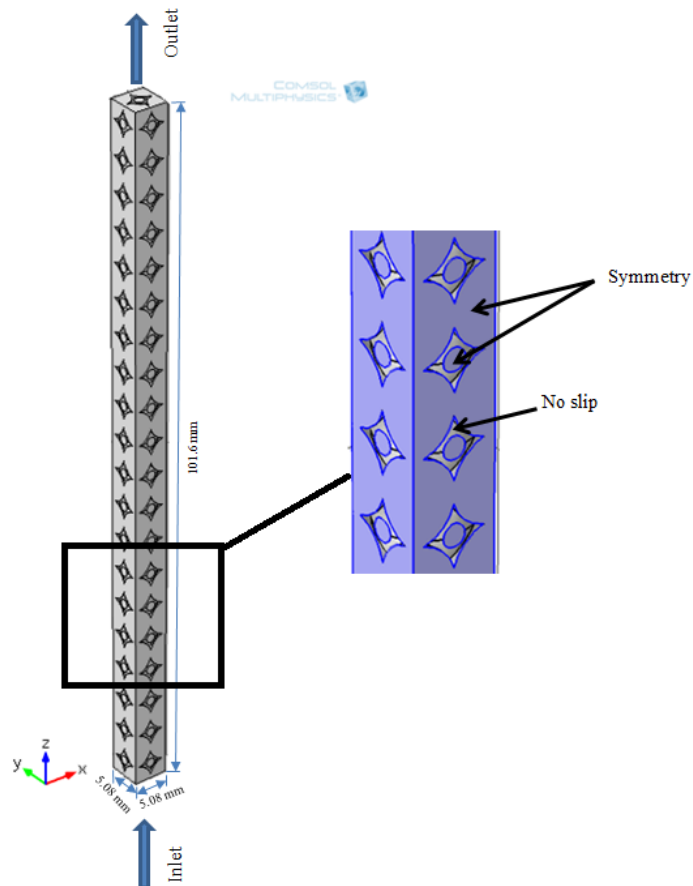


Figure 5. 5 The Computational Domain and Boundary Conditions in 3D

It should be noted that all flows in this chapter with inlet velocity ranging 0.31 m/s to 4.48 m/sec are considered to be laminar flows[39]. Dukhan and Ali [39] used the classical definition of Reynolds number for making the transition to turbulence for channel flow:

$$\frac{\rho V D_h}{\mu} \quad (5.3)$$

where D_h is the hydraulic diameter of the channel, $D_h = 4A/P$ is the hydraulic diameter defined as four times the ratio of the cross-sectional flow area divided by the wetted perimeter, P , of the channel.

5.4.2 Boundary Conditions

Boundary conditions for the computational domain were defined by explicitly assigning data in the boundary condition panels. A uniform velocity profile was applied ranging from 0.31 to 1.18 m/s seen in Table 5. 2 normal to the inlet boundary of the computational domain as seen in Fig. 5.5. The gauge pressure (static pressure) of the environment to which the flow exits was 0 bars, and assigned to outlet boundary. Flow field and geometry were considered to be symmetrical, and no inputs were required, i.e. pressure or velocity. Thus, symmetry boundaries on all outer surfaces of the channel or computational domain were applied. Symmetry boundaries mean zero normal velocity at symmetry plane, and zero normal gradients of all variables at symmetry plane. In viscous flows, no slip conditions - zero fluid velocity- were applied at walls or the foam's internal surface.

5.4.3 Meshing and Mesh Dependence

The finite element method works by dividing the complex CAD (Computer Aided Design) shape up into smaller pieces, or elements, over which it is easy to approximate the solution via polynomials.

In general, any 3D part can be meshed using tetrahedral element as seen in Fig.5.6 (a). There are other kinds of elements that can be used such as; hexahedral and prismatic elements which are seen in Fig.5.6 (b, c respectively). They are more appropriate for certain geometries, i.e. less complex geometries than tetrahedral element. Hexahedral and prismatic elements are also used when solution is known to vary slowly in one axis, and when there are contact problems. In this computational domain, tetrahedral element was used due to complexity of geometrical domain in terms of sharp edges and narrow regions.

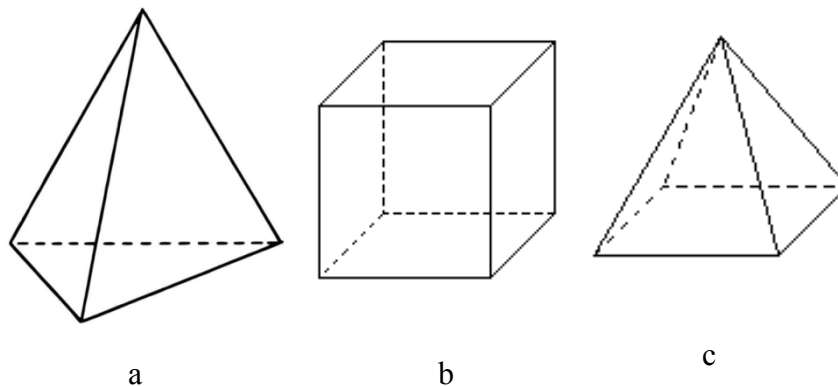


Figure 5. 6 Element Kinds. a) Tetrahedral Element. b) Hexahedral Element. c) Prismatic Element

Mesh independence was established to ensure that the solution or results is/are independent of the mesh size. To confirm mesh independence, the same

computational domain was spatially discretized using three meshes of varying refinement.

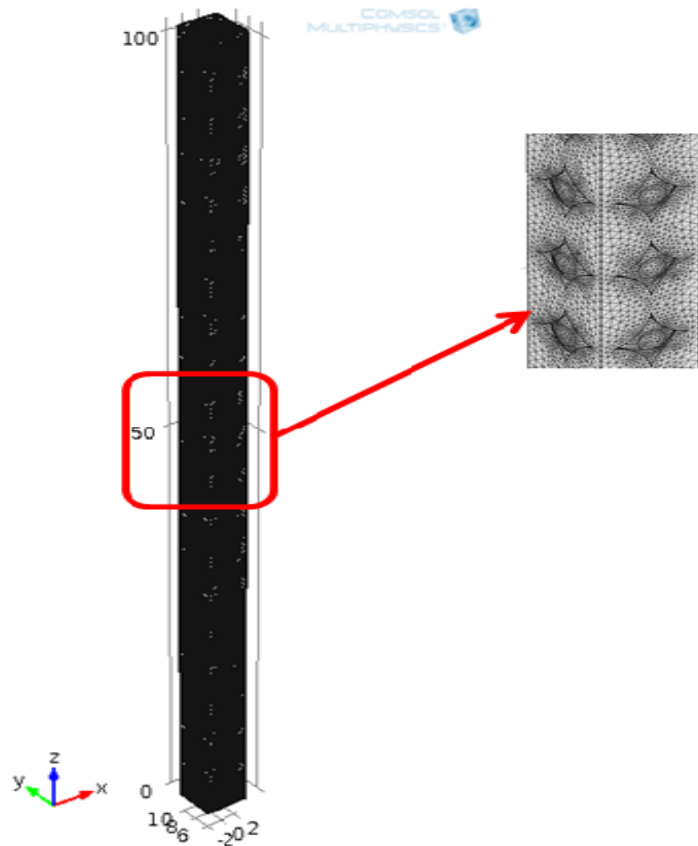


Figure 5. 7 Meshing

The Three different unstructured tetrahedral element meshes were generated with commercial software COMSOL. Coarse mesh consists of 651,340 elements; medium mesh consists of 918,016 elements; and fine mesh consists of 1,234,420 elements. All meshes were applied to the present computational model of Fig.5.7.

Figure 5.8 displays mesh details near both the wall and the surface of porous media for the coarsest and finest cases. The coarsest mesh was refined up to 2 times to perform the mesh independence study, as seen in Table 5.2

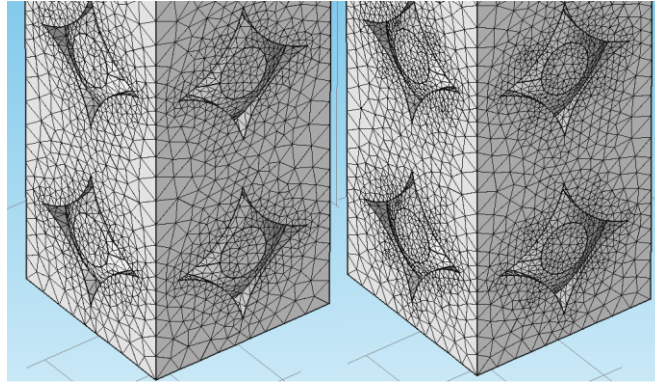


Figure 5. 8 Details of Volume Mesh of Cells at the Coarse and Fine Meshes

The pressure drop along flow direction also was calculated to provide more comparisons of the simulation results, as seen Table 5. 2. The relative error of pressure drop between the coarsest and finest mesh is 2.9 %, while the relative error of pressure drop between medium and fine is 2.3 %, as shown in Fig.5.9.

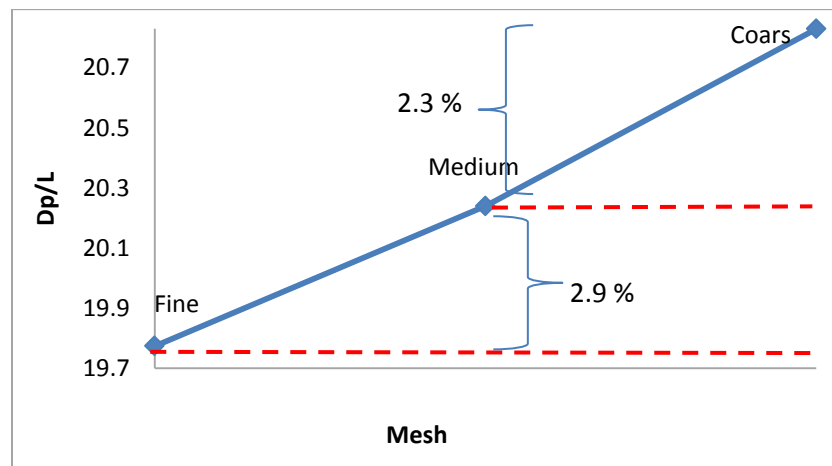


Figure 5. 9 Pressure Drop at Different Meshes and V=0.31 m/sec

Table 5. 2 Meshing levels with their number of elements and pressure drop at V= 0.31 m/sec

Mesh	No. Element	Dp/L (Pa/m)
Coarse	651,340	19.8
Medium	918,016	20.2
Fine	1,234,420	20.8

Flow velocities in flow direction for the same entrance velocity 0.31 m/s at 2 inches from the inlet were 2.7 % between the medium and the coarse meshes, and 0.25 % between the medium and the fine meshes. Thus, the results of the medium mesh were deemed mesh-independent; and the medium mesh was used for all subsequent studies. The simulation was run until convergence, which took five hours and six minutes. The computer used for simulation ran on a 64-bit operating system, with a processor operating at 3.40 GHz and 31.7 GB of usable RAM.

5.5 Results

Figure 5.10 shows cross-sectional slices perpendicular to the flow direction at different locations along the flow direction (the positive z-direction). Each slice is colored by the velocity magnitude for an inlet fluid velocity of 1.18 m/s. The presence of the metal foam in the channel reduces the cross-sectional area available for fluid flow and increases the fluid velocity. It can be noticed that the maximum fluid velocity inside the foam is about 1.5 times higher than the inlet velocity (dark red regions). These regions are typically close to small pores (or windows), where the flow must accelerate. Also noticeable in this figure are regions of very low velocity (light blue) and stagnation regions (dark blue) where the velocity is essentially zero. These regions are close to the solid ligaments of the foam. This behavior is expected due to the no-slip condition imposed on the solid-fluid interface.

Figure 5.11 is a plot of streamlines of the fluid inside the simulated foam colored by the velocity magnitude. The tortuosity of the porous medium is shown by the winding flow streamlines around the foam ligaments, which leads to mixing. However, there are areas of the flow that permit undisturbed (aligned) flow paths through the pores or the windows. This is especially true around the central area of the cells. Some flow paths severely divert from the macroscopic one-dimensional main flow direction (z-direction).

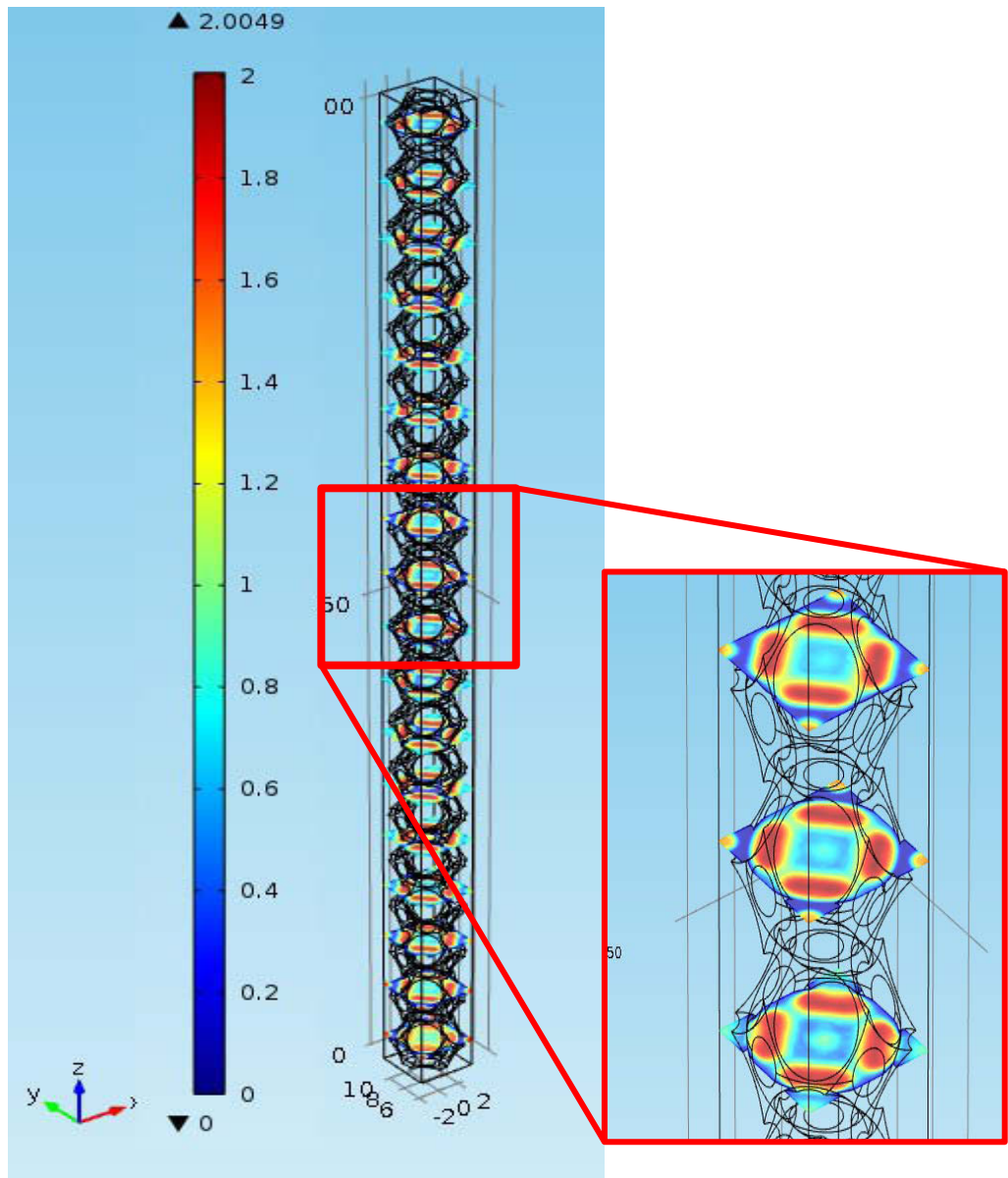


Figure 5. 10 Cross-Sectional Slices Colored by Velocity Magnitudes for an Inlet Velocity of 1.18 m/s.

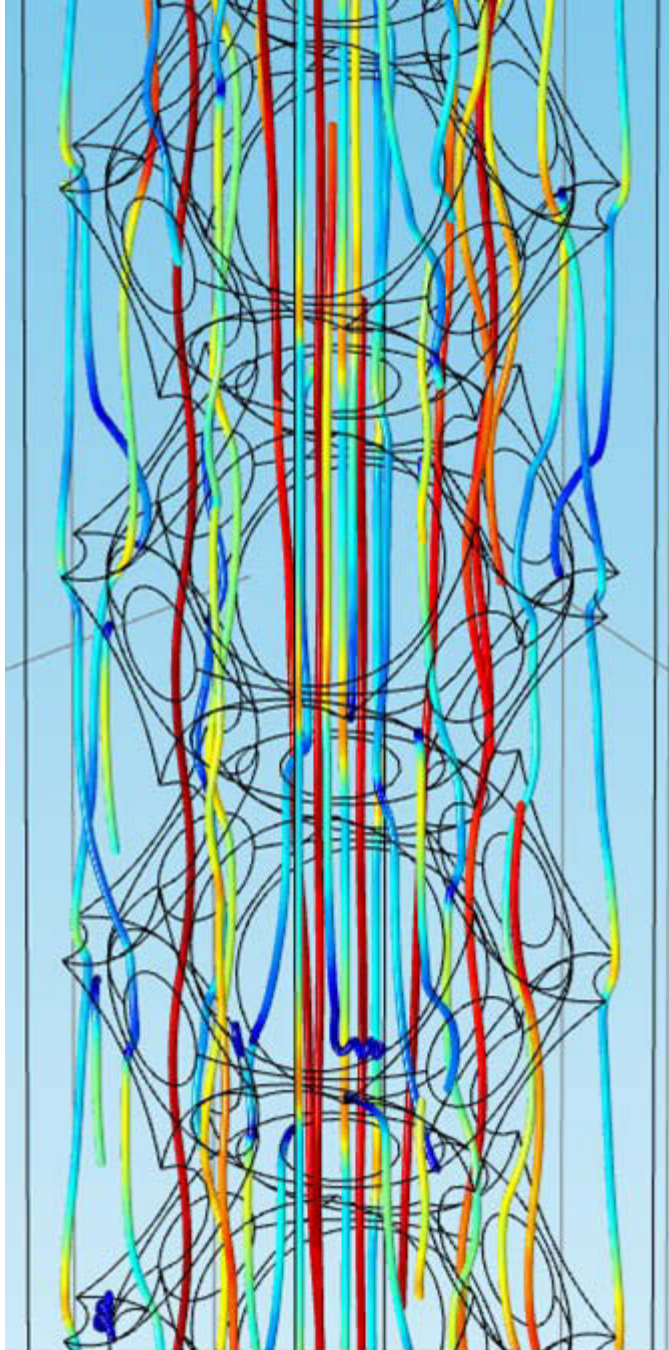
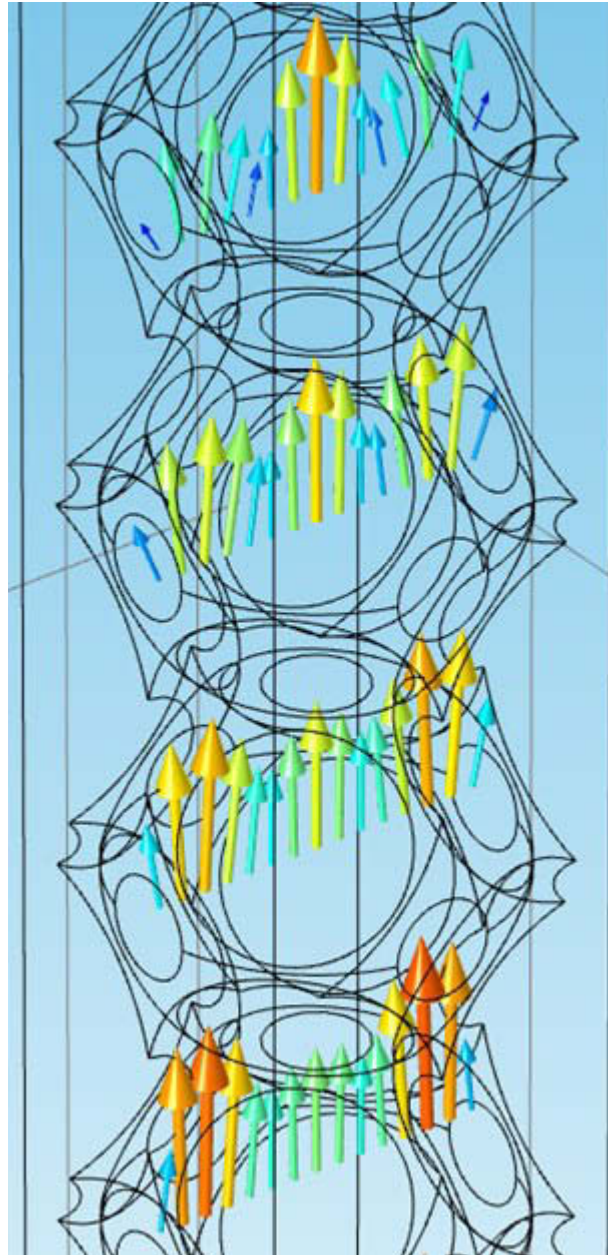


Figure 5. 11 Streamlines Colored by Velocity for an Inlet Velocity of 1.18 m/s.

Figure 5.12 is a plot that shows the velocity vectors in an x-z plane passing through the center of the simulation domain. The magnitude of the velocity at every location is signified by the size and the color of the arrows. This figure provides

another way of visualizing the accelerated and the decelerated flow regions within the cells. The plot also shows the orientation of the velocity



**Figure 5. 12 Velocity Vector at an x-z Plane Passing through Middle of the Domain for an Inlet
Velocity of 1.18 m/s.**

5.6 Experimental Validation

5.6.1 Experiment Set Up

The pressure drop was measured in an open-loop wind tunnel shown in Fig.5.13. A direct-drive 0.5-horsepower blower draws ambient air through the tunnel. As one flow rate control, a piece of Plexiglas is used to partially block the outlet area of the blower. For further control of the flow rate, and hence the velocity in the test section and through a foam sample, a variable speed controller is used. A reducing section connects the inlet of the blower to the rest of the tunnel.

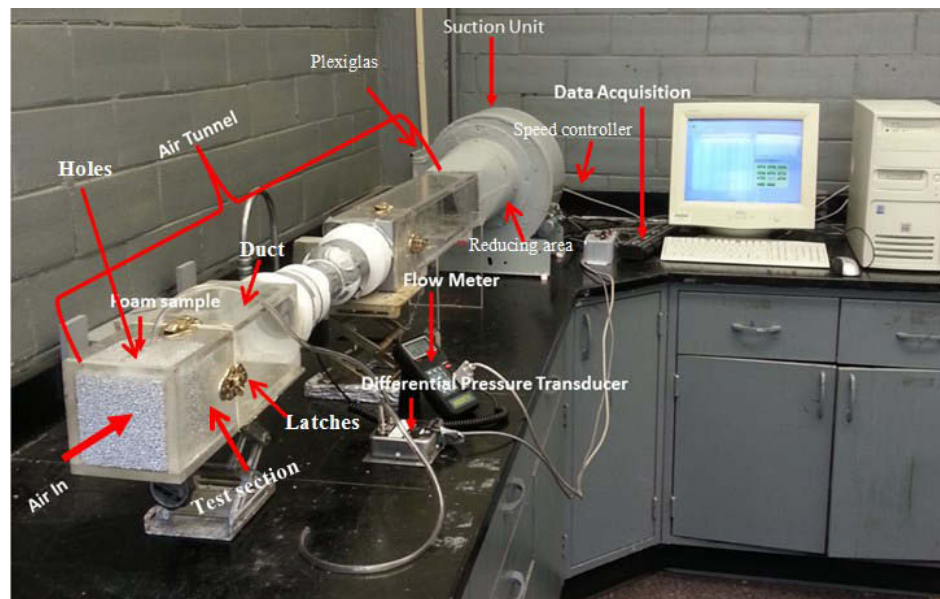


Figure 5. 13 Experimental Testing Equipment Setup

The test section is fabricated from Plexiglas and has a square inside cross section of 10.16 cm by 10.16 cm. The test section is placed securely to square duct using a set of four latches. Each duct has a length of 152.4 cm.. Two holes are drilled at the center of the top acrylic sheet separated by a distance of 2.54 cm (1 in). The diameters

of these holes are 0.79 cm and they hold pressure differential tubing. The pressure drop is measured using an Omega differential pressure transducer. Depending on the air velocity the pressure transducer can be model PX653- 10D5V, which has a range of 0 to 2,487 Pa, or model PX653-03D5V, which has a range of 0 to 746 Pa. For flow measurements, an Extech Heavy Duty CFM Metal Vane flow meter is used. This meter has power input 15-18 VDC and output 4-20 mA.

A sample of commercially available aluminum foam as shown in figure.5.3 (manufactured by ERG Materials and Aerospace) was investigated. The sample had a cross-sectional area of 10.16 cm by 10.16 cm. Other foam parameters are given in Table 5. 1. The sample was made from aluminum alloy 6101-T6.

The sample was placed in the tunnel's test section. The flow rate was varied to realize different velocities at the test section inlet. For each velocity, the static pressure drop was measured using the pressure transducers.

The uncertainty in the measured pressure drop had a contribution from a fixed error ($e_f = 10.8\%$) and an error in each reading ($e_r = 0.2\%$), as reported by the pressure transducer's manufacturer. The root-sum-squares method [34] states that total uncertainty in the pressure values δp is given by

$$\delta_p = \mp \sqrt{e_f^2 + e_r^2} \quad (5.4)$$

This results in δ_p of 10.8%. The average air velocity in the tunnel was measured using an Extech metal vane meter. The reported uncertainties by the manufacturer included a fixed error of $\pm 2\%$ and an error of ± 0.2 m/s of the reading. Using the root-

sum-squares method and a conservative representative velocity of 2 m/s, the relative uncertainty in the air velocity is 10.2%.

5.6.2 Comparison

The pressure drop per unit length obtained from the simulation is compared to that obtained experimentally. These two pressure drops are plotted against the Darcy velocity in Fig.5.14. The pressure drop is seen to increase as the Darcy velocity through the foam increases. This trend is evident and expected for both simulation and experiment. . Actually Darcy law dictates that

$$\frac{\Delta P}{L} = \frac{\mu}{k} V \quad (5.5)$$

As the velocity increases the form (or inertial) drag becomes significant and the Forchheimer extension is added:

$$\frac{\Delta P}{L} = \frac{\mu}{k} V + \rho C V^2 \quad (5.6)$$

where Δp is the pressure drop, L is the length of the porous medium in the flow direction, μ is the fluid viscosity, k is the permeability of the porous medium, ρ is the density and C is a form drag coefficient. The Darcy velocity V is a superficial quantity calculated by dividing the volumetric flow rate by the open cross-sectional area.

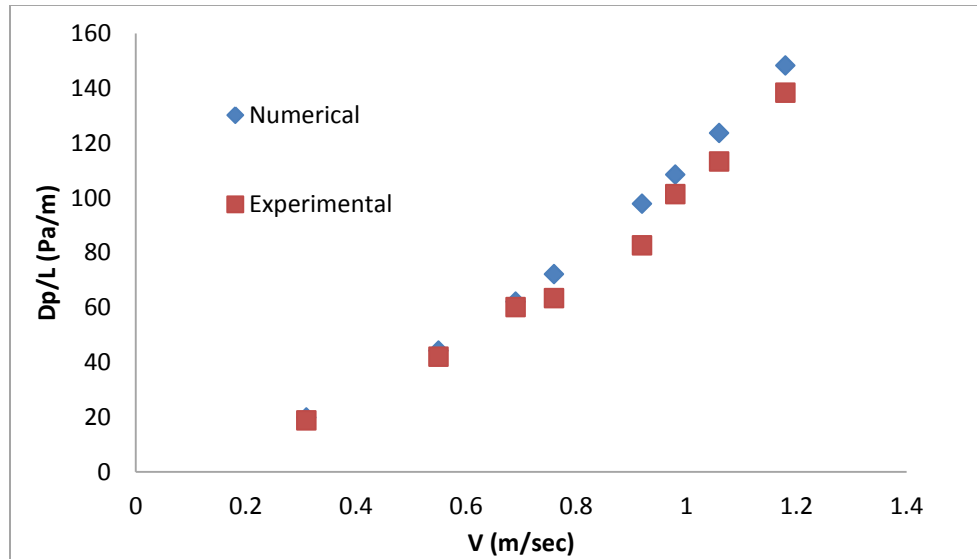


Figure 5. 14 Pressure Drop from Numerical and Experimental Studies of 10 PPI and 97% Porosity Foam

The agreement between the results obtained experimentally and those obtained by the geometrical modeling and simulation is rather good. Table 5.3 shows the percentage difference between the two. The maximum difference is around 15.5%, which is acceptable. This lends confidence to the simulation used in the current study.

**Table 5. 3 Experimental Normalized Pressure Drop with Numerical for Low Velocity Regime for 10
PPI and 97% Porosity Foam**

Inlet Velocity (m/sec)	Numerical Dp/L (Pa/m)	Experimental Dp/L (Pa/m)	Difference %
0.31	19.77	18.75	5.16
0.55	44.21	41.99	5.02
0.69	62.11	60.10	3.24
0.76	72.13	63.38	12.12
0.92	97.82	82.67	15.48
0.98	108.48	101.31	6.61
1.06	123.60	113.25	8.37
1.18	148.21	138.31	6.67

5.7 Model Limitations

The agreement between the results obtained experimentally and those obtained by the geometrical modeling and simulation seems to weaken as the velocity increases. This can be explained by the geometrical difference between the idealized unit cell and the actual cell of aluminum foam. This difference affects the flow field with this influence getting stronger as the velocity increases as seen in Fig.5.15 and Table 5.4.

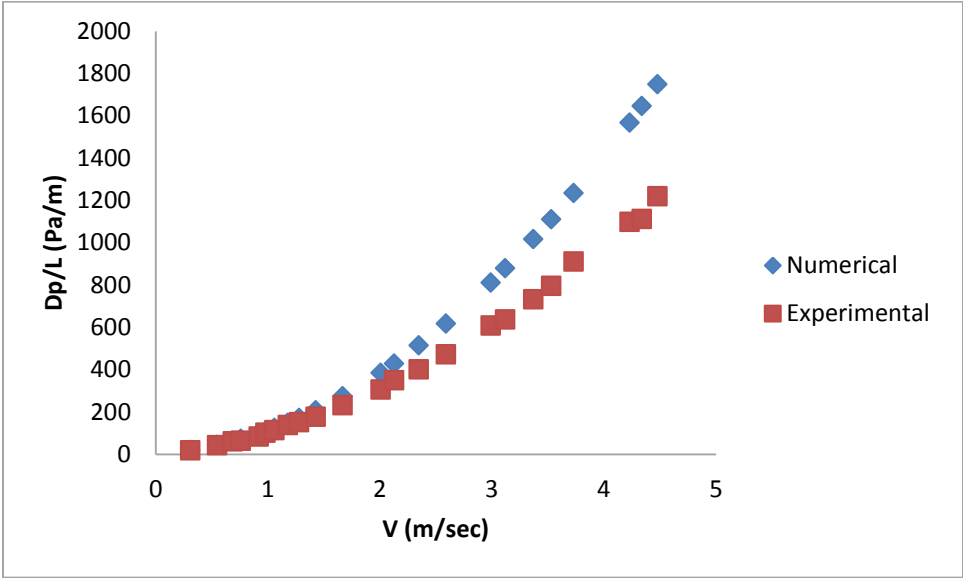


Figure 5. 15 Pressure Drop from Numerical and Experimental Studies of 10 PPI and 97% Porosity Foam

**Table 5. 4 Experimental Normalized Pressure Drop with Numerical for Low and High Velocity
Regimes for 10 PPI and 97% Porosity Foam**

Inlet Velocity (m/sec)	Numerical Dp/L (Pa/m)	Experimental Dp/L (Pa/m)	Difference %
0.31	19.77	18.75	5.16
0.55	44.21	41.99	5.02
0.69	62.11	60.10	3.24
0.76	72.13	63.38	12.12
0.92	97.82	82.67	15.48
0.98	108.48	101.31	6.61
1.06	123.60	113.25	8.37
1.18	148.21	138.31	6.67
1.28	170.54	150.65	11.66
1.43	207.12	177.16	14.46
1.67	273.60	231.75	15.29
2.01	384.34	305.89	20.41
2.13	428.04	349.85	18.26
2.35	514.37	401.55	21.93
2.59	617.62	471.36	23.68
2.99	810.41	608.61	24.90
3.12	878.56	636.82	27.51
3.37	1017.15	732.47	27.98
3.53	1110.98	796.37	28.31
3.73	1233.87	911.05	26.16
4.23	1567.95	1098.66	29.92
4.34	1646.62	1112.18	32.45
4.48	1749.36	1218.71	30.33

From a practical stand point, two of the most important characteristics of the flow in a porous medium are the permeability and the form drag coefficient. These two can be easily calculated by fitting a second-order polynomial to the pressure drop curves according to Eq. (5.6), and knowing the density and viscosity of the air. The obtained values from the simulation and the experiment are shown and compared in Table 5.5, for the two velocity regimes. It is clear that the simulation results are acceptable and they compare very well with the experiment strictly in the low

velocity regime. However, the differences between the simulation and the experiment in the high-velocity regime are very pronounced. The reason for this severe disagreement can be the significant difference in the ligament average diameter of the geometrical model and actual foam (26% as mentioned above), and the considerable difference in the resulting surface area density, as listed in Table 5.1. Another limitation of the model, which is imposed by the geometry, is that closed faces result when the porosity is reduced below 94%.

Table 5. 5 Simulation and Experimental Values of Permeability and Form Drag Coefficient in the Low- and High-Velocity Regimes.

		Simulation	Experiment	%Difference
<i>Low-velocity regime</i>	Permeability, $K \times 10^7$ (m²)	5.08	4.54	11.8
	Form Drag Coefficient, C (m⁻¹)	56.01	59.93	6.5
<i>High-velocity regime</i>	Permeability, $K \times 10^7$ (m²)	6.05	2.84	113.4
	Form Drag Coefficient, C (m⁻¹)	66.67	38.33	73.9

5.8 Study of Hydrodynamic Entry Length

5.8.1 Geometrical Model

For study of hydrodynamic entry length inside open metal foam with 10 PPI and porosity of 97.3 %, a matrix of 25x1 unit cells was used to represent a computational domain. The computational domain has cross section $(5.08 \text{ mm})^2$ and length of 127 mm in the positive z- flow direction (the flow direction), as shown in Fig.5.16.

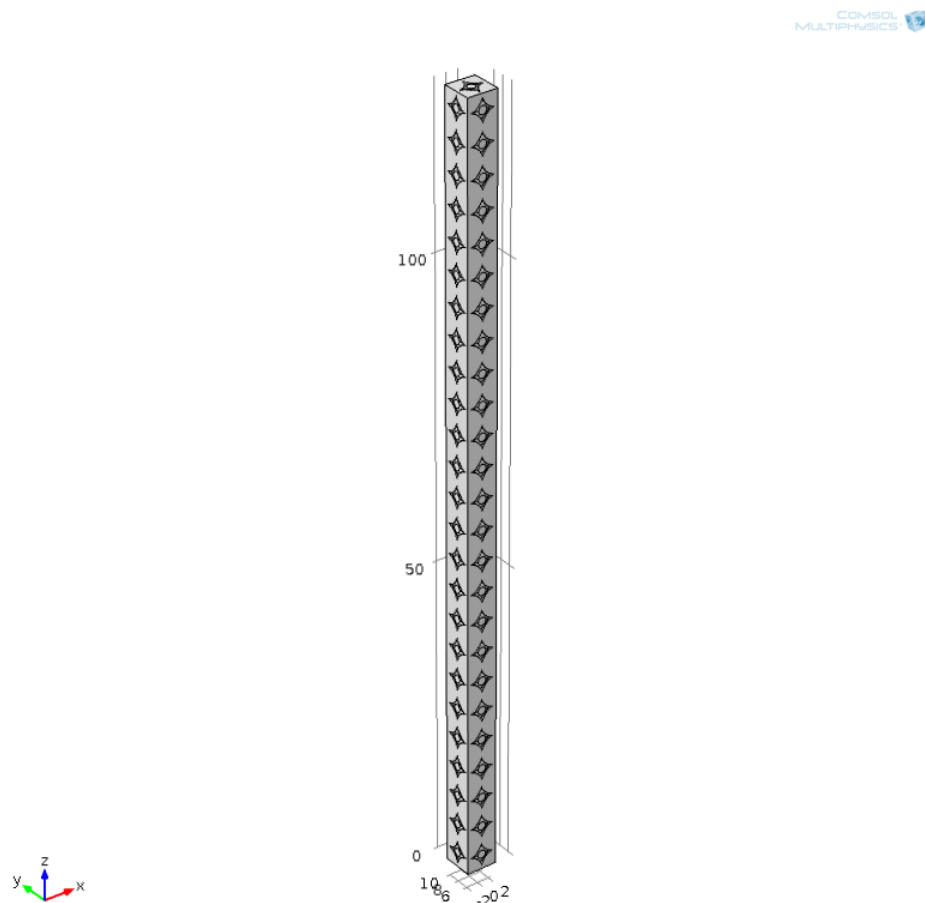


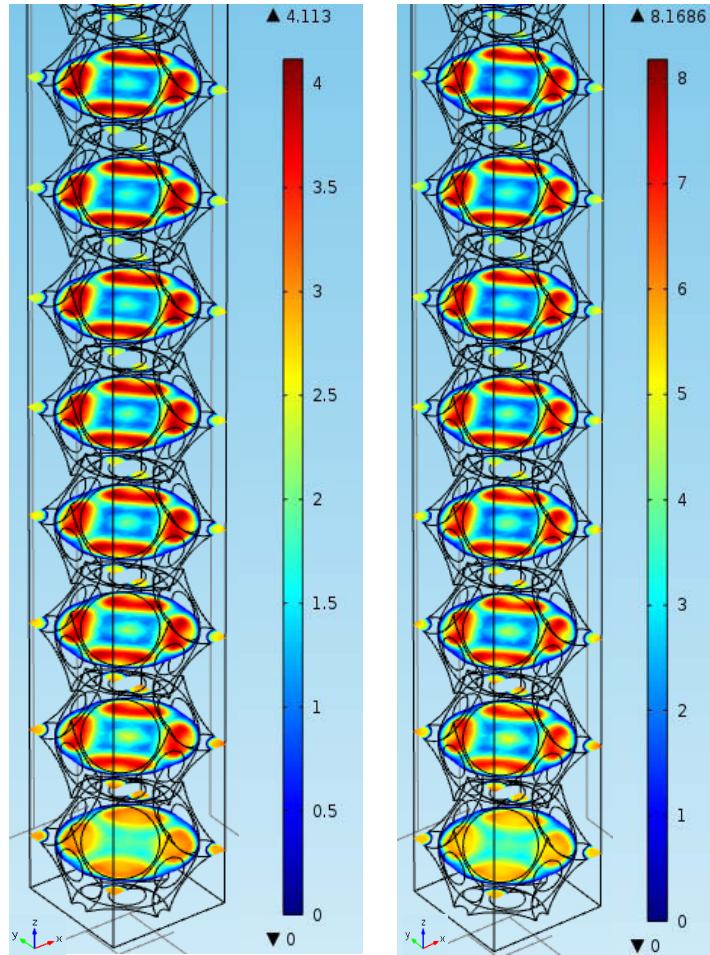
Figure 5. 16 The Computational Domain of Hydrodynamic Entry Length

5.8.2 Simulation Results

General description of the flow field inside the foam will be presented in light of the following three figures. Figure 5.17 shows cross-sectional slices perpendicular to the flow direction colored by velocity magnitudes at different locations along the flow direction (the positive z-direction), all taken in the developing region. Two cases are chosen to display the flow development: for inlet fluid velocities of 2.35 and 4.48 m/s. The solid ligaments' presence obstructs the flow, reduces the open cross-sectional area and increases the fluid velocity in the remaining open areas (dark red regions). These correspond to the pores (or open windows) of the foam. For inlet velocities of 2.35 and 4.48 m/s, the maximum velocity inside the foam is about 4.11 and 8.17 m/s, respectively. On the other hand, there are regions of very low velocity (light blue) and stagnation regions (dark blue) where the velocity is essentially zero. These regions are close to the solid ligaments of the foam and reflect the no-slip condition imposed on the solid-fluid interface.

The development aspect of the flow can be traced in this figure by focusing on the middle region of each cross-sectional slice, and noticing the sometimes subtle pattern and color changes. These changes get weaker and tend to diminish as the distance from the inlet increases, suggesting fully-developed flow conditions. This issue will be looked at in more detail later.

Figure 5.18 is a plot of streamlines traced by fluid elements flowing inside the foam- each colored by the velocity magnitude along the flow. The tortuosity of the porous medium is shown figure. 5.18.



$V_{in} = 2.35 \text{ m/s}$

$V_{in} = 4.48 \text{ m/s}$

Figure 5. 17 Cross-Sectional Slices Colored by Velocity Magnitudes for Inlet Velocities of 2.35 and 4.48 m/s.

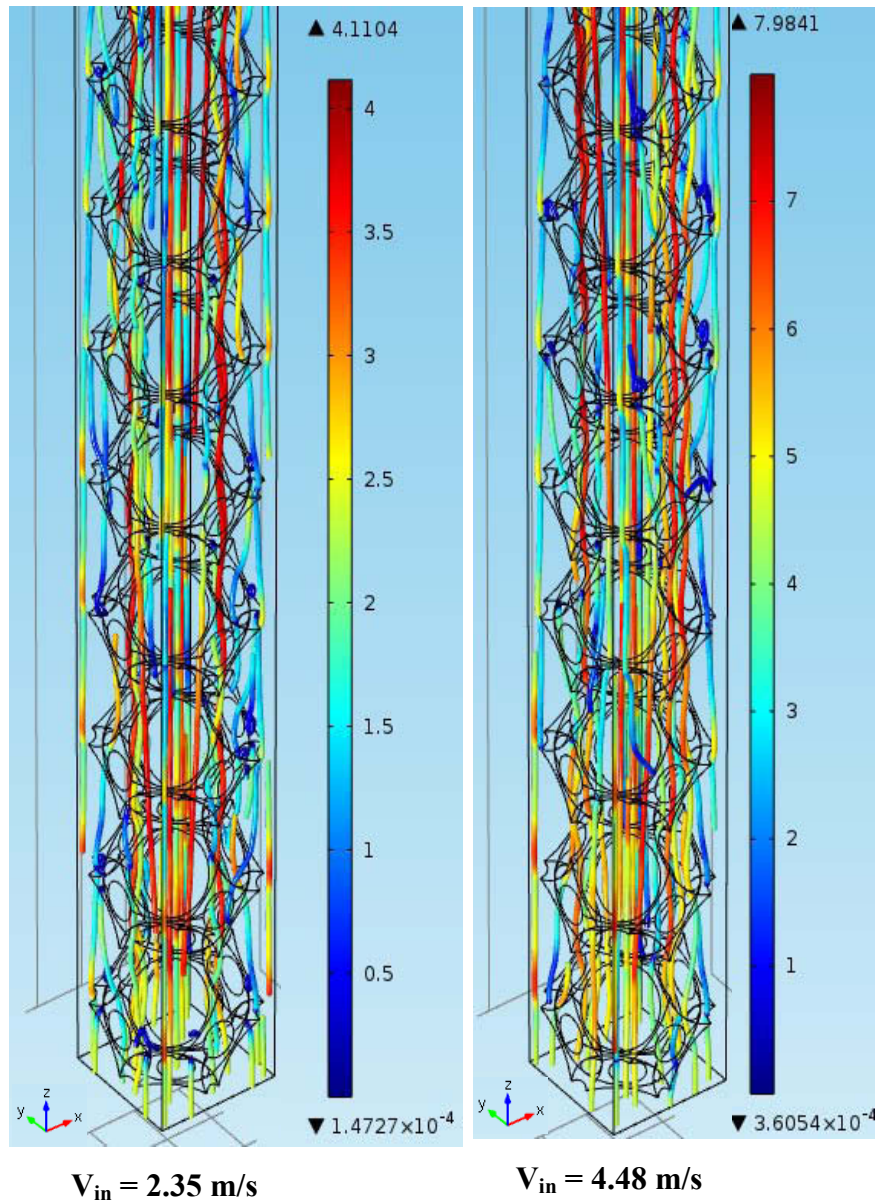


Figure 5. 18 Streamlines Colored by Velocity Magnitudes for Inlet Velocities of 2.35 and 4.48 m/s.

By the winding flow streamlines around the foam ligaments, which leads to mixing. By inspecting the changing colors along a given steam line, one also can notice locations of acceleration and deceleration influenced by the presence and location of solid foam ligaments. Stagnation regions are identified by the dark blue color. These interactions seem to temper down as the distance from the entrance

increases (see the outermost streamlines on the right and left of the domain for example.) There are areas in the domain that permit undisturbed (aligned) flow paths through the pores or the windows of the foam cells. This is especially true around the central area of the cells. A similar observation was made by Kopanidis et al. (2010).

Figure 5.19 is a plot that shows the velocity vectors in an x-z plane passing through the center of the simulation domain. At every location, the magnitude of the velocity is signified by the size and the color of the arrows. This figure provides another way of visualizing the accelerated and decelerated flow regions within the cells. The plot also shows the orientation of the velocity vectors at various locations, and how some of these vectors converge as they approach the open pores in their path- another sign of flow mixing. The changes in the size and color of the arrows soften as the distance from the inlet increases, again suggesting an approach from a developing to developed flow regions.

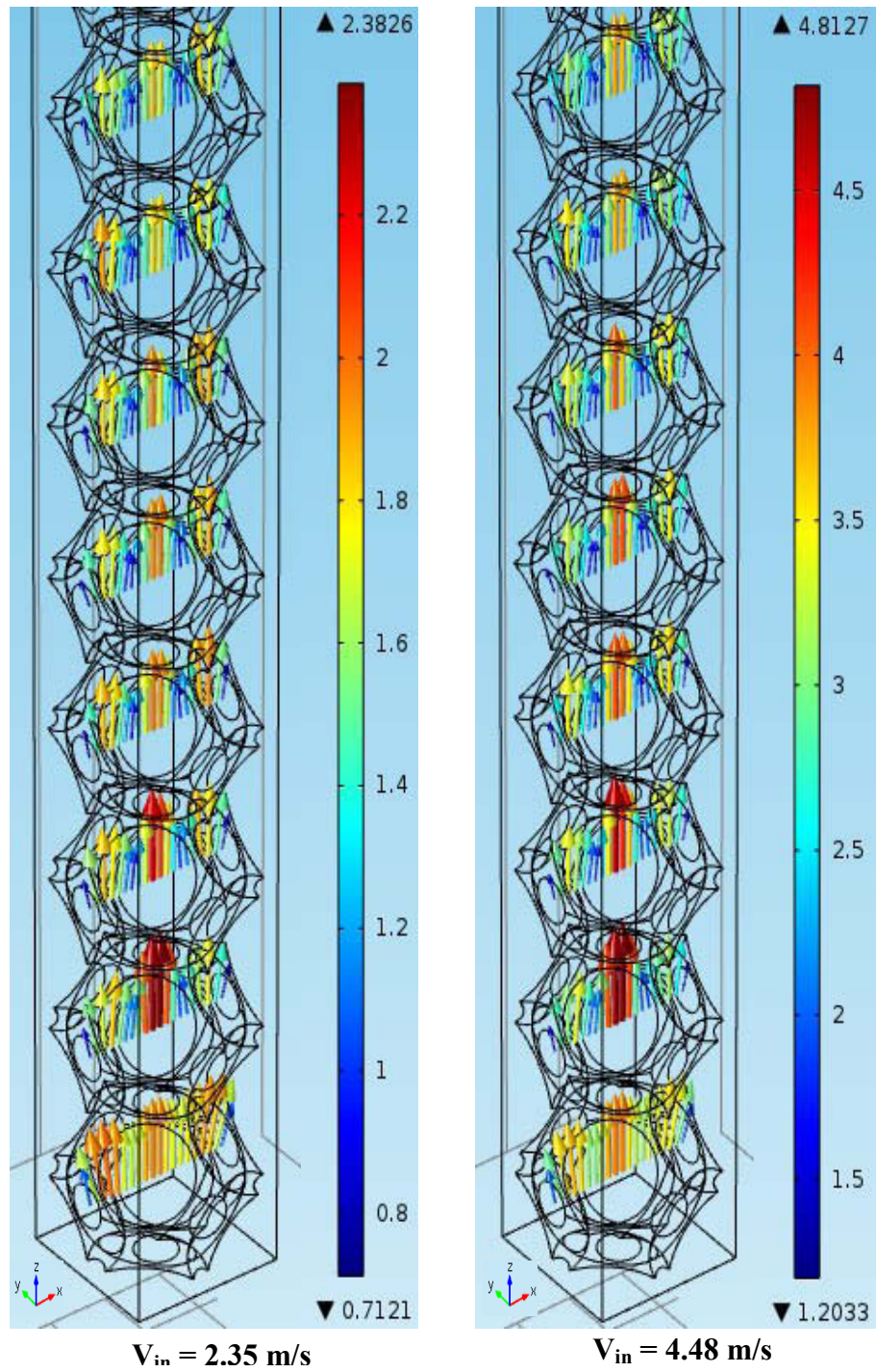


Figure 5. 19 Velocity Vector at an x-z Plane Passing through the Middle of the Domain for Inlet Velocities of 2.35 and 4.48 m/s.

Flow development in the entrance region will be investigated with the aid of the following three figures. Figure 5.20 is a two-dimensional plot that shows the velocity vectors at an x-z plane passing through the center of the cells for all five values of inlet velocities. It is clear in this figure, that the velocity in the flow direction is changing as the distance from the entrance increased in the flow direction. Also, for the low inlet velocity of 0.31 m/s, the change is completed after the second cell, after which there is no significant change in the velocity field. Similar trends are present for the other four inlet velocity values. However, significant changes in the velocity field seem to be completed further away from the entrance. This clearly shows that the development length depends on the inlet velocity (or the Reynolds number).

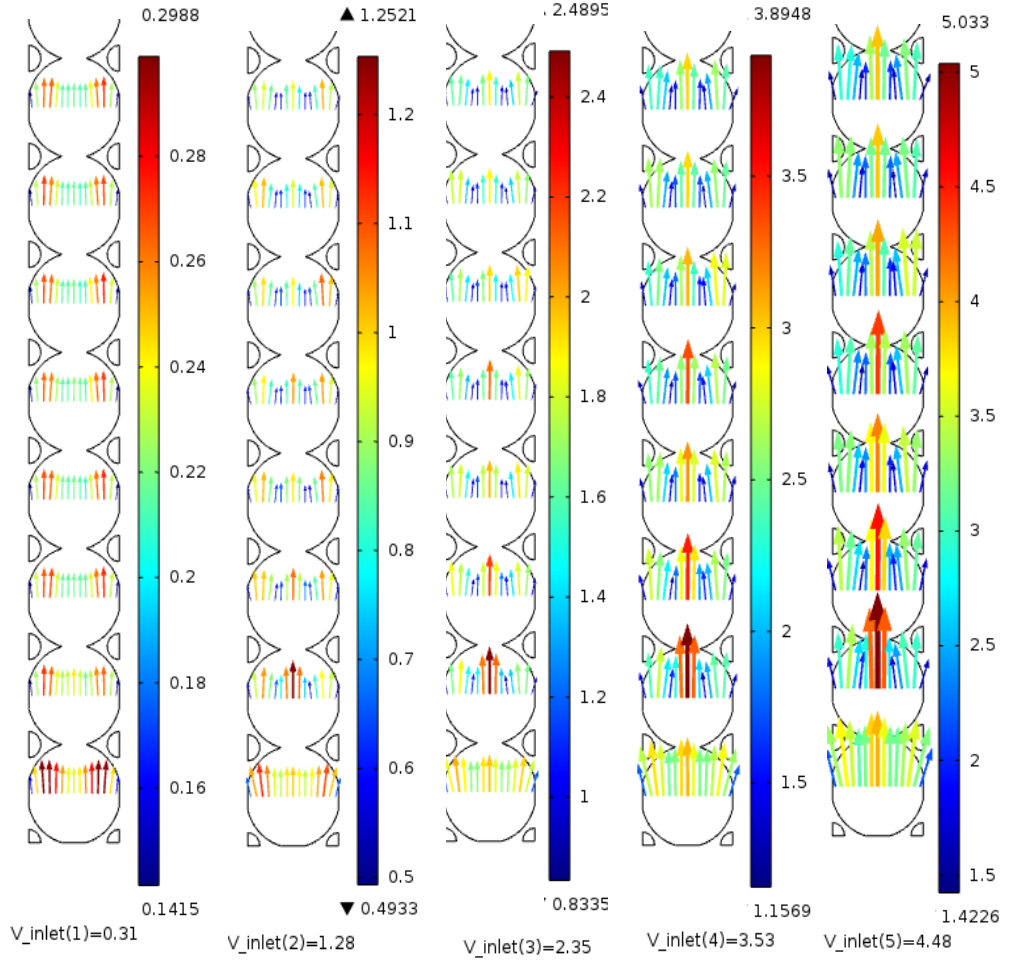


Figure 5.20 Two-Dimensional Plot Showing Velocity Vectors in an X-Z Plane Passing Through the Center of the Cells for All Five Values of Inlet Velocities

These flow-development trends can be viewed from a different angle. Figure 5.21 is a plot of the cell center z-velocity component as a function of cell number. This velocity is taken at 2.54 mm from the entrance of each cell. It is evident that this velocity starts high close to the entrance and asymptotically reaches relatively constant values as the distance from the entrance increases. Actually, the entrance length can be ascertained for different inlet velocities, as given in Table 2. The changes toward the end of the porous channel (in the last 6 cells) may be due to the

presence of an exit effect. Horneber et al. (2012) confirmed the presence of an exit effect for flow in metal foam.

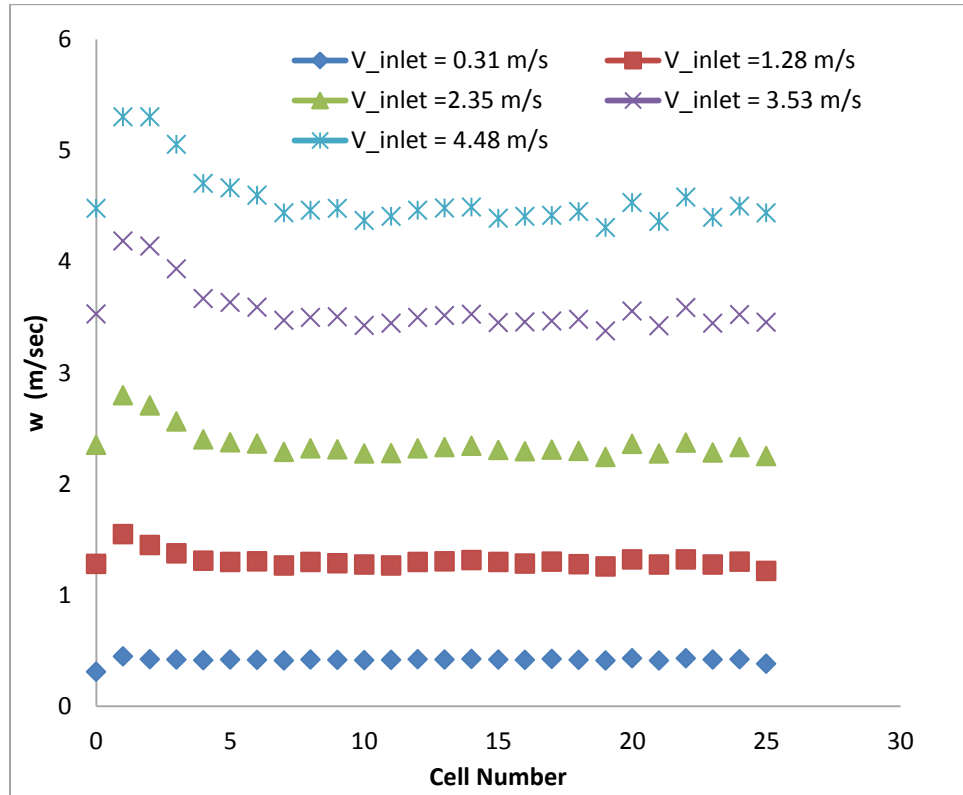


Figure 5.21 Cell Center z-Velocity Component at 2.54 mm from the Entrance of Each Cell as a Function of Cell Number

A meaningful criterion for asserting the start of the fully-developed region and the end of the entry region is that the pressure drop per unit length for a given cell no longer changes as the location of the cell from the inlet increases. Figure 5.22 is a plot of the pressure drop per unit length for each cell for all cells and all inlet velocities. The suggestions made by the previous plots (Fig.5.20 and Fig.5.21) regarding the entrance region are both displayed and conformed by Fig.5.22. It is now easy to estimate the entrance length by locating the cell beyond which the pressure drop per

unit length becomes essentially constant. The entrance length given in cells from is obtained, and is given in Table 5.6 for each inlet velocity. The entry length is seen to increase with the inlet velocity, and seems to approach a constant value as the inlet velocity increases: it is six cells for both 3.35 and 4.48 m/s inlet velocities.

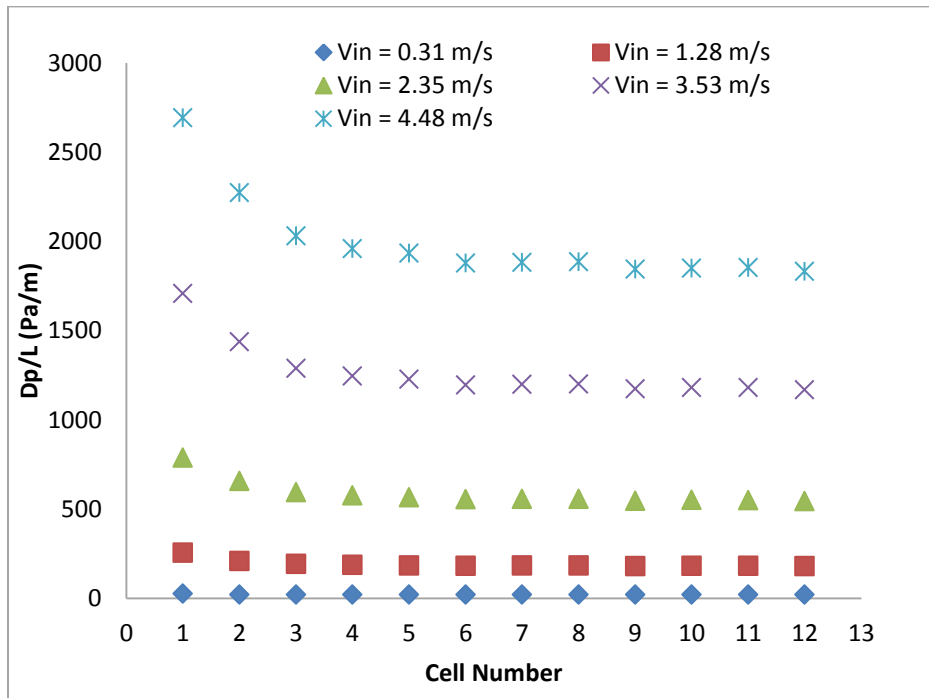


Figure 5. 22 Pressure Drop over the Length of Each Cell

Table 5. 6 Entrance Length for Various Inlet Velocities

Inlet Velocity m/s	Reynolds Number Re	Entry Length (Cells)	Entry Length (mm)
0.31	97	1	5.08
1.28	401	3	15.24
2.35	737	5	25.4
3.53	1107	6	30.48
4.48	1405	6	30.48

Poulikakos and Renken (1987) stated that the hydrodynamic entry length is of order KV/ν where K is the permeability, V the average velocity and ν the kinematic viscosity; and that this ratio is negligible in most practical cases. Kaviany (1985) indicated the entry length was negligibly small. The permeability of the simulated foam was calculated from curve-fitting the pressure drop per unit length as a function of the Darcy velocity according to Forchheimer equation, as is shown below. The permeability was obtained as $5.14 \times 10^{-7} \text{ m}^2$. Therefore, according to Poulikakos and Renken (1987), the entrance length is of the order 152 mm for the highest velocity. Using a cell size of 5.08 mm, the entrance length is about 30 cells. The source of Poulikakos and Renken (1987) had been Vafai and Tien (1981). The latter researches actually indicated that the ratio KV/ν can become significant for flow of low dynamic-viscosity fluid in a highly permeable medium, which is exactly the case for air flow in open-cell metal foam. Nonetheless, the predicted entry length is much higher than the result obtained by the current study.

Nield et al. stated that the hydrodynamic entry length in porous media is of the order K/ε where K is the permeability and ε is the porosity; and that this ratio is typically small compared to the length or width of a porous medium (Nield et al. 2004)[15]. So for the foam in hand, the entry length should be of the order $5.3 \times 10^{-7} \text{ m}$. Clearly these predictions of entry length (for traditional porous media) are not consistent with the result of the current study for metal foam.

A couple of recent studies alluded to the entrance region for flow in metal foam. Kopanidis et al. (2010) covered the entrance region in their simulations for a domain

of only 10 metal-foam-cells long. They simulated 97% porous 10- and 40-ppi foam using Kelvin cell. Their fixed inlet velocity boundary condition represented the developing flow condition. They confirmed the significance of the developing region but did not give a value of the entrance length. Horneber et al. (2012)[33] confirmed the presence of an entry region for flow in metal foam. They used Kelvin cell, porosity was 89% and window diameter of 3.09 mm, which is closes to 10-ppi commercial foam with a pore diameter of 2.54 mm. For an inlet velocity of 1.65 m/s, and judging by the behavior of the maximum values of the velocity at the center of their simulated domain, an entrance length of 2 to 3 cells was observed. This length corresponded to 30 to 40% of the total length of the medium (eight cells in the flow direction). This compares well with an entrance length of three cells for the case of 1.28 m/s inlet velocity of the current study.

5.8.3 Entry-Length Experiment Verification

The experiment was conducted in an open loop system as it was described in Section 5.7.1. The foam sample used in this experiment was manufactured by ERG Materials and Aerospace Corporation [38]. The foam was made of aluminum alloy 6101-T6, having a cross section area of $(10.16 \text{ cm})^2$. The sample tested for this experiment is listed in Table 5.1. A photograph of the 10 PPI and porosity of 90.2 % metal foam sample that is tested is shown in Fig.5.3.

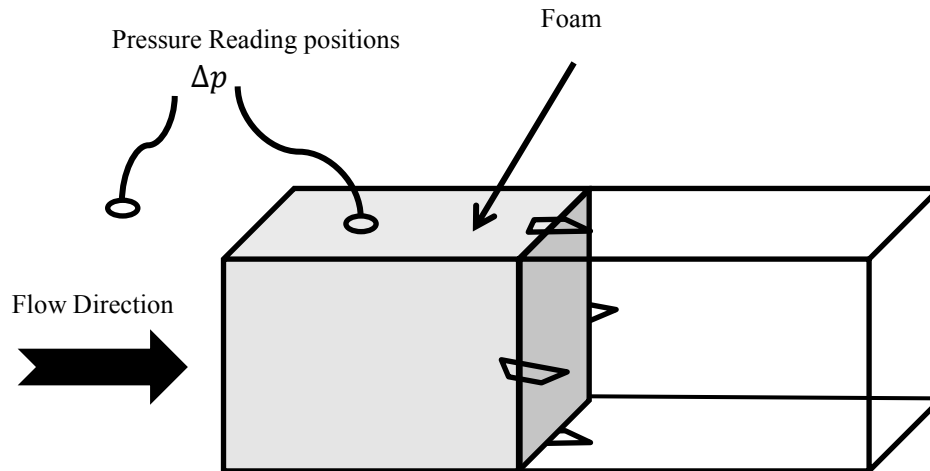


Figure 5. 23 Schematic of the Test Sectin.

The test section for studying hydrodynamic entry length was a cross sectional area of $(10.16 \text{ cm})^2$. As shown in Fig.5.23, foam sample could be placed inside the tunnel from one side at the end of the tunnel.

A schematic of the setup for entrance effect is shown in Fig.5.24. A tunnel was fabricated with the use of Plexiglas, which had cross sectional area of $(10.16 \text{ cm})^2$ and a length of 10.16 cm. To measure the pressure, taps with a diameter of 0.75 cm were drilled at the center of the top of the foam sample. To visualize the entrance effect,

more holes were drilled at 0.5 inch increments, starting 0.625 inch from the channel inlet and going all the way up to 2.5 inches.

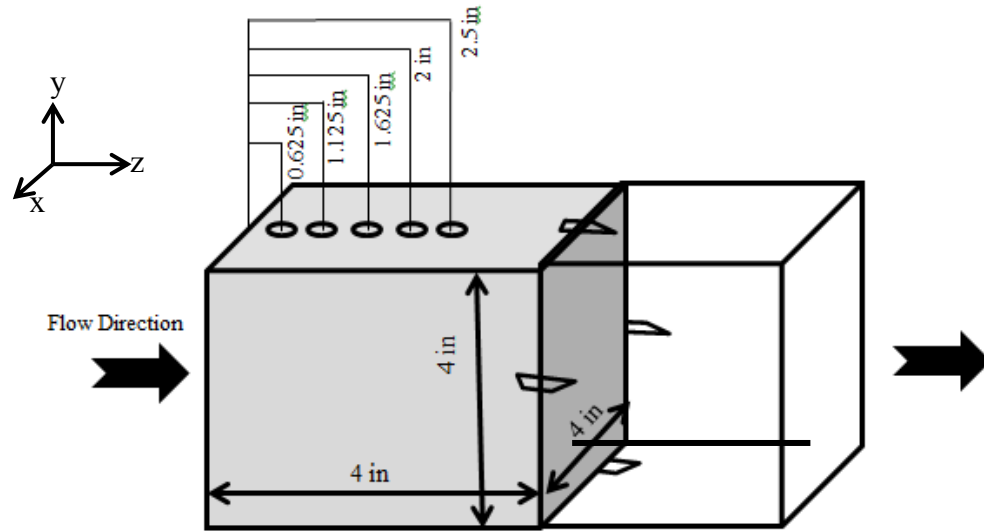


Figure 5. 24 Schematic of Entrance Effects Measurement.

The pressure was read using the taps that were drilled on the top of the foam. When the desired velocity was achieved, the pressure drop was recorded. This measurement was taken when both velocity reading and the pressure drop were stabilized. For each velocity, the pressure drop measurement was repeated two to three times and the average pressure drop for those readings was recorded.

Figure 5.25 shows experimental and numerical pressure drop per unit length at different distance from the inlet. The results show that experimental pressure drop is quite greater than numerical pressure drop at low velocities. Therefore, the flow in experiment takes a longer distance to be fully developed than the flow in numerical model. The reasons for these differences can be explained as follow. The inertial term in Eq.5.3 was neglected and flow was considered to be Stokes flow. As velocity

increases, the numerical pressure drop increases, that is, the inertial term has important influence. It cannot be neglected.

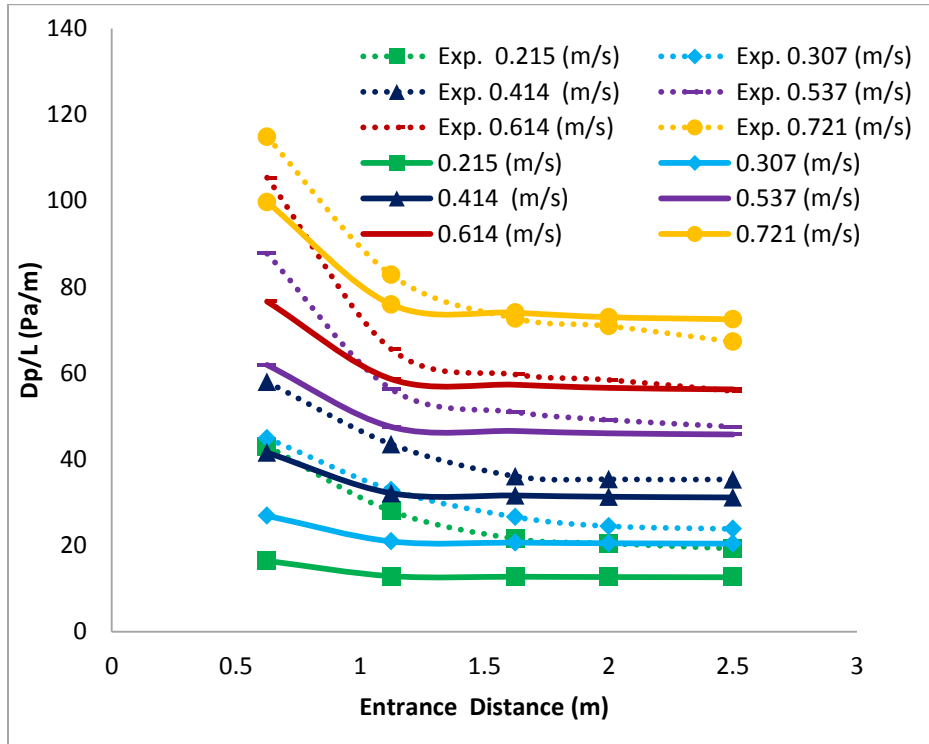


Figure 5. 25 Pressure Drop per Unit Length across the Porous Channel

Chapter 6: Numerical Convection Heat Transfer in Metal Foam Using COMSOL

6.1 Introduction

Metallic foams are widely used in thermal management industry, such as compact heat sinks of power electronics and compact heat exchangers, due to high thermal conductivity, large accessible surface area per unit volume and high porosities (often greater than 90%). Metal foams have also been used as thermal conductivity enhancers in phase-change materials [40,41]

For most recent development in the field of metal foam, Ref. [42] should be consulted. The high porosity means very low weight. All of these attributes make metal foam a very attractive heat transfer core for many applications and need to be taken into account in many CFD (Computational Fluid Dynamic) calculations. The understanding of fluid flow and convection heat transfer through open-cell metal foam is crucial for heat-exchange systems employing metal foam.

Experimental flow and/or heat transfer characteristics studies on metal foam have been reported in the literature [5,8,10,11,19,40–43]. Analytical solutions of the volume-averaged transport equations in porous media, e.g., metal foam, are also available for some simple or simplified cases, e.g., [12,13]. The internal structure of metal foam results in complex flow fields, including flow recirculation and unsteadiness at the back of the foam's solid fibers. Intricate details of the interactions between the surface of the solid matrix of the foam and the fluid are not completely

understood, and some of them can be masked by empirical correlations and volume averaging. Hence, detailed numerical analyses at the microscopic pore level have been conducted to investigate thermal and flow characteristics of open-cell foam. A few will be summarized below.

Due to these difficulties; complex and intrinsically random architecture of metal foam are virtually impossible to capture exactly and cannot be included in the CFD domain. Many these difficulties will be alleviated if an internal structure geometrical modeling of metal foams were available. To model a whole foam domain would require a lot of time of a computational power. This issue can be overcome by investigating a cell representing the structure of open-cell metal foam. This geometrical idealization of the internal structure the foam must be able to capture the foams' morphological parameters, namely; shape and diameter of cell; shape and thickness of ligaments; specific surface area and porosity.

In this chapter, a cell geometry, which was proposed previously in Chapter 3, will be used to numerically study forced convection heat transfer between aluminum foam and air. This particular geometry is relatively simple and easier in terms of meshing compared to others used in other studies [7,22,27]. The Navier-Stokes and the energy equations are directly solved and the velocity and temperature fields are obtained using COMSOL. Proper boundary conditions are applied. A clear validation strategy using accepted analytical solutions for the volume-averaged transport equations will be given in the next chapter. The details of the modeling process are given in this chapter.

6.2 Problem Description

The problem considered is shown schematically in Fig.6.1. A channel is filled with open-cell porous medium (or metal foam). The channel has height $2H$ and is bounded by solid surfaces at the top and bottom.

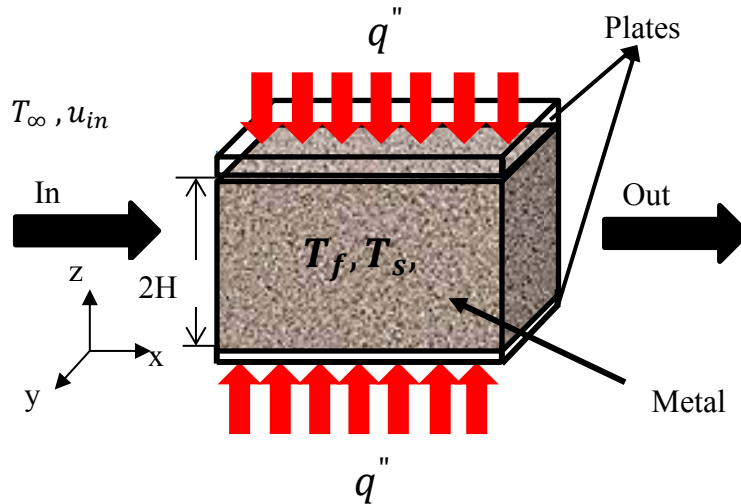


Figure 6.1 Problem Schematic

The two surfaces are heated with a constant uniform heat flux q'' . Inside the porous medium, there is a one-dimensional fluid flow in the positive x -direction with velocity u . The following boundary conditions were applied for fluid flow analysis:

- Constant fluid velocity at the inlet of the porous channel.
- Constant fluid pressure at the outlet of the porous channel (0 bar).
- Zero fluid velocity (no-slip) on the foam internal surface.
- Symmetry in the center of the porous channel.

The mass and momentum conservation equations are as following:

$$\rho \nabla \cdot u = 0 \quad (6.1)$$

$$\rho(u \cdot \nabla)u = \nabla \left[-pI + \mu(\nabla u + (\nabla u)^T) - \frac{2}{3}\mu(\nabla \cdot u)I \right] + F \quad (6.2)$$

where p is the fluid pressure, μ is the fluid viscosity, ρ is the fluid density and F represents body forces. For the heat transfer problem, following assumptions are made:

- Radiation and natural convection are negligible.
- Thermophysical properties of the solid and the fluid phases are constant.
- The porous medium is isotropic and homogeneous.

The equation energy model for the fluid and solid phases are given by

$$\nabla \cdot (k_f \nabla T_f) + Q_f = \rho c u \nabla T_f \quad (6.3)$$

$$\nabla \cdot (k_s \nabla T_s) + Q_s = 0 \quad (6.4)$$

where the subscripts f and s refer to the fluid and solid phases, respectively. k is the thermal conductivity, T is the temperature, ρ is the density, c is the specific heat of the fluid, and u is the velocity inside the pores. Q represents heat per unit volume due to any heat sources (zero for the current case). It should be noted that COMSOL Solver ensures that both the temperature and the heat flux are continuous at the solid-fluid interface. The following thermal boundary conditions apply:

$$\text{At } z = 0 \quad \frac{\partial T_f}{\partial z} = \frac{\partial T_s}{\partial z} = 0 \quad (6.5)$$

$$\text{At } z = H \quad -k_f \frac{\partial T_f}{\partial z} = -k_s \frac{\partial T_s}{\partial z} = \dot{q} \quad (6.6)$$

$$\text{At } x = 0 \quad T_f = T_\infty \quad (6.7)$$

It should be noted that COMSOL solved the conjugate heat transfer problem considering both the solid and fluid phases. At the interface of the solid and the fluid inside the foam, continuity of temperature and heat flux was imposed.

6.3 Numerical Simulations

The physics of conjugate heat transfer is common in many engineering applications, including heat exchangers, HVAC and electronic component design. The purpose of this section is to provide guidelines and recommendations for setting up and solving a conjugate heat transfer problem using COMSOL.

6.3.1 Geometrical & Fluid domains

The first step in simulating the flow and heat transfer in the foam is to determine a geometrical model that can represent the actual internal structure of the foam. Consider a cell made by spheres of equal volumes located at the vertices of a cube and at the center of it. The ideal foam geometry is obtained by subtracting the spheres located at the body center and vertices of the cube from the cube itself as shown in Fig.3.5.

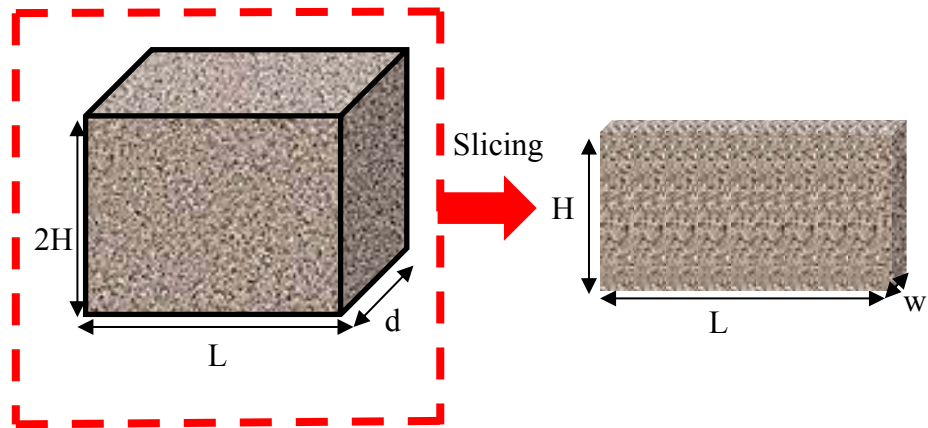


Figure 6.2 Taking Thin Slice From the Actual Physical Domain

Solving the Navier-Stokes equations with the two-equation model for the heat transfer at the pore level is impractical in CFD due to computing resource limitations. To keep the computational domain reasonable within those limitations, using symmetry perpendicular to flow direction only rectangle slice with length (L), height (H), and width (w) was taken at the middle plane of an actual domain with length L , height $2H$, and width d as seen in Fig.6.2 . Then, each slice is evenly split into blocks as shown in Fig.6.3.

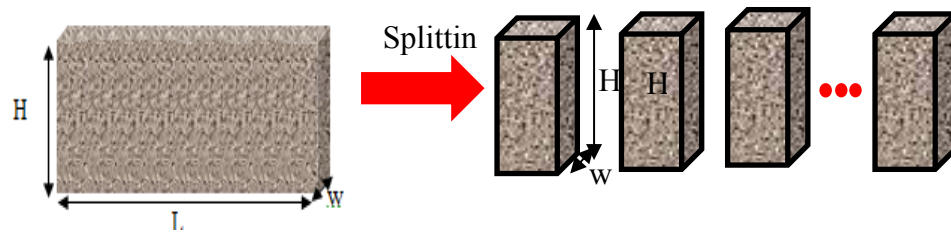


Figure 6.3 Splitting the Thin-Slice Domain into Even Blocks

Each block consists of many periodic unit cells. Figure 6.4 shows one block with its periodic cells at pore level scale.

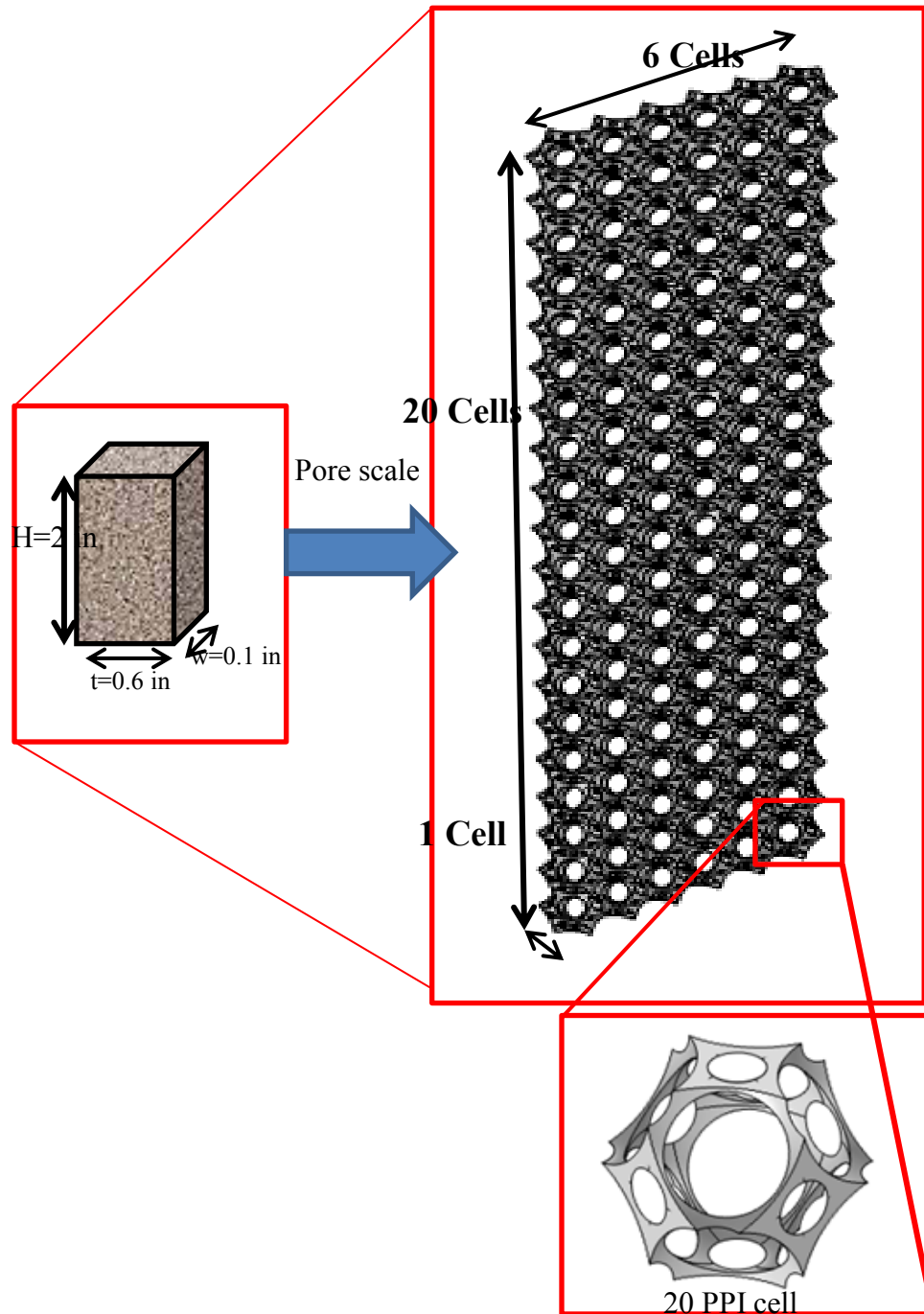


Figure 6.4 3D Metal Foam Geometrical Approximation at Pore Level

Figure 6.5 shows fluid and metal domain modeling creations, a matrix of 30 BCC unit cells having 94.7% porosity and 20 PPI was placed inside a rectangular channel. This matrix was subtracted from a rectangle that contained it, in order to get the fluid

(air) domain as shown in Fig.6.5 c. Air was used as the working fluid with density of 1.2 kg/m^3 and a viscosity of $1.814 \times 10^{-5} \text{ Pa.s}$.

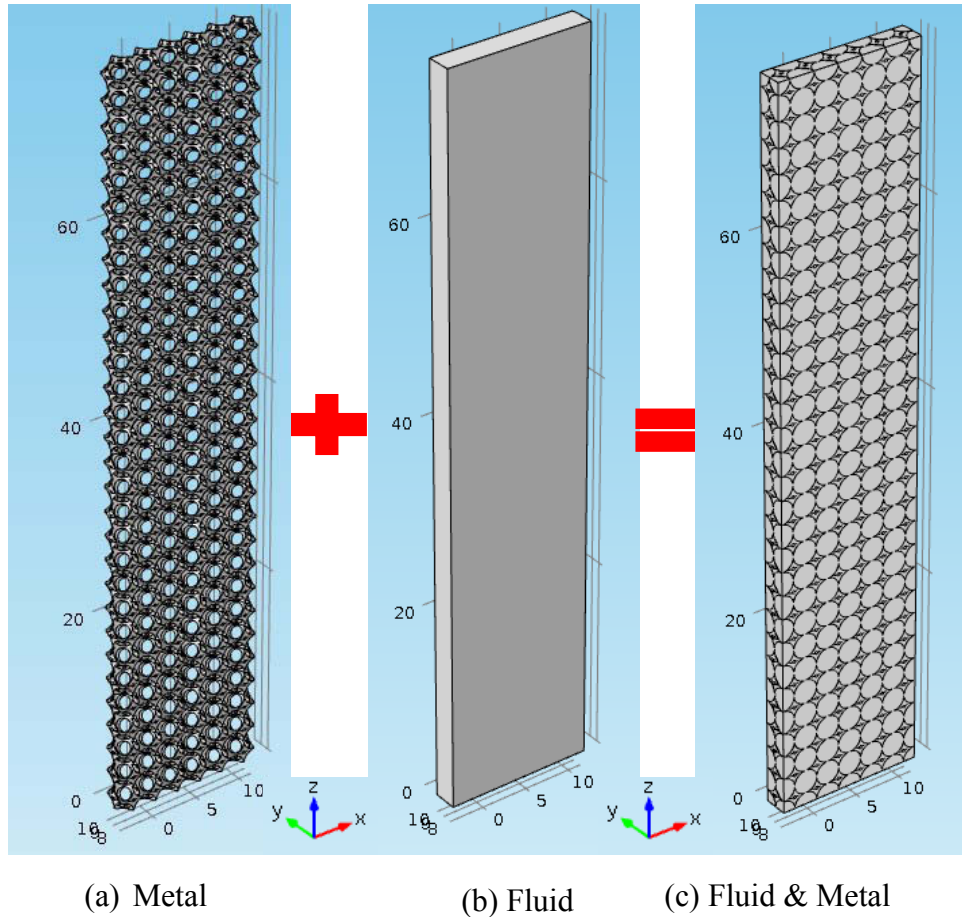


Figure 6.5 Creation of One Block Model

6.3.2 Model Description

The model solves thermal balance equations for the aluminum foam mounted inside a channel of rectangular cross section as seen in Figure 6.6, and the air flowing in the rectangular channel. Air enters the channel at the inlet (at $x=0$) and exits the channel at the outlet (at $x=0.6$ inch). Thermal energy is transported through conduction in the aluminum foam and through conduction and convection in the cooling air. The temperature field is continuous across the internal surfaces between the aluminum foam and the air in the channel. The temperature is set at the inlet of the channel. The base of the aluminum foam receives q'' heat flux through a thin plate. The transport of thermal energy at the outlet is dominated by convection.

The flow field is obtained by solving one momentum balance equation for each space coordinate (x , y , and z) and the mass balance equation. The inlet velocity is defined by a constant velocity for laminar flow. At the outlet, a constant pressure is combined with the assumption that there are no viscous stresses in the direction perpendicular to the outlet. At all solid surfaces, the velocity is set to zero in all three spatial directions. The thermal conductivity of air, the heat capacity of air, and the air density are all taken as temperature-dependent material properties.

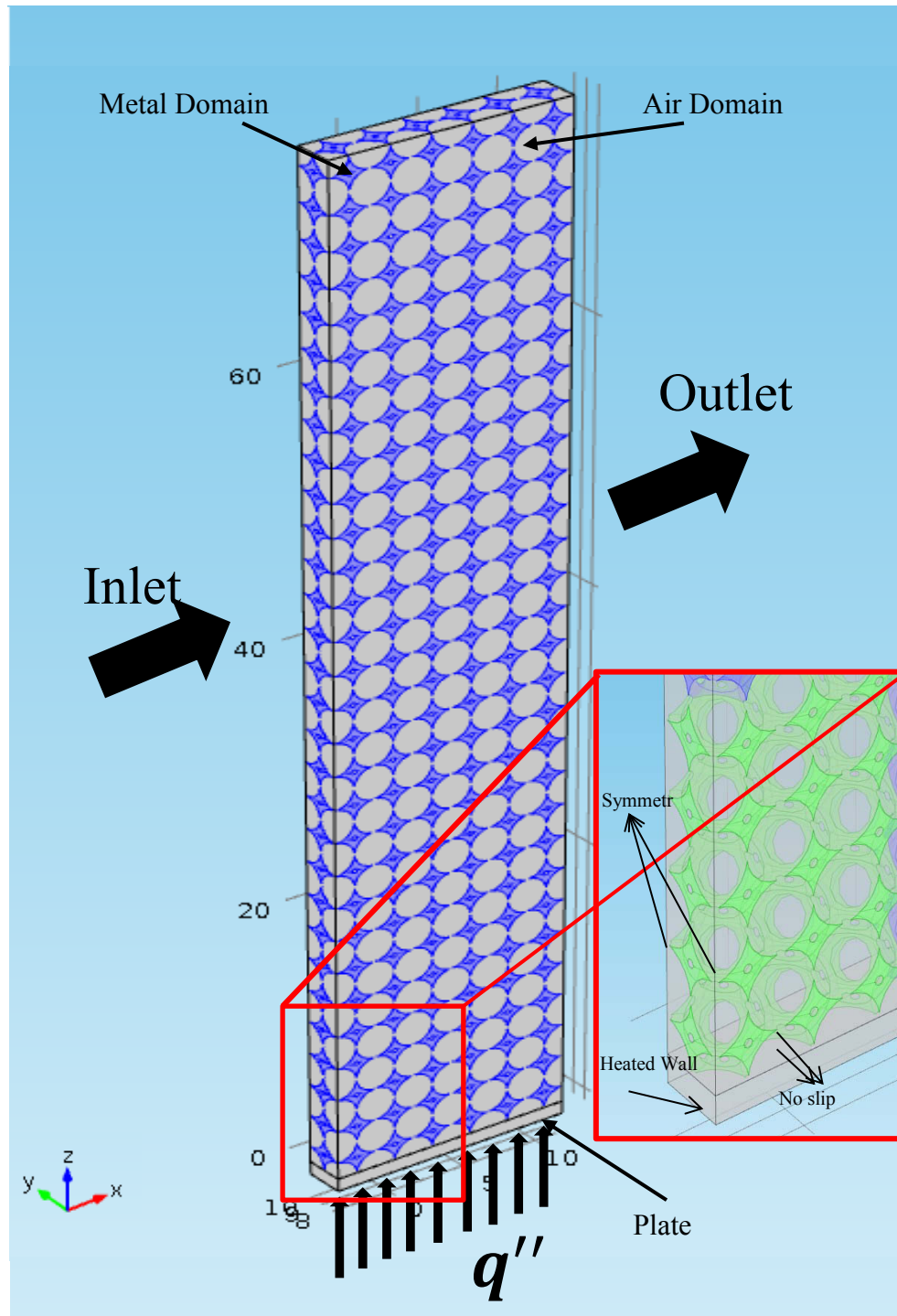


Figure 6.6 The Block Model Set-Up Including Channel and Metal Foam

6.3.3 Solving with The Marching Technique

In this section, a new solving technique called the marching technique used in COMSOL is implemented. The marching technique is used to solve an entire domain with length L as seen in Fig.6.3 by splitting it evenly to many blocks. Each block will represent a domain with a length that is smaller than L . The block domain is a practical domain, which can be solved in COMSOL with less memory computing resource. In general, the velocity and temperature fields obtained at outlet of the first block are applied to next block (the same block geometry as first one) at its middle, and then repeat the steps between the third block and second block, and so on. The exact details of the steps are:

1. Run the first block as seen in Figure 6.7. At the inlet, a constant flat profile velocity V_i , 0.2 m/sec, is applied, and the temperature T_i is set 295.15 K. At the outlet, a zero pressure P_0 is implemented with no viscous stresses normal to the outlet. At all foam surfaces and upper surface of the thin plate surface, the velocity is set to zero in all three spatial directions. The heat flux q'' , 4895 W/m² is applied to the base of the thin plate. Other boundaries are set as symmetry. The exit velocity V_0 , and temperature T_0 , and inlet pressure P_i are obtained by solving one momentum balance and energy balance for each space coordinate (x , y , and z) and a mass balance.

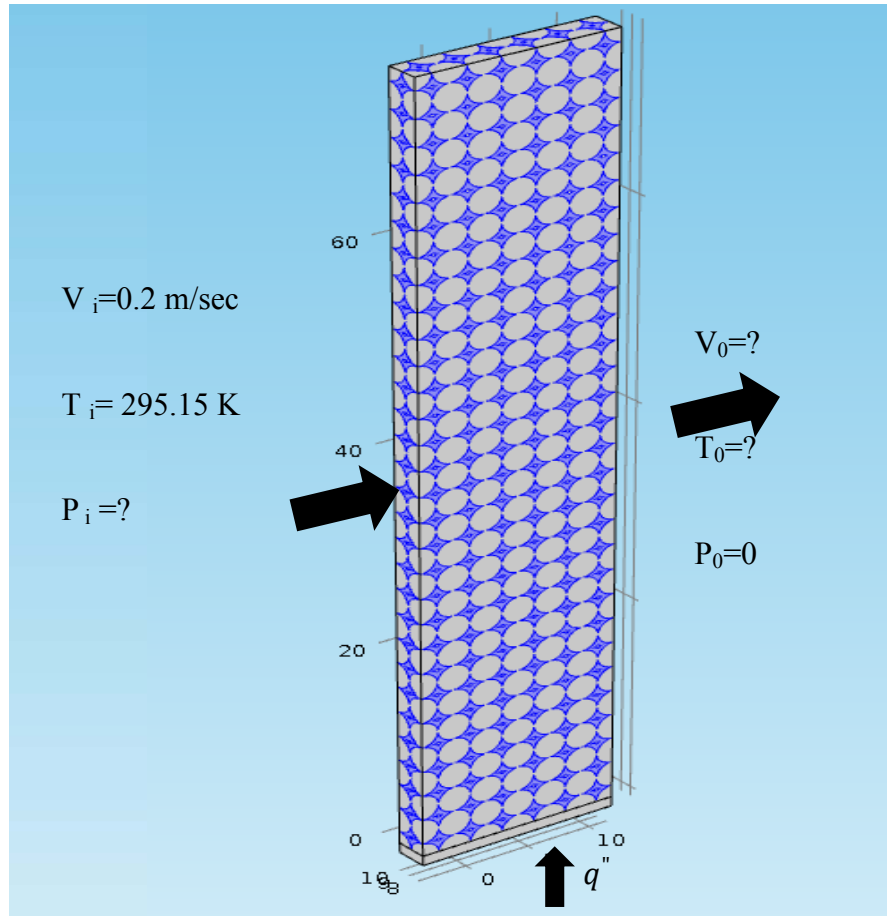


Figure 6.7 Setting Up a Unit block Before Marching Technique

2- Now, $\Delta P = P_i$ is obtained over the first block. Finding the total pressure over the entire domain by multiplying ΔP by a number of marching blocks $N_{marching}$. This assumption gives an approximation of pressure drop over the actual domain.

Each block has length t inch in flow direction. If the entire domain has length L inch, so the $N_{marching}$ is obtained by

$$N_{marching} = \frac{2L}{t} - 1 \quad (6.8)$$

3- Now start the marching as seen in Fig.6.8, with the first block seeing a back pressure that corresponds to having $N_{marching}$ other marching blocks in the flow direction. So instead of using outflow condition ($P_o=0$), use an exit pressure

$$P_2 = P_i \times N_{marching} \quad (6.9)$$

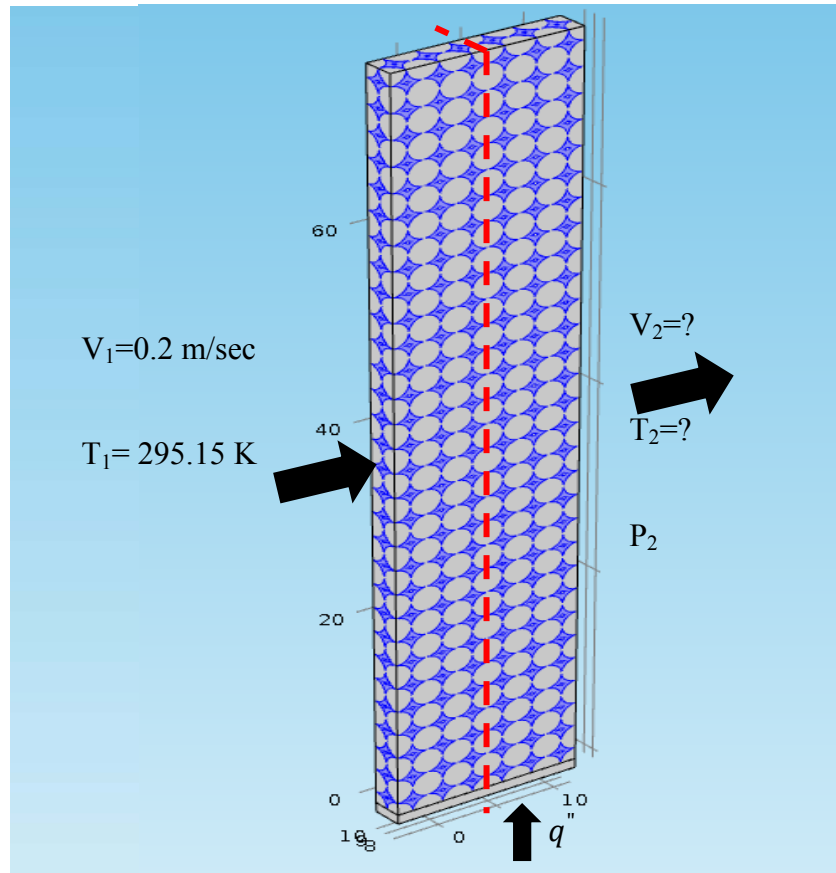


Figure 6.8 The First Marching Block Set-Up

4. The second block as seen in Fig.6.9 sees less back pressure that is,

$$P_3 = P_i N_{marching} - P_i \quad (6.10)$$

Then, the inlet velocity and temperature profiles can be evaluated using a built-in function in COMSOL called General Extrusion coupling operator. This operator

maps the velocity and temperature profiles defined on the middle of the first block (seen in Fig.6.8) as a source and to the velocity and temperature profiles on the inlet of the second block as destination. Mapping between a source and destination is valid if their geometrical maps are valid.

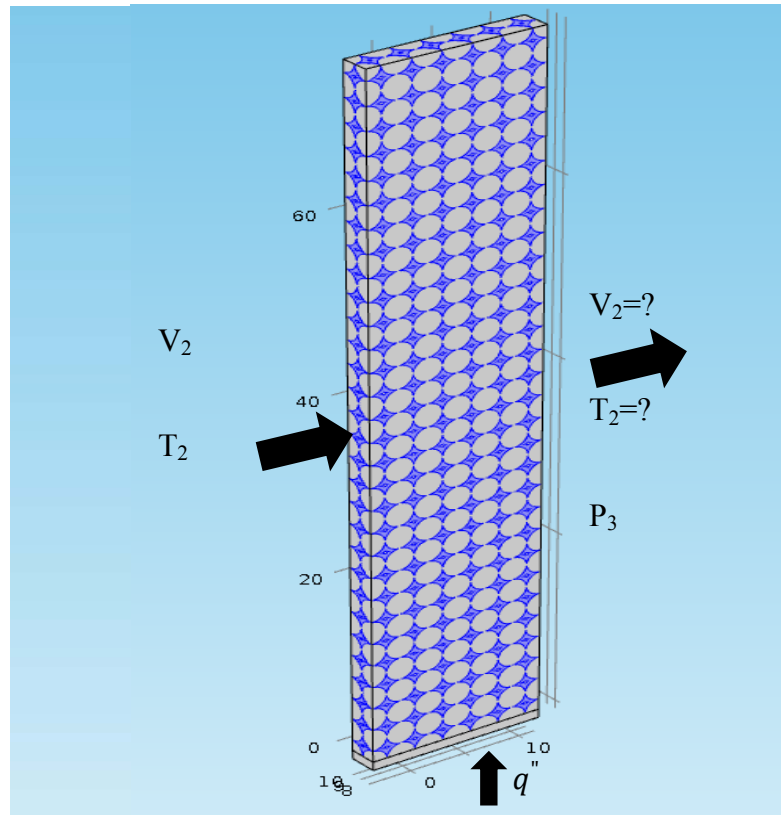


Figure 6.9 Second Marching Block Set-Up

5. The third block as shown in Fig.6.10 sees less back pressure, that is ,

$$P_3 = P_i N_{marching} - 2P_i \quad (6.11)$$

Like before, take the velocity and temperature profile from the middle of this block and put them at the next block's inlet as entrance conditions.

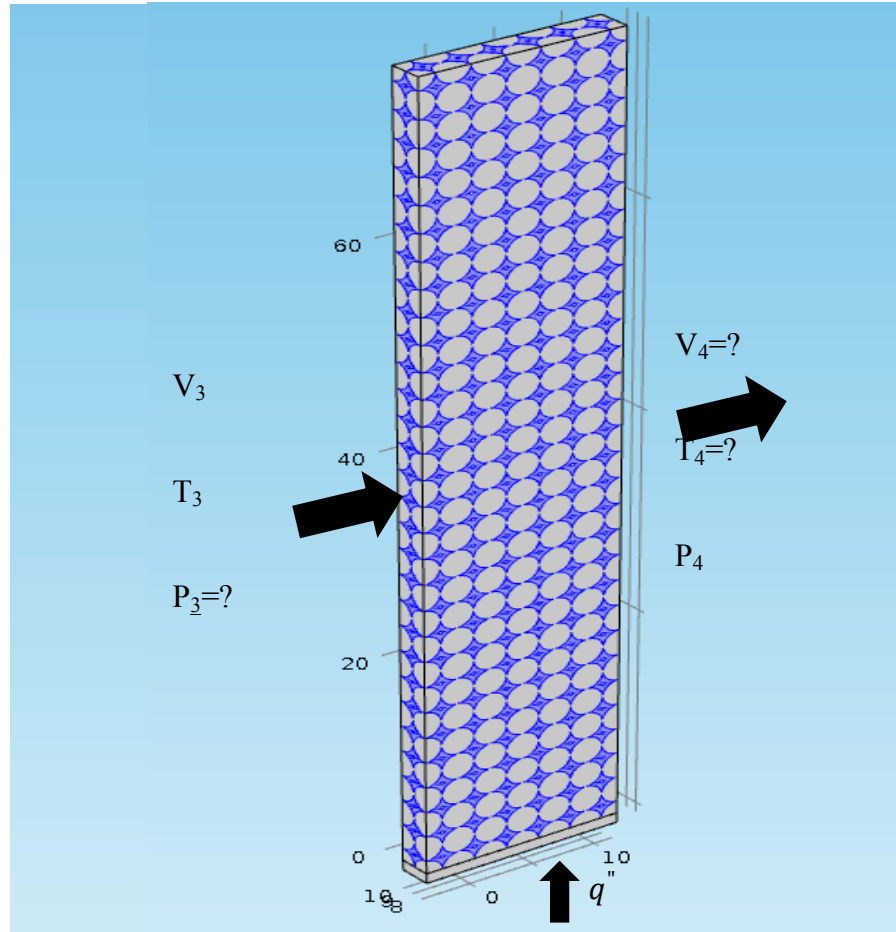


Figure 6.10 The Third Marching Block Set-Up

6. Go on with the same approach as mentioned in steps 3, 4, and 5. Fig.5.11 shows the last block seeing back pressure that is zero gauss pressure. The inlet velocity and temperature profiles are taken from the middle of the previous block numbered, $N_{\text{block}}-1$.

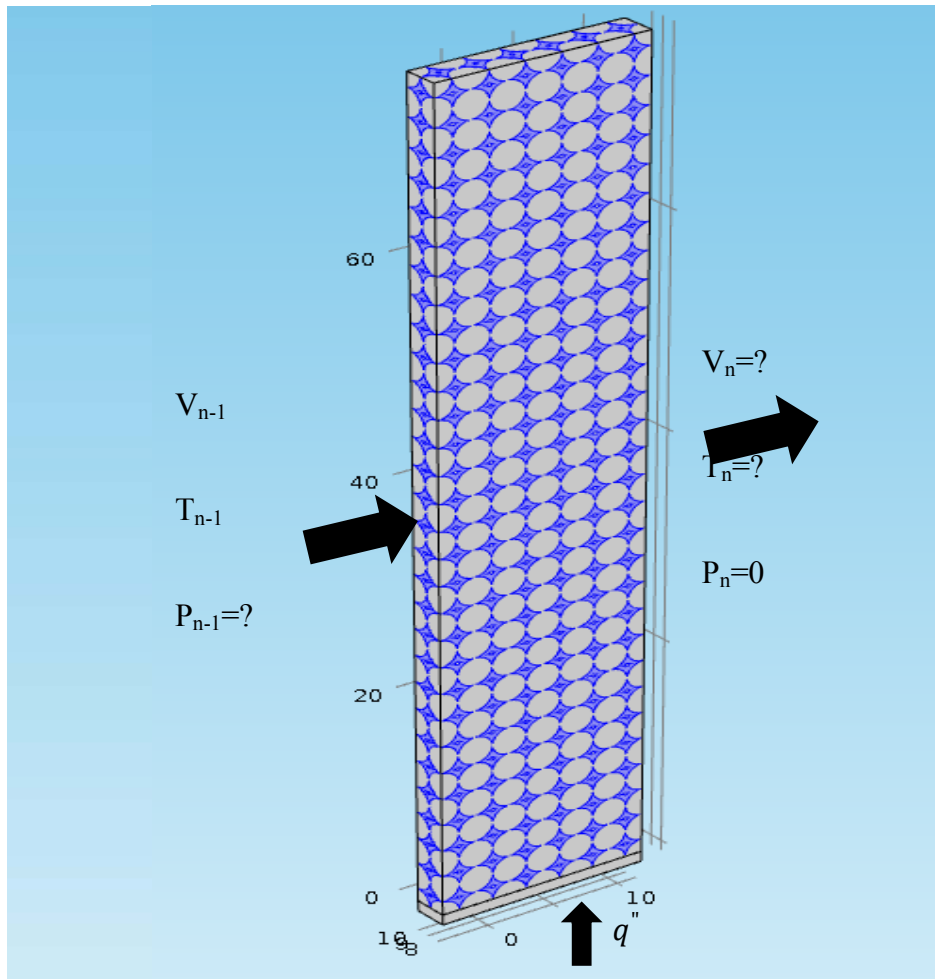


Figure 6.11 The Last Marching Block Set-Up

6.4 Mesh Independence

The computational domain was meshed using tetrahedral elements (3D). A finer mesh was applied to areas on the porous cell surface to account for the large gradients that occur in these areas. Mesh independence was established to ensure that the solution or results is/are independent of the mesh size. To confirm mesh independence, the same computational domain was spatially discretized using three meshes of varying refinement.

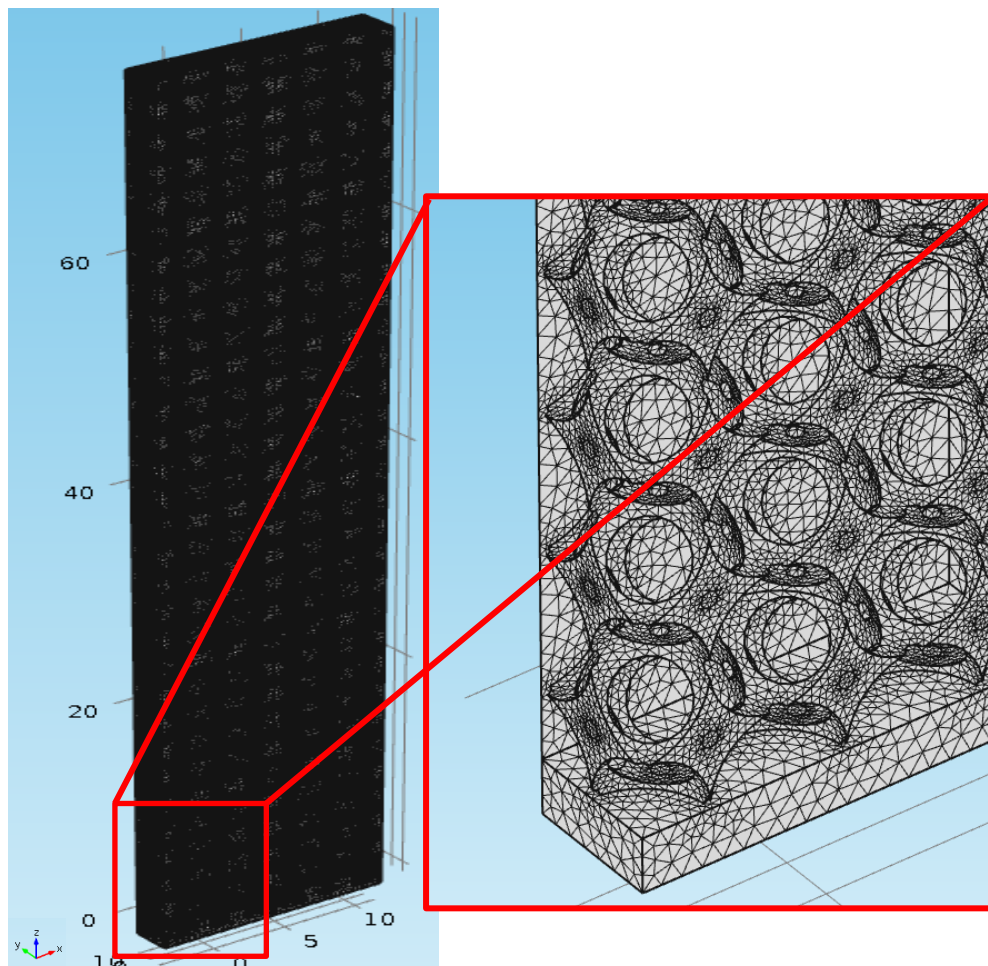


Figure 6.12 The Computational Model with Fine Mesh

The three different unstructured tetrahedral element meshes were generated with commercial software COMSOL. The coarse mesh consisted of 866,485 elements, medium mesh consisted of 3,910,936, and fine mesh consisted of 4,744,774. All meshes were applied to the present computational model in Fig.6.12, in which the inlet velocity is 0.2 m/sec, the PPI is 20, the porosity is 93.6%, and the wall heat flux is 8495 W/ m^2 .

Figure 6.13 displays mesh details near both the heated wall and the porous media for the coarsest and finest cases. The coarsest mesh was refined up to 5.4 times to perform the mesh independence study, as seen in Table 6.1

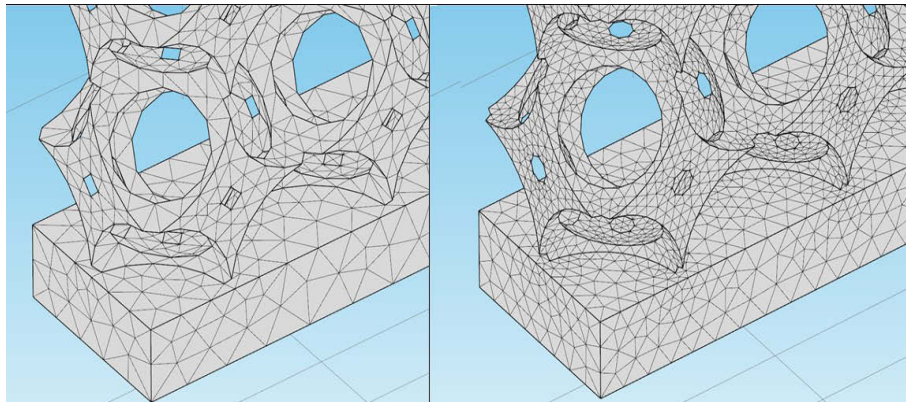


Figure 6.13 Details of Volume Mesh of Heated Wall and Cells for the Coarse and Fine Meshes

Figure 6.14 shows the fluid temperatures obtained from simulation results perpendicular to the flow direction (x direction), and distanced 0.25 inch (0.635 cm). from the inlet for the three different meshes. There is no significant difference among the three meshes: coarse, medium, and fine.

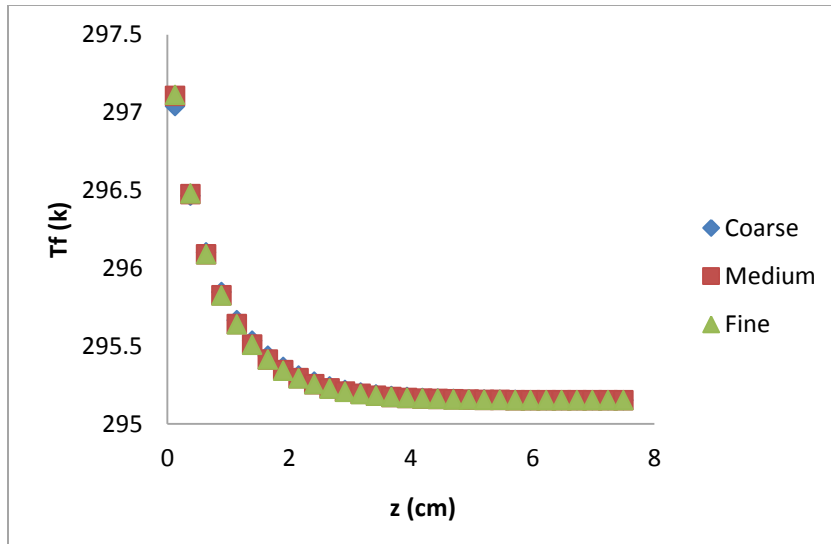


Figure 6.14 Fluid Temperatures at x=0.635 cm for All Meshing

Maximum differences in fluid temperatures (as seen in Figure 6.14) at 0.25 inch (0.635 cm) from the entrance were 0.008 % between the medium and the coarse meshes, and 0.0008% between the medium and the fine meshes.

The pressure drop along flow direction also was calculated to provide more comparisons of the simulation results, as seen in Table 6.1. The relative error of pressure drop between the coarsest and finest mesh is 2.9 %, while the relative error of pressure drop between medium and fine is 0.3 %, as shown in Figure 6.15.

Table 6. 1 Meshing Levels with Their Number of Elements and Pressure Drop (Pa/m)

Mesh	No. Element	Dp/L (Pa/m)
Coarse	866485	57.90
Medium	3910936	56.46
Fine	4744774	56.28

5.4 X

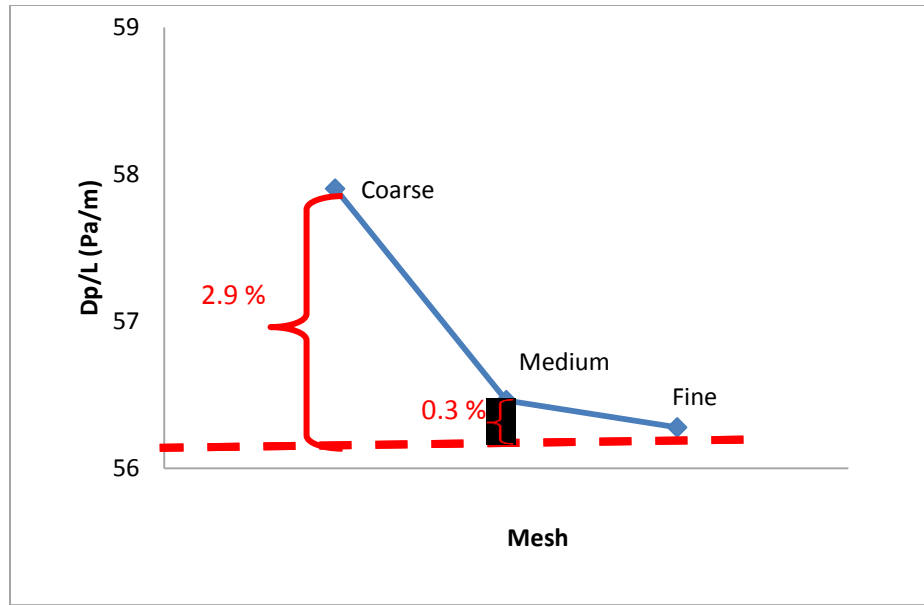


Figure 6.15 Pressure Drop at Different Meshes

Average differences in fluid velocities for the same entrance velocity at 0.25 inch from the inlet were 4.7 % between the medium and the coarse meshes, and 0.17 % between the medium and the fine meshes. Thus, the results of the medium mesh were deemed mesh-independent; and the medium mesh was used for all subsequent studies. Each block was run until convergence, which took one hour and eight minutes. The computer used for simulation ran on a 64-bit operating system, with a processor, Intel (R) Xeon (R), operating at 3.40 GHz and 31.7 GB of usable RAM.

6.5 Results

6.5.1 Temperature Field of Entry Region

Figure 6.16 displays contours of temperature field of air and foam. The temperature field is colored by temperature magnitudes, with red representing high temperatures zones (near the heated wall) and blue representing low temperature zones (near the center).

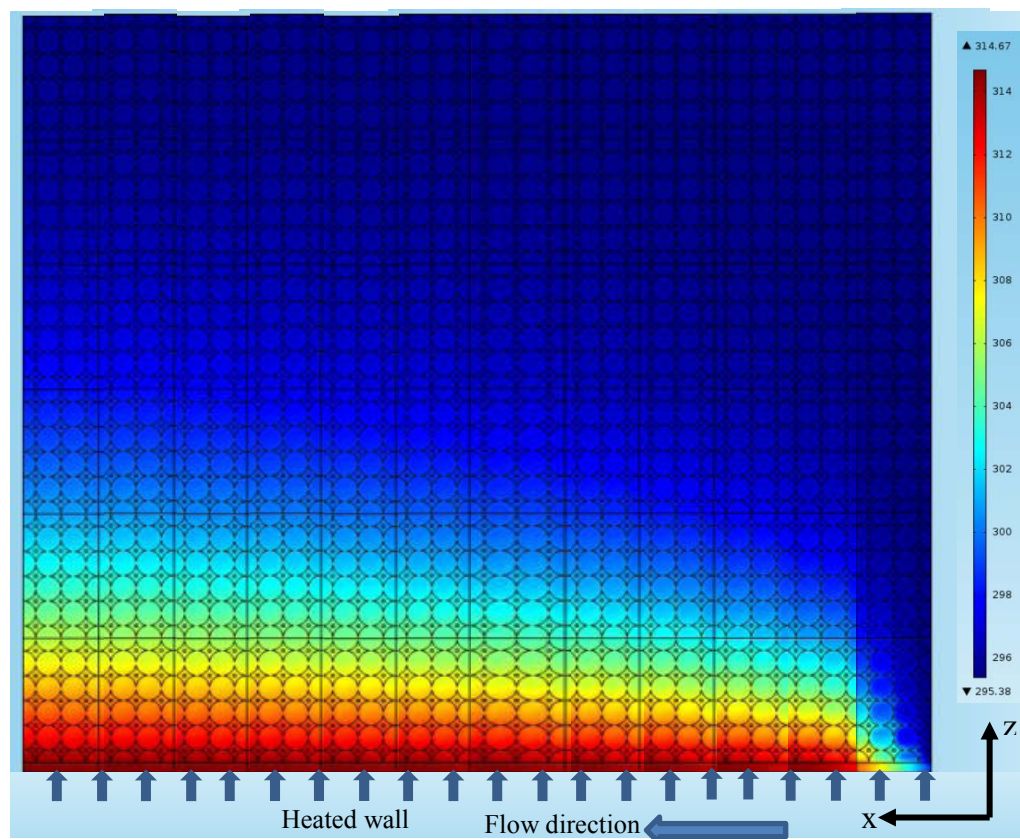


Figure 6. 16 Temperature Field of Developing Entry Rgion

Clearly, the metal foam exhibits thermally developing entry region. The temperature field develops starting at the entrance of the porous channel (the first block), and keeps developing as the distance in the flow direction increases.

Figure 6.17 shows the air temperature measured at 2.55 inch from the heated wall in z- direction at different points in the flow direction- x direction . The temperature increases with increasing the flow direction distance, starting at about 295 k until reaching 296.5 k at 3.55 inches, then, after 3.55 inches from the entrance (twelfth block), the temperature exhibits different slope confirming a change and the heat transfer seems to be evolving towards another region which is a fully – developed region as seen in Figure 6. 18.

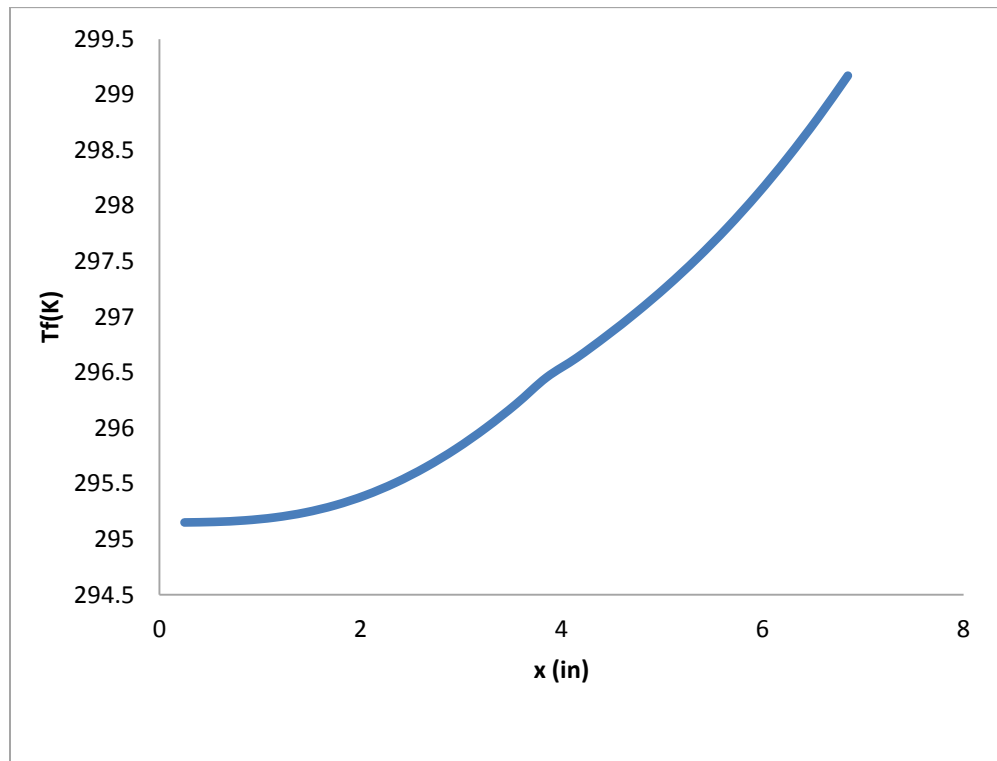


Figure 6. 17 Air Temperature for Fully Developing Region at 2.55 inch from Heated Wall

6.5.2 Temperature Field of Fully Developed Region

In Fig.6.18, the temperature field on the channel walls and the metal foam surface are shown. Obviously, the heat transfer is fully developed. As expected the maximum temperature is reached at the heated wall and decays as the distance from the heated wall increases.

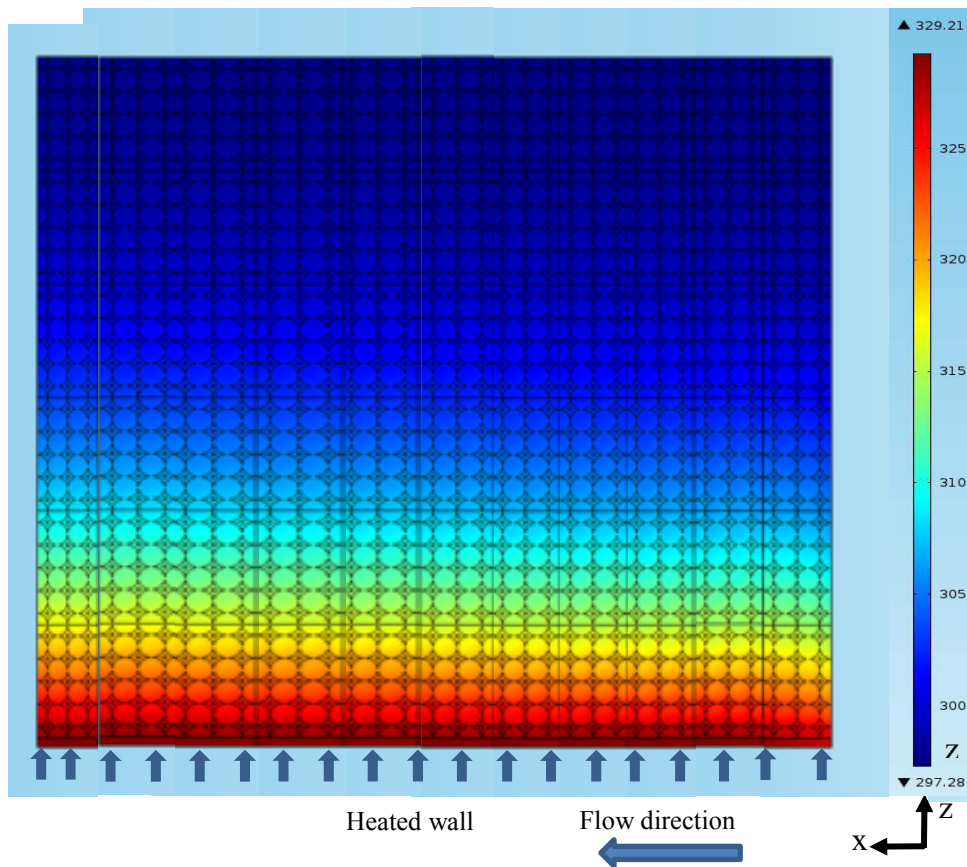


Figure 6. 18 Temperature Field of Fully Developed Region

6.5.3 The Wall Temperature

The wall local temperatures were obtained and are presented in the Fig.6.19 as function of local distance in flow direction. As the distance in the flow direction increases, the wall temperature increases and exhibits different slopes. This behavior

is typical of thermally-developing internal flow, in which the thermal boundary layer starts to grow in the flow direction. After specific distance, this layer stops growing and is in fully –developed region as seen in Figure 6.19. This indicated by the change in slope at about 3.55 (9 cm) inch from the entrance. The nature of the fully developed region slop is constant, but in Fig.6.18 there is small change in slop line due to combination of mapping error as mentioned in section 6.5.2 and rounding of error.

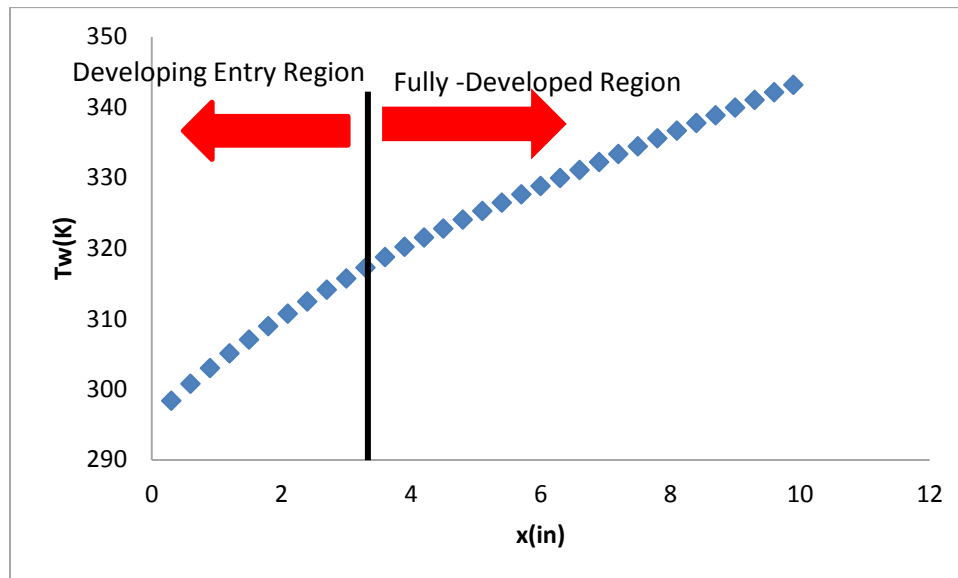


Figure 6.19 Wall Local Temperature as Function of Distance in Flow Direction

6.5.4 Mean Temperature

The mean temperature is given by

$$T_m = \frac{1}{A_f U_m} \left[\int_{A_f} u T_f dA_f \right] + \frac{1}{A_s} \int_{A_s} T_s dA_s \quad (6.12)$$

where A_f and A_s are cross section areas for fluid and solid domains respectively, U_m is mean fluid velocity, u is local fluid velocity, and T_f , T_s are fluid and solid local temperatures respectively. The mean temperature is plotted as function of local distance in the flow direction in Figure 6. 20. The mean temperature keeps increasing as local distance increases. This trend is realistic [44].

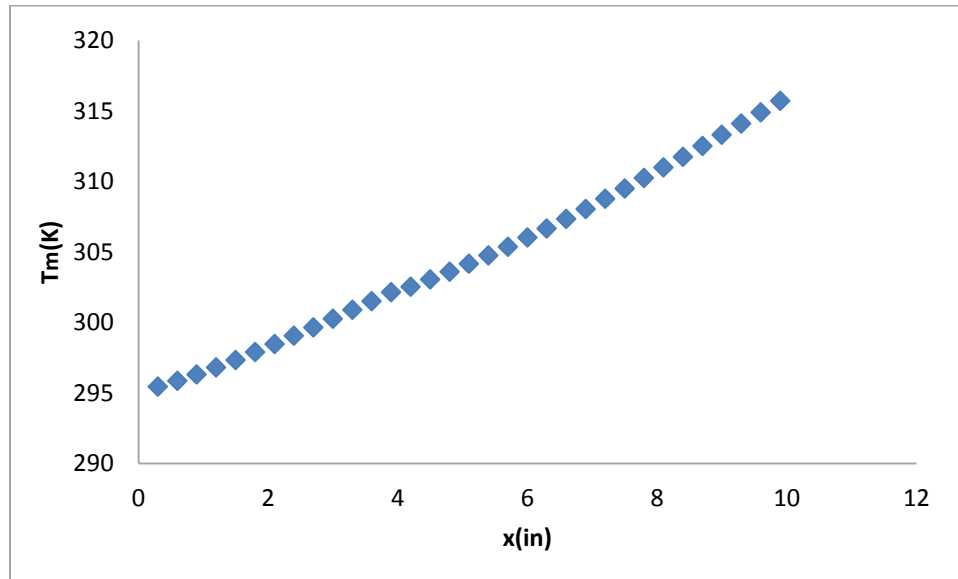


Figure 6. 20 The Mean Temperture as Function of line distance in The Flow direction

6.5.5 Nusselt Number

The local Nusselt number of the surface can be determined from

$$Nu = \frac{hH}{k_f} = \frac{q''H}{k_f(T_w - T_m)} \quad (6.13)$$

where T_w is the local wall temperature . The local Nusselt number is plotted as a function of the local distance in the flow direction in Figure 6. 21. The Nusselt number starts very high at the entrance and starts to decay as the distance from the

entrance increases, and is seen to be asymptotically declining. This behavior is typical of thermally-developing internal flow, in which the thermal boundary layer starts to grow in the flow direction. In this study, many blocks were taken to make the computational domain long enough in the flow direction to encounter the fully-developed region.

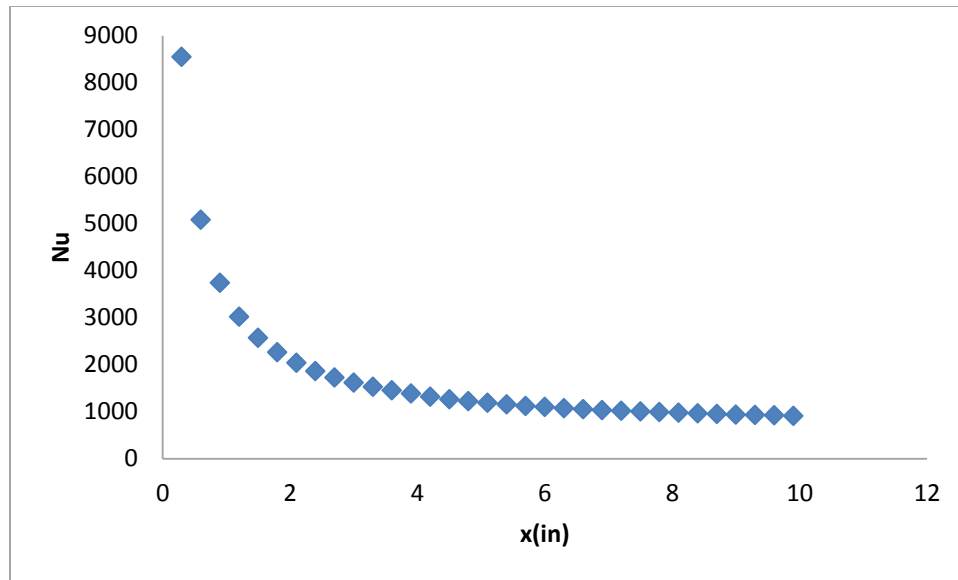


Figure 6. 21 Nusselt Number as a Function of Axial Distance.

Chapter 7 : Heat Transfer Validation

7.1 Volume-Averaged Analytical Solution

Consider a channel filled with open-cell porous medium. The channel has height $2H$ and is bounded by solid surfaces at the top and bottom, as shown in Fig.6.1. The two surfaces are heated with a constant uniform heat flux \dot{q} . Inside the porous medium, there is a one-dimensional fluid flow in the positive x -direction with velocity u .

The Darcy-regime, fully-developed velocity profile is easily obtained [42], and is given by

$$U = 1 - \frac{\cosh\omega Z}{\cosh\omega} \quad (7.1)$$

where $\omega^2 = \mu H^2 / \mu_e K$, $Z = z/H$ and $U = u/u_m$, u_m is the mean velocity (averaged over the cross section). Also, K is the permeability, μ is the fluid viscosity and μ_e the effective viscosity.

For the heat transfer problem, we make the following assumptions:

- Radiation and natural convection are negligible.
- Thermophysical properties of the solid and the fluid phases are constant.
- The porous medium is isotropic and homogeneous.
- Flow and heat transfer are steady and fully-developed.

The two-equation energy model for the solid and the fluid phases is given by

$$k_s \frac{\partial^2 T_s}{\partial z^2} - h\sigma(T_s - T_f) = 0 \quad (7.2)$$

$$k_f \frac{\partial^2 T_f}{\partial z^2} + h\sigma(T_s - T_f) = \rho c u \frac{\partial T_f}{\partial x} \quad (7.3)$$

where k_s and k_f are the effective thermal conductivities of the solid and the fluid, respectively, T_s and T_f are the volume-averaged temperatures of the solid and the fluid, respectively, h is the heat transfer coefficient between the solid and the fluid, σ is the surface area per unit volume of the porous medium, ρ is the density of the cooling fluid, c is the specific heat of the fluid, and u is the volume-averaged velocity inside the pores. Equations (7.2) and (7.3) are well-known and have been used extensively. The following boundary conditions apply:

$$\text{At } z = H \quad \frac{\partial T_s}{\partial z} = \frac{\partial T_f}{\partial z} = 0 \quad (7.4)$$

$$\text{At } z = 0 \quad T_s = T_f = T_w \quad (7.5)$$

where T_w is the wall temperature (unknown).

In a non-dimensional form Eq. (7.1) through Eq. (7.5) become

$$\frac{\partial^2 \theta_s}{\partial Z^2} - B_i(\theta_s - \theta_f) = 0 \quad (7.6)$$

$$\lambda \frac{\partial^2 \theta_f}{\partial Z^2} + B_i(\theta_s - \theta_f) = U \quad (7.7)$$

$$\text{At } Z = 0 \quad \frac{\partial \theta_s}{\partial Z} = \frac{\partial \theta_f}{\partial Z} \quad (7.8)$$

$$\text{At } Z = 1 \quad \theta_s = \theta_f = 0 \quad (7.9)$$

where $X = x/H$, $\lambda = k_f/k_s$, $B_i = h \sigma H^2/k_s$ is the Biot number for the porous medium

$\theta_f = (T_f - T_w)/\dot{q} H/k_s$ and $\theta_s = (T_s - T_w)/\dot{q} H/k_s$. It should be noted that for thermally fully-developed flow, $\partial T_f/\partial x$ is constant and can be evaluated by integrating the sum of the two energy equations over the cross section.

In this study, the parameters that will be used are obtained by direct or measurement or by computation, as follows. The surface area density of the foam is calculated from a correlation given by the manufacturer, ERG Duocel®. The effective thermal conductivity of the solid, k_s , is obtained from a model given in Calmidi and Mahajan[45]. The interstitial heat transfer coefficient inside the foam, h , is computed based on a correlation given by Kuwahara et al.[46]

The solution of Eqs.(7.6) to (7.9) involves the following steps [42] By adding Eqs. (7.6) and (7.7), a single second order, nonhomogeneous, ordinary differential equation for $\lambda\theta_f + \theta_s$ is obtained.

1. The velocity solution from Eq.(7.1) is substituted in the equation obtained in step 1. This equation is solved for $\lambda\theta_f + \theta_s$.
2. The solid temperature θ_s in terms of the fluid temperature θ_f is taken from step 2.

3. The solid temperature θ_s from step 3 is substituted in the fluid's energy equation (Eq. (7.7)) which results in a single differential equation involving the fluids' temperature θ_f only. Therefore the coupled two energy equations are de-coupled.
4. The equation for the fluid's temperature θ_f obtained in step 4 is solved. The solution is given by

$$\theta_f = b_1 \cosh \psi Z + d_1 \cosh \psi Z + d_3 Z^2 + d_5 \quad (7.10)$$

where ω was defined with Eq.(7.1) and $\psi^2 = B_i(\lambda + 1)/\lambda$. The constants in Eq.(7.10) are given as

$$d_1 = \frac{B_i - \omega^2}{\omega^2 \cosh \omega [\lambda \omega^2 - B_i(\lambda + 1)]}$$

$$d_3 = \frac{1}{2(\lambda + 1)}$$

$$d_5 = \frac{B_i \left(\frac{1}{\omega^2} - \frac{1}{2} \right) - 1}{B_i(\lambda + 1)} + \frac{\lambda}{B_i(\lambda + 1)^2}$$

And

$$b_1 = - \frac{d_1 \cosh \omega + d_3 + d_5}{\cosh \psi}$$

7.2 Experiment

7.2.1 Sample

The sample is an aluminum cylindrical tube filled with aluminum foam, which is brazed to its inside wall. The outside diameter of the tube is 10.6 inches, the inside diameter is 10.1 inches and the length is 6 inches (as shown in Figure 7. 1)

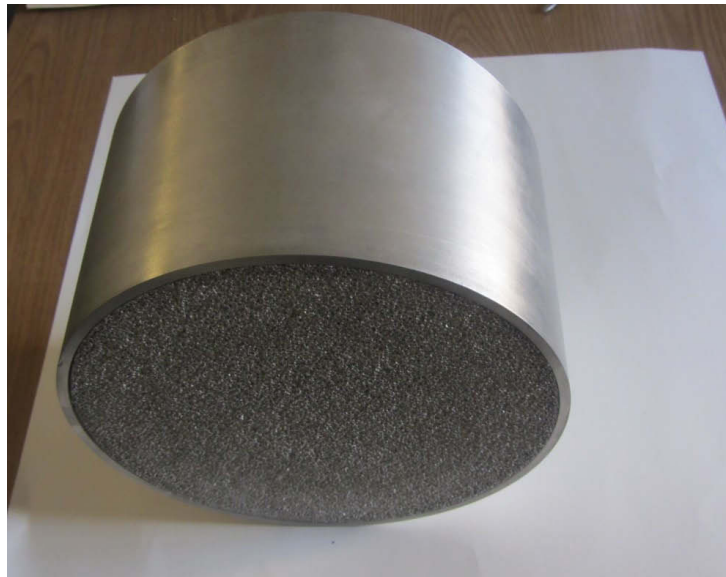


Figure 7. 1 Photograph of the Cylindrical Foam Sample

The sample was made by ERG Materials and Aerospace from aluminum alloy 6101-T6 foam with 20 ppi (20 pores per linear inch). As shown in Figure 7. 2, 50 holes with a diameter of 0.19 inches were drilled in different locations. The purpose of these holes was to measure the temperature of the air radially and along the sample by inserting thermocouples inside each hole. The 50 holes were divided to five sets and each set contains 10 of them.

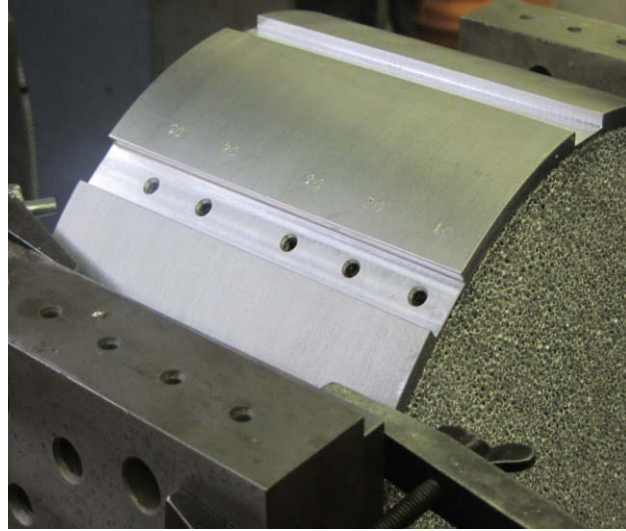


Figure 7. 2 Photograph of the Thermocouples' Holes

To arrange the thermocouples we made a numbering system for them as shown in Table 7. 1. The numbering system consists of two digit number: A (B), where A is distance from entrance in inches and B is depth from outside surface in inches.

Table 7. 1 Location of Each Themocouple and Numbering System

First set of holes	Second set of holes	Third set of holes	Fourth set of holes	Fifth set of holes
0.5(0.8)	1.5(0.8)	2.5(0.8)	4(0.8)	5(0.8)
0.5(1.3)	1.5(1.3)	2.5(1.3)	4(1.3)	5(1.3)
0.5(1.8)	1.5(1.8)	2.5(1.8)	4(1.8)	5(1.8)
0.5(2.3)	1.5(2.3)	2.5(2.3)	4(2.3)	5(2.3)
0.5(2.8)	1.5(2.8)	2.5(2.8)	4(2.8)	5(2.8)
0.5(3.3)	1.5(3.3)	2.5(3.3)	4(3.3)	5(3.3)
0.5(3.8)	1.5(3.8)	2.5(3.8)	4(3.8)	5(3.8)
0.5(4.3)	1.5(4.3)	2.5(4.3)	4(4.3)	5(4.3)
0.5(4.8)	1.5(4.8)	2.5(4.8)	4(4.8)	5(4.8)
0.5(5.3)	1.5(5.3)	2.5(5.3)	4(5.3)	5(5.3)

As shown in Fig.7.3 , five slots(one for each set) were drilled in the wall of the tube to measure the temperature of the wall along the tube by inserting a thermocouple through each slot.

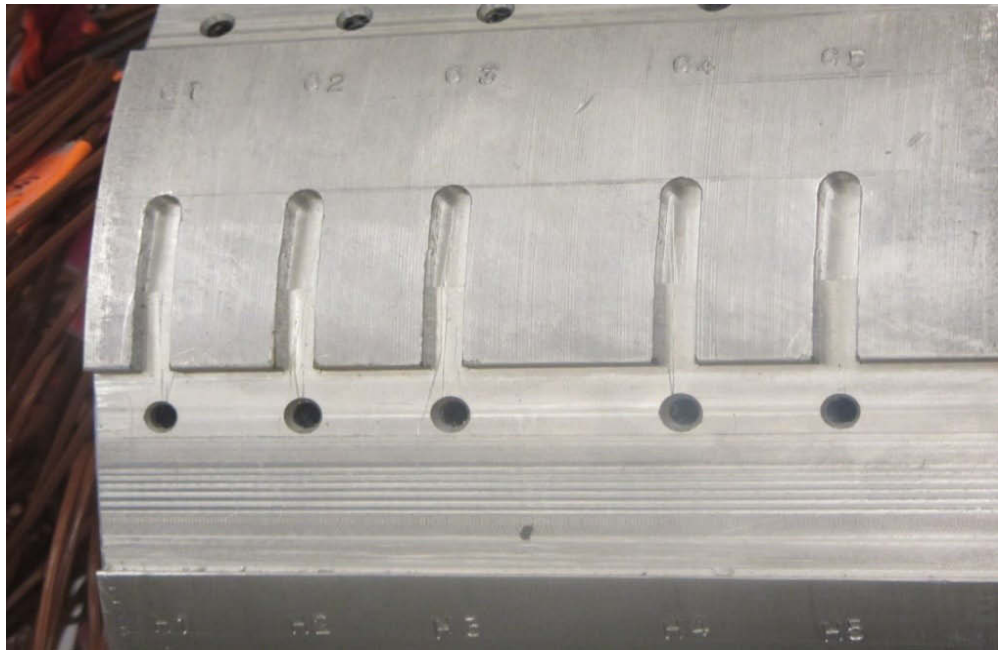


Figure 7. 3 Photograph of Slots to Measure the Temperature of the Wall

As shown in the Fig.7.4 , the angle between each hole in the set was 36° .

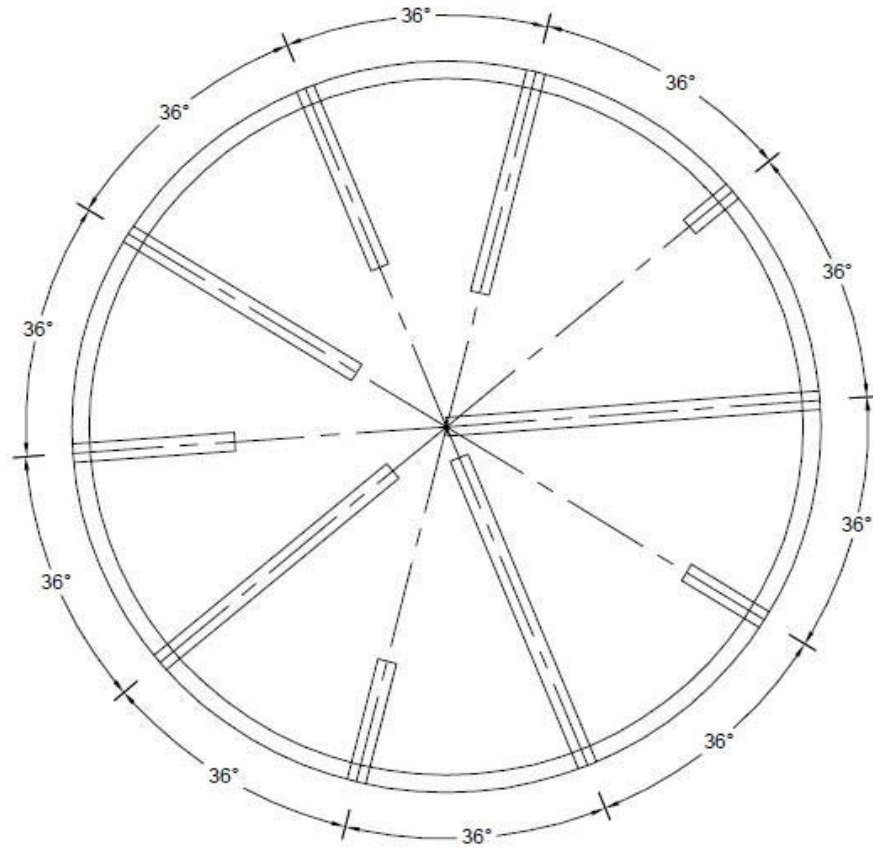


Figure 7. 4 The Angles between the Holes in the Set

For each hole there is a small tube, and the length of the tube depends on the depth of the hole. Small holes were made along each small tube so, as much as possible, not to block air flow, as shown in Figure 7. 5.

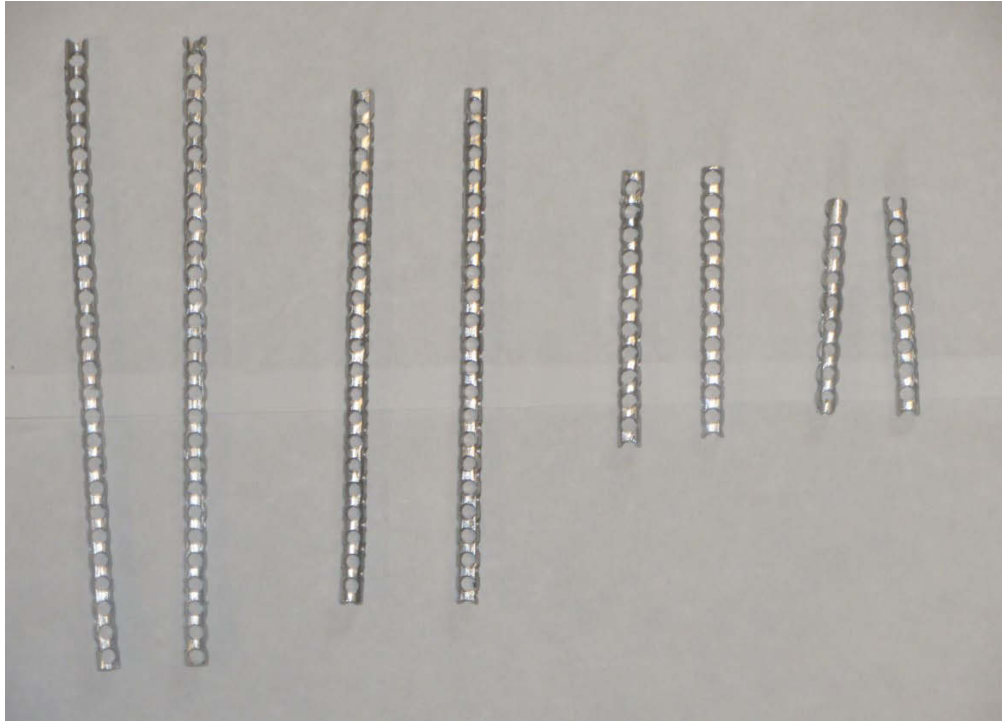


Figure 7. 5 Photograph of the Small Tubes

In every hole there is a thermocouple to measure the temperature of the air. To guarantee the thermocouple measures the temperature of air and not the temperature of the foam, we inserted the thermocouple inside the small tube without the end of the thermocouple touching the tube wall or the foam, as shown in figure7.6.

The purpose of the grooves that appear in figure7.7 is to keep the thermocouples wrapped around the outside cylinder and be flush with its surface.



Figure 7. 6 Photograph of the Thermocouple Inside the Small

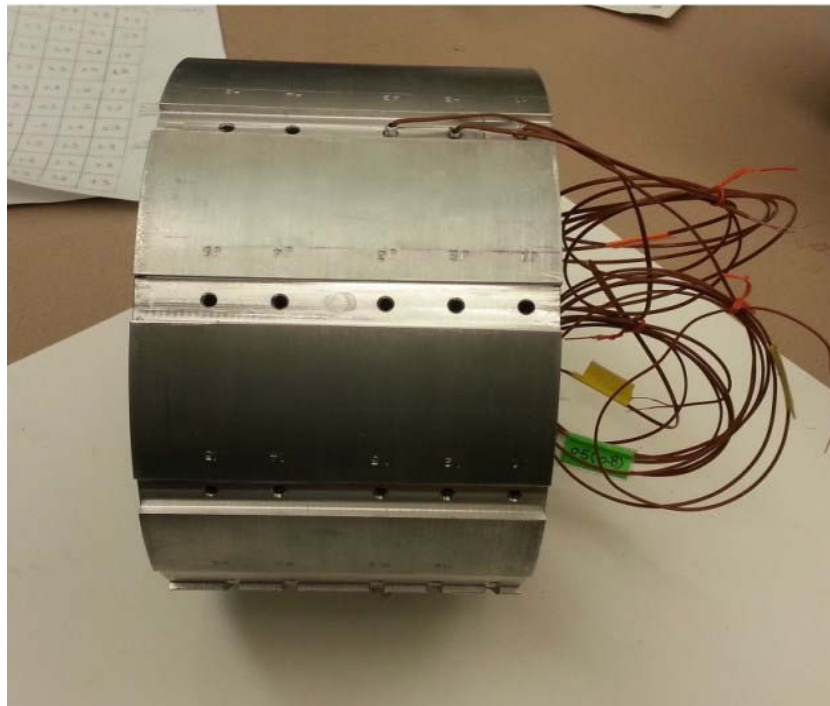


Figure 7. 7 Photograoh of the Groove in the Wall's Sample

Industrial strength epoxy putty was used to fasten the thermocouple inside the tube because this product can resist high temperatures. Figure 7. 8 shows a photograph of the foam sample instrumented with thermocouples. The purpose of the small holes that are shown in the Fig. above was to measure the pressure drop by inserting two small plastic tubes.



Figure 7. 8 Photograph of the Foam Sample Instrumented with Thermocouples

Six thermofoil heaters as shown in Figure 7. 9 were attached to the wall of the tube firmly, without any air gaps, as shown in Figure 7. 10. The dimensions for each heater are 3 inches by 11 inches and they were connected in parallel. The themofoil heaters were made by Minco and the proprties for each one are shown in the Table 7. 2.



Figure 7.9 Photograph of the Heaters

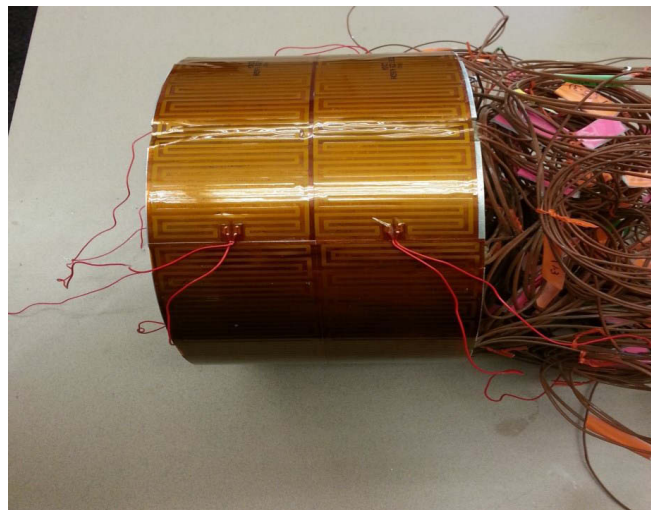


Figure 7.10 Photograph of the Foam Sample with Thermofoil Heaters

Table 7.2 Properties of the Heater

Resistance (Ohms)	Max.Power (Watts)	Heat Flux (Watts/in²)	Max Temp.(°C)
22.3	645.74	21.72	150

7.2.2 Wind Tunnel and Set-up

Experiments were performed in an open-loop tunnel producing air flow rates up to $17 \text{ m}^3/\text{min}$ to induct room air into the tunnel and through the foam sample. The suction unit was powered by eight fans; they were electrically modified so that two could run at a time. The tunnel was fabricated from thin Plexiglass tube as shown in the Figure 7. 11.



Figure 7. 11 Photograph of the Open-Loop Tunnel

We attached the test sample to the face of the nozzle that shows on Fig.7.11, where the diameter of the face of the nozzle is equal to the diameter of the sample. To avoid any convection from the heater, insulation was wrapped around the sample firmly, as shown in Figure 7. 12 and Figure 7. 13.



Figure 7. 12 Photograph of Sample Wrapped with the Insulation

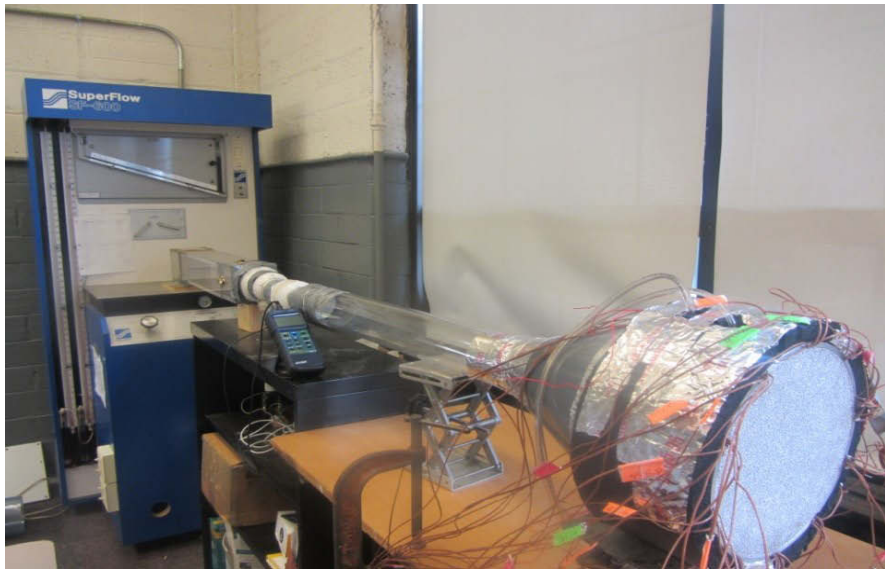


Figure 7. 13 Photograph of the Complete Set-up

7.2.3 Procedure

Electrical power to the heater was measured using a wattmeter, and heat flux was calculated by dividing the power by the surface area of the heater. A DC power supply provided the electrical power. Pressure drop was measured using an Omega differential pressure transmitter with a range of 0 to 746 Pa (0 to 3 in H₂O) .

For velocity measurement, an Extech gas flow meter that could measure speeds up to 35 m/s (29 ft/min) was used. The pressure transducer, the flow meter, and thermocouples were connected to a data acquisition system (DAQ, by Omega Engineering) which delivered the readings to a computer. The flow rate was varied to realize different velocities in the test section. For each velocity, the steady-state static pressure drop was measured using pressure taps and the differential pressure transducer, and thermocouples measured the temperatures. The measurements were repeated three times, and the average for the three runs was reported.

7.3 Comparison

Figure 7. 14 shows non- dimensional air temperatures of numerical and experimental solutions along flow direction. In general, the two air temperatures decay as the distance from heated wall ($Z=1$) increases, as expected. Both air temperatures were measured within fully–developed region. However, the entry length was different in experiment than in the numerical simulation. In particular, the thermal fully developed region started at 2.5 inches (6.35 cm) from the entrance in the experiment. In the numerical model, the flow took longer to be in the fully – developed region which started at 3.55 inches (9 cm), as seen in fig. 6.18. To be safe, air temperatures were numerically measured and plotted at 11.95 inches after which no change occurred. This difference in the entry length was due to numerical error and mapping error between the blocks in the marching technique. Relative Averaging error between the experimental and numerical air temperature is about 14 %. Maximum and minimum are 31 % and 5 % receptively

The two points closest to the center of the foam cylinder of experimental model are seen to produce lower non-dimensional fluid temperatures, or higher physical temperatures, noting that $\theta_f = (T_f - T_w)/q''H/k_s$. Inspection of fig.7.4, which shows the arrangement of the thermocouples around the cross section, indicates that these two points are marked by the numbers 13.46 and 12.19 cm. The figure clearly shows that the blockage caused by inserting the two small perforated tubes with their thermocouples is significant enough to cause the temperatures at these two locations to be higher that what they would have been if the structure of the foam was not disturbed.

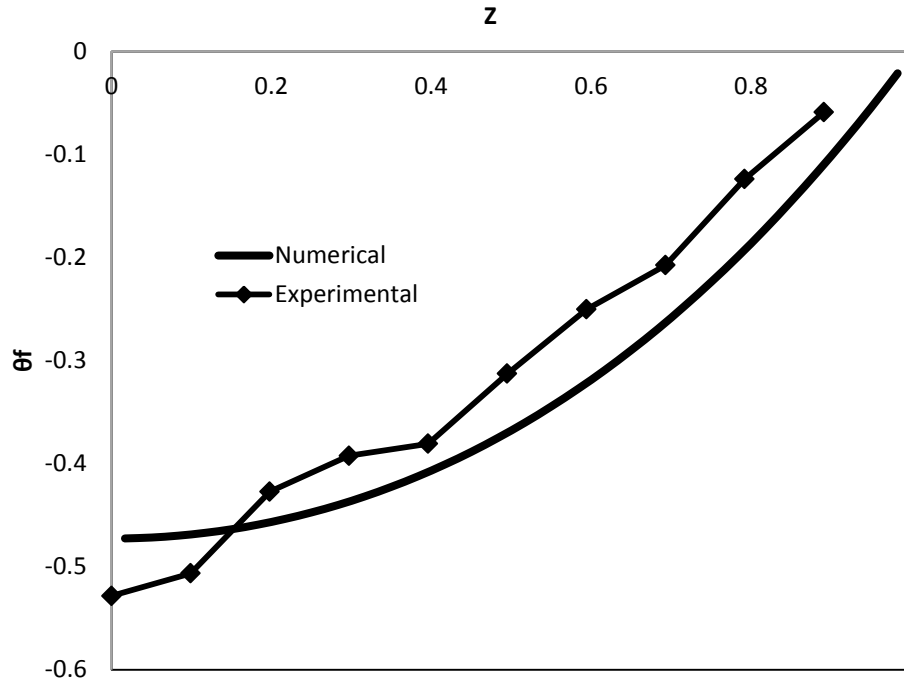


Figure 7. 14 Experimental and Numerical Air Temperatures

Figure 7. 15 shows comparison of the non- dimensional air temperatures between the numerical and the analytical solution as a function of non-dimensional distance in z direction (perpendicular to flow direction) at 11.95 inches from entrance (fully-developed region). The two temperature curves are relatively close to each other, with the analytical solution predicting a slightly lower temperature close to the center. It should be noted that the analytical solution of the volume –averaged energy equation calculated air temperature average over an averaging volume, while in numerical solution, the point local air temperature are calculated.

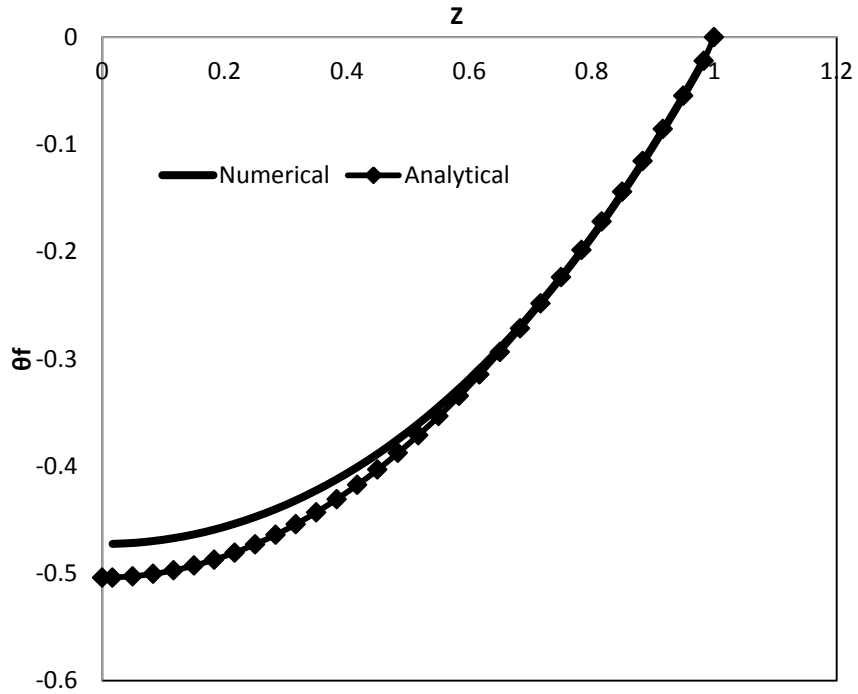


Figure 7. 15 Analytical and Numerical Air Temperatures

From particular standpoint, the comparison should be done between the numerical and the experimental results for the same cross section. The available experimental model is a cylinder filled with foam, while the numerical simulation is for infinite parallel plates. However, we can be overcome this issue by comparing: (a) difference between analytical solutions for flat plates of height $2H$ (see equation 7.10) and a cylinder of radius r_0 [47]; (b) difference between physical air temperatures from the numerical solution for the flat plates to the physical air temperatures of the experiment for the cylinder.

Figure 7.16 shows the volume-averaged analytical air temperature difference between the theoretical solutions for the flat plates and the cylinder as function of distance from the heated wall.

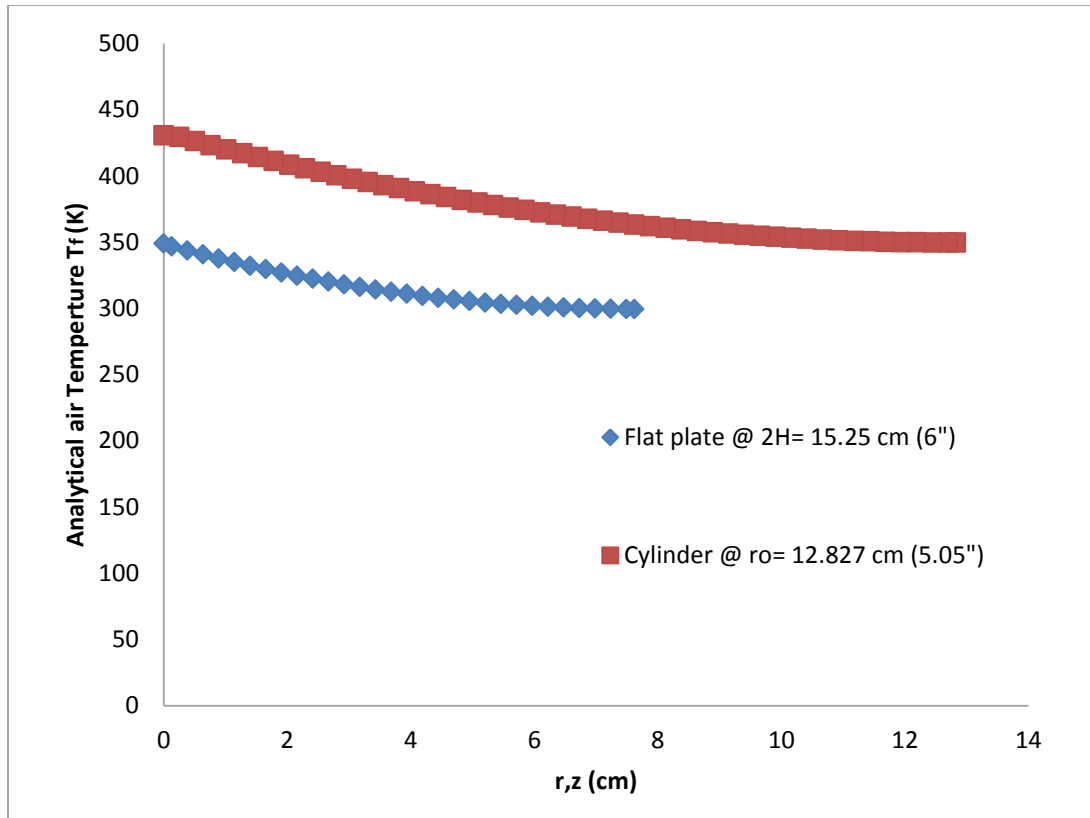


Figure 7. 16 Analytical Air Temperature

These two analytical cases correspond to our simulation and our experiment. The two cases are subject to the same heat flux (8495 W/m^2) and velocity (0.2 m/s), also the foam is the same. It can be noted that the two air temperatures have similar behavior, and the difference between them is almost constant.

Figure 7.17 shows comparison of physical air temperatures from the numerical simulation to the physical air temperatures of the experiment as function of a distance from the heated wall.

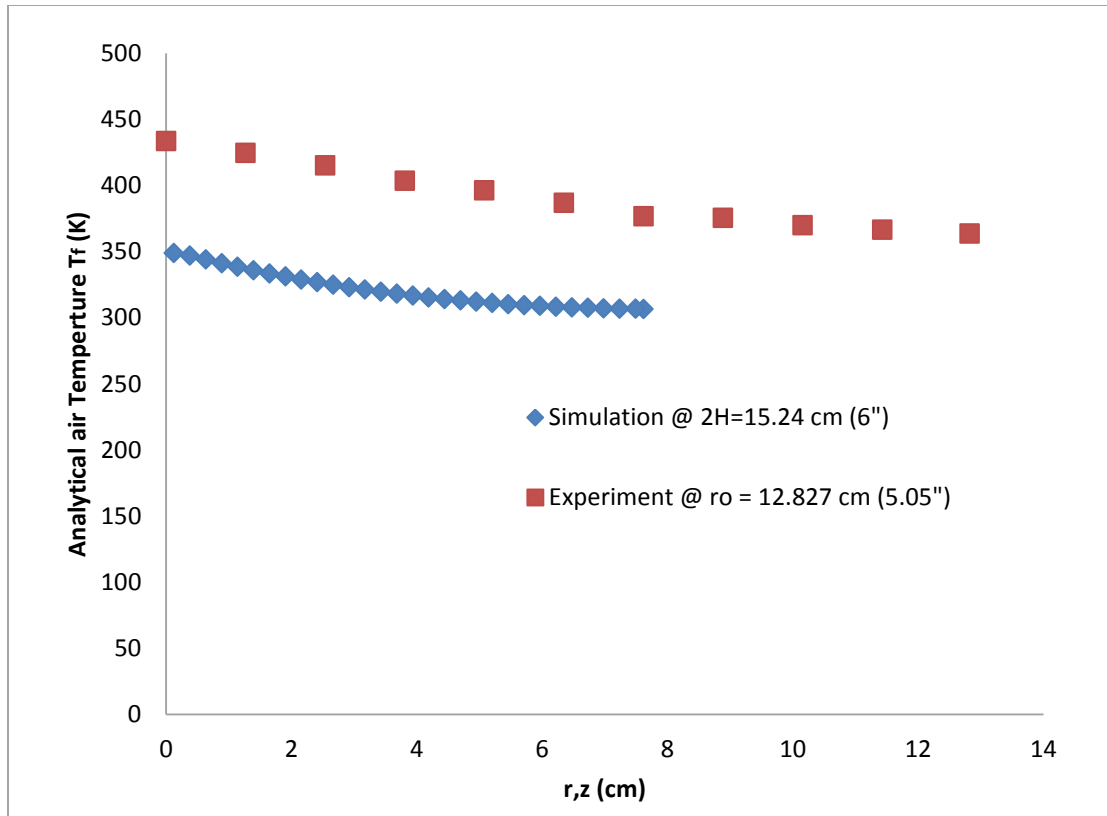


Figure 7. 17 Physical Air Temperatures

These two physical curves are a little different from analytical curves as shown in Fig.7.16, but they have the same trend. The difference between physical air temperatures is almost constant.

Table 7.2 shows the average, maximum and minimum differences in air temperatures between two cases (the analytical-solution case and the simulation-experiment case). The locations of maximum and minimum difference are also included. In last column, relative error between average, maximum and minimum differences obtained analytically to differences obtained in by comparing the simulation to the experiment are also tabulated. Good agreement is obtained.

Table 7. 3 Air temperature Differences for Parallel plates and cylinder

Air temperature difference	Analytical	Simulation- experiment	Error (%)
Average (K)	75.88	83.75	10.4
Max. (K)	82.52	90.38	9.5
Loction (cm)	0.508	2.54	
Min. (K)	62.52	70.14	12.2
Loction (cm)	7.62	7.62	

Chapter 8 : Conclusion

Open-cell metal foam was successfully simulated. In particular, a unit geometrical cell representing the internal structure of the foam was described in detail. The unit was imported into a finite-element packaged, and the flow and convective heat transfer of air was analyzed numerically by solving the pertinent governing equations in the fluid domain. The detailed flow field and temperature profiles obtained from the numerical solution were seen to make qualitative physical sense.

From the detailed flow field solution, the pressure drop across the foam could be ascertained. To validate the model, a physical experiment was conducted on 10-pores-per-inch commercial aluminum foam. The Darcy-regime pressure drop for various flow velocities matched the values obtained by the simulation. The agreement was deemed reasonably good, with a maximum difference of about 15% between the simulation and the experimental values of the pressure drop in the low-velocity regime.

For the numerical heat transfer model, the porous foam domain had 20 pores-per-inch and 94 % porosity. Experimental validations of the numerical model was conducted. In particular, direct measurement of the fluid temperature inside a heated cylinder filled with metal foam was conducted using a specially-designed technique. The data points were obtained in the Darcy regime and in the thermally fully-developed region. . In order to compare numerical results to analytical predictions, the thermal-non-equilibrium two-equation model for convection heat transfer in a heated duct filled with a porous medium was revisited. The analytical fluid temperature was presented. The solution employed the Brinkman-extended Darcy

flow momentum equation. Relatively good agreement between the numerical and analytical fluid temperatures and between numerical and experimental fluid temperatures was displayed. The numerical technique can be of utility for heat transfer designs, and for validating cases of the transport phenomenon in open-cell metal foam. In additions , the numerical model can be used an optimization approach for minimizing pressure drop and maximizing heat transfer. A future study is on the effect of dividing the domain into sectors, and manipulating the sectors' configurations on the flow and heat transfer. Other future work should form a better marching of the surface area density of the geometrical model and that of actual foam

References

- [1] Sullines D., and Daryabeige K., 2001, "Effective Thermal Conductivity of High Porosity Open Cell Nickel Foam : Sullins, Alan D. : Free Download & Streaming : Internet Archive," 35th AIAA Thermophysics Conference, Anaheim,CA.
- [2] Bastwros A. F., 1998, "Effectiveness of Open Cell Metallic Foams for High Power Electronic Cooling," the Symposium on the Thermal Management of Electronics,IMECE, Anaheim, CA.
- [3] Vafai K., and Tien C. L., 1982, "Boundary and inertia effects on convective mass transfer in porous media," *International Journal of Heat and Mass Transfer*, **25**(8), pp. 1183–1190.
- [4] AshbyMichael, Evans T., Fleck N. . A., Hutchinson J. W. W., Wadley H. N. G. N. G., and Gibson L. J., 2000, *Metal Foams: A Design Guide*, Woburn,MA.
- [5] Hwang J.-J., Hwang G.-J., Yeh R.-H., and Chao C.-H., 2002, "Measurement of Interstitial Convective Heat Transfer and Frictional Drag for Flow Across Metal Foams," *Journal of Heat Transfer*, **124**(1), p. 120.
- [6] Boomsma K., Poulikakos D., and Zwick F., 2003, "Metal foams as compact high performance heat exchangers," *Mechanics of Materials*, **35**(12), pp. 1161–1176.
- [7] Lage J., 1998, "The fundamental theory of flow through permeable media from Darcy to turbulence," *Transport phenomena in porous media*, pp. 1–30.
- [8] Antohe B., Lage J., Price D., and Weber R., 1997, "Experimental determination of permeability and inertia coefficients of mechanically compressed aluminum porous matrices," *Journal of fluids engineering*, **119**(2), pp. 404–412.
- [9] Seguin D., Montillet A., Comiti J., and Huet F., 1998, "Experimental characterization of flow regimes in various porous media—II: Transition to turbulent regime," *Chemical Engineering Science*, **53**(22), pp. 3897–3909.
- [10] Paek J. W., Kang B. H., Kim S. Y., and Hyun J. M., 2000, "Effective Thermal Conductivity and Permeability of Aluminum Foam Materials¹," *International Journal of Thermophysics*, **21**(2), pp. 453–464.
- [11] Noh J.-S., Lee K. B., and Lee C. G., 2006, "Pressure loss and forced convective heat transfer in an annulus filled with aluminum foam," *International Communications in Heat and Mass Transfer*, **33**(4), pp. 434–444.

- [12] Haji-Sheikh A., and Vafai K., 2004, "Analysis of flow and heat transfer in porous media imbedded inside various-shaped ducts," *International Journal of Heat and Mass Transfer*, **47**(8-9), pp. 1889–1905.
- [13] Vafai K., and Kim S. J., 1989, "Forced convection in a channeld filled with a porous medium: An Exact solution," *Journal of Heat Transfer*, **111**(November), pp. 1103–1106.
- [14] Beckerman C., and Viskanta R., 1987, "Forced convection Boundary layer flow and heat transfer along a flat plate embedded in a porous medium," *International Journal of Heat and Mass Transfer*, **30**(7), pp. 1547–1987.
- [15] Nield D. A., Kuznetsov A. V., and Xiong M., 2004, "Thermally developing forced convection in a porous medium: parallel plate channel or circular tube with isothermal walls," *Journal of Porous Media*, **7**(1), pp. 19–27.
- [16] Nield D. A., Kuznetsov A. V., and Xiong M., 2003, "Thermally developing forced convection in a porous medium: parallel plate channel or circular tube with walls at constant heat flux," *Journal of Porous Media*, **6**(3), pp. 203–212.
- [17] Kim S. J., and Jang S. P., 2002, "Effects of the Darcy number, the Prandtl number, and the Reynolds number on local thermal non-equilibrium," *International Journal of Heat and Mass Transfer*, **45**(19), pp. 3885–3896.
- [18] Nield D. A., and Bejan A., 1999, *Convection in Porous Media*, Springer-Verlag, New York.
- [19] Boomsma K., and Poulikakos D., "The effects of compression and pore size variations on the liquid flow characteristics in metal foams," *Journal of fluids engineering*, **124**(1), pp. 263–272.
- [20] Bhattacharya A., and Mahajan R. L., 2002, "Numerical modeling of pressure drop across high porosity metal foams," (June), p. 85226.
- [21] Kumar S., and Murthy J. Y., "A numerical technique for computing effective thermal conductivity of fluid-particle mixtures," *Numerical heat transfer. Part B, fundamentals*, **47**(6), pp. 555–572.
- [22] Kopanidis A., Theodorakakos A., Gavaises E., and Bouris D., 2010, "3D numerical simulation of flow and conjugate heat transfer through a pore scale model of high porosity open cell metal foam," *International Journal of Heat and Mass Transfer*, **53**(11-12), pp. 2539–2550.
- [23] Boomsma K., and Poulikakos D., 2001, "On the effective thermal conductivity of a three-dimensionally structured fluid-saturated metal foam," *International Journal of Heat and Mass Transfer*, **44**(4), pp. 827–836.

- [24] Kaviany M., 1999, Principles of heat transfer in porous media, Springer, New York.
- [25] Vafai K., and Tien C. L., 1981, "Boundary and inertia effects on flow and heat transfer in porous media," *International Journal of Heat and Mass Transfer*, **24**(2), pp. 195–203.
- [26] Poulidakos D., and Renken K., 1987, "Forced-convection in a channel filled with porous-media, including the effects of flow inertia, variable porosity, and Brinkman friction," *ASME Journal of Heat Transfer*, **109**, pp. 880–888.
- [27] Boomsma K., Poulidakos D., and Ventikos Y., 2003, "Simulations of flow through open cell metal foams using an idealized periodic cell structure," *International Journal of Heat and Fluid Flow*, **24**(6), pp. 825–834.
- [28] Hu Y.-J., Zhu Y.-Y., and Cheng C.-J., 2009, "DQM for dynamic response of fluid-saturated visco-elastic porous media," *International Journal of Solids and Structures*, **46**(7-8), pp. 1667–1675.
- [29] Krishnan S., Murthy J. Y., and Garimella S. V, 2006, "Direct Simulation of Transport in Open-Cell Metal Foam," *Journal of Heat Transfer*, **128**(8), p. 793.
- [30] Du Plessis P., Montillet A., Comiti J., and Legrand J., 1994, "Pressure drop prediction for flow through high porosity metallic foams," *Chemical Engineering Science*, **49**(21), pp. 3545–3553.
- [31] Karimian S. a. M., and Straatman A. G., 2008, "CFD study of the hydraulic and thermal behavior of spherical-void-phase porous materials," *International Journal of Heat and Fluid Flow*, **29**(1), pp. 292–305.
- [32] Bai M., and Chung J. N. N., 2011, "Analytical and numerical prediction of heat transfer and pressure drop in open-cell metal foams," *International Journal of Thermal Sciences*, **50**(6), pp. 869–880.
- [33] Horneber T., Rauh C., and Delgado A., 2012, "Fluid dynamic characterisation of porous solids in catalytic fixed-bed reactors," *Microporous and Mesoporous Materials*, **154**, pp. 170–174.
- [34] Anghelescu M. S., 2009, "Thermal and Mechanical Analysis of Carbon Foam," Ohio University.
- [35] De Jaeger P., De Schamphelreire S., T'Joel C., Huisseune H., Ameel B., and De Paepe M., 2012, "Closure term modeling of the volume averaged transport equations for open," 9th International conference on Heat Transfer , Fluid Mechanics and Thermodynamics, Hefat , Malta.

- [36] Voronov R., Vangordon S., Sikavitsas V. I., and Papavassiliou D. V, 2010, “Computational modeling of flow-induced shear stresses within 3D salt-leached porous scaffolds imaged via micro-CT.,” *Journal of biomechanics*, **43**(7), pp. 1279–1286.
- [37] Bai M., and Chung J. N., 2011, “Analytical and numerical prediction of heat transfer and pressure drop in open-cell metal foams,” *International Journal of Thermal Sciences*, **50**(6), pp. 869–880.
- [38] “ERG Duocel® – Reticulated Carbon, Ceramic, & Metal Foam” [Online]. Available: <http://www.ergaerospace.com/index.html>. [Accessed: 23-Jan-2013].
- [39] Dukhan N., and Mohamed Ali., 2012, “On the Various Flow Regimes in Open-Cell Metal Foam,” *International Journal of Transport Phenomena.*, **3.2**, pp. 85–97.
- [40] Dukhan N., and Bodke S., 2012, “Metal Foam-PCM: Heat Storage Technology: The Thermal Charging Scenario,” *Electronics Cooling*, pp. 8–11.
- [41] Dukhan N., and Chen C., “CH-12-C038-Metal-Foam Enhanced PCM Storage System: The Cylinder-in-Cylinder Geometry,” *Proceedings, ASHRAE Winter Meeting, Chicago,IL*, p. 293.
- [42] Dukhan N., 2013, *Metal Foams: Fundamentals and Applications*, DEStech Publications, Inc, Lancaster, PA.
- [43] Dukhan N., 2012, “Analysis of Brinkman-Extended Darcy Flow in Porous Media and Experimental Verification Using Metal Foam,” *Journal of fluids engineering*, **134**(7), p. DOI: 10.1115 / 1.4005678.
- [44] Incropera F. P., DeWitt D. P., Bergman T. L., and Lavine A. S., 2007, *Fundamentals of Heat and Mass Transfer*, John Wiley & Sons.
- [45] Calmidi V. V, and Mahajan R. L., 1999, “The Effective Thermal Conductivity of High Porosity Fibrous Metal Foams,” *Journal of Heat Transfer*, **121**(2), pp. 466–471.
- [46] Kuwahara F., Shiota M., and Nakayama A., 2001, “A numerical study of interfacial convective heat transfer coefficient in two-energy equation model for convection in porous media,” **44**, pp. 1153–1159.
- [47] Nihad D., Rammahi M. A. Al, and Ahmed S. Suleiman, 2013, “Fluid Temperature Measurements inside Metal Foam and Comparison to Brinkman-Darcy Flow Convection Analysis,” *International Journal of Heat and Mass Transfer*, (in press).